FAULTING AND DEFORMATION AT DIVERGENT AND TRANSFORM PLATE BOUNDARIES

by

Samuel M. Howell

submitted in partial fulfillment of the requirements for the degree of

DOCTOR OF PHILOSOPHY
in
GEOLOGY AND GEOPHYSICS
at the
UNIVERSITY OF HAWAIʻI AT MĀNOA

December 2016

Dissertation Committee

Garrett Apuzen-Ito, Chairperson
Bridget Smith-Konter
Fernando Martinez
James Foster
Daisuke Takagi

ACKNOWLEDGEMENTS

I thank Garrett Ito, Bridget Smith-Konter, Fernando Martinez, Neil Frazer, Mark Behn, Jean-Arthur Olive, Javier Escartın, Boris Kaus, Eric Mittelstaedt, Xiaopeng Tong, David Sandwell, Thomas Morrow, and Anton Popov for their invaluable contributions to the research presented here. Further, I thank the Department of Geology and Geophysics and the School of Ocean and Earth Science and Technology for their educational and financial support.

Chapter 2 was supported by National Science Foundation (NSF) grants EAR-0838252 and EAR-1424374. Material support for Chapter 2 was based on data provided by the Plate Boundary Observatory operated by UNAVCO for EarthScope and supported by the NSF grants EAR-0350028 and EAR-0732947. Chapters 3 and 4 were supported by NSF grants OCE-11-55098 and OCE-11-54238.

ABSTRACT

Transform tectonic plate boundaries reflect strike-slip interaction between plates of rigid lithosphere that generate many of the planet's most harmful earthquakes. The first study presented focuses on vertical uplift surrounding the San Andreas Fault System. The horizontal interseismic motions of the fault system are largely predictable, but vertical motions arising from tectonic sources remain enigmatic. Careful statistical analysis isolates these tectonic signals from hydrologic and environmental noise, revealing the tectonic fingerprint of far-field flexure due to 300+ years of fault locking and creeping depth variability. At divergent boundaries, mid-ocean ridges accommodate the separation of plates and are responsible for most of Earth's volcanism, linking fundamental magmatic depth to faulting and topography observed on the seafloor. The second study presented focuses on the intermediate spreading rate Chile Ridge. Specifically, we investigate abyssal hill creation and evolution and how variations in magmatic extension influence morphology and faulting along the spreading axis. Our findings indicate that changes in magmatic strain are accommodated though variations in fault slip, and that ridge morphology is inherently dependent on this relationship. Further, results suggest a form of magmatic segmentation that is partially decoupled from the geometry of the plate boundary. These along-axis variations and the magmatic segmentation exhibited at the Chile Ridge illustrate that mid-ocean ridge processes are inherently three-dimensional. Thus, the last study presented focuses on 3-D geodynamic numerical models of intermediate spreading rate mid-ocean ridges. We model a single ridge segment subjected to an along-axis gradient in the rate of magma injection. Our results illuminate the effects of lithosphere coupling both along and across the ridge axis on faulting and ridge morphology, and provide an explanation for the presence of smaller fault blocks near long-lived detachments faults. Further, models predict an axial valley to form at a depth that increases with the size of faults: individual faults depress the ridge axis, uplift its flanks, and the integrated effect of multiple faults produces most of the axial valley. These three studies motivate future research into post-seismic relaxation, the mechanics of fault weakening and healing, and magma budget variability along slow spreading ridges.

TABLE OF CONTENTS

LIST OF TABLES

LIST OF FIGURES

CHAPTER 1. INTRODUCTION

Tectonic plates are strong slabs of crust and cold mantle, called lithosphere, that are partially decoupled from the motions of the bulk Earth by a weak, partially molten layer called the asthenosphere. Where two adjacent plates are pulled apart from one another, they eventually form a new ocean basin where mid-ocean ridges accommodate the separation of the plates and form volcano chains tens of thousands of kilometers long. Where two adjacent plates move parallel to their shared boundary, transform plate boundaries form and exhibit cycles of plate locking and slipping which produce major earthquakes.

The San Andreas Fault System is one of the best-studied transform plate boundaries on Earth due to the potential for devastating earthquakes near major population centers, including San Francisco and Los Angeles [e.g. *Massonnet et al.*, 1993; *Deng et al.*, 1998; *Fialko et al.*, 2001; *Pollitz et al.*, 2001; *Smith-Konter and Sandwell*, 2006; *Smith-Konter et al.*, 2014; *Tong et al.*, 2014]. To monitor the complex network of locked faults that slowly deform the crust in response to large-scale plate motions, the University NAVSTAR Consortium (UNAVCO) operate EarthScope's Plate Boundary Observatory, comprised of thousands of continuously recording and campaign Global Positioning System (GPS) instruments [*EarthScope-PBO*, 2015]. The horizontal interseismic motions of the fault system are largely predictable and have been the target of numerous investigations of GPS data, but vertical motions arising from tectonic sources remain enigmatic.

Chapter 2 describes a statistical analysis that isolates this tectonic signal from hydrologic and environmental noise. The resulting vertical velocity field demonstrates remarkable agreement with the sense of vertical motions predicted by earthquake cycle models spanning the last few centuries [*Smith and Sandwell*, 2004; *Smith-Konter and Sandwell*, 2006]. This analysis reveals the subtle, but identifiable, tectonic fingerprint of far-field elastic flexure of the plate due to 300+ years of fault locking depth variability. Understanding this critical component of interseismic deformation at a complex strike-slip plate boundary will better constrain regional mechanics and crustal rheology, improving the quantification of seismic hazards in southern California and beyond.

In Chapters 3 and 4, we turn our attention to divergent plate boundaries. Mid-ocean ridges accommodate the separation of oceanic tectonic plates along boundaries tens-of-thousands of kilometers in accumulated length, and are composed of individual spreading segments tens to hundreds of kilometers in length. The hot, ductile asthenosphere below the plates is drawn up beneath the diverging plates, and the resultant decompression melting of mantle rock supplies magmatism to the mid-ocean ridge. Extension is accommodated by normal faulting and the accretion of new rock in zones of deformation a few kilometers wide, referred to as the ridge spreading-axis. The tectonomagmatic processes at the ridge axis influence the formation of median topographic highs, median axial valleys, abyssal hills, and volcanic edifices.

In Chapter 3, we use data from an extensive multibeam bathymetry survey of the Chile Ridge to study tectonomagmatic processes at the ridge axis. Specifically, we investigate how abyssal hills evolve from axial faults, how variations in the amount of extension accommodated magmatically influence morphology and faulting along the spreading axis, and how these variations correlate with the onset and development of ridge segmentation. Our findings suggest that changes in magmatism are accommodated though variations in fault slip, but not fault spacing, and that the depth of the median valley increases with fault slip. Further, results suggest that periodic variations in the amount of extension accommodated magmatically along the ridge segment do not necessarily coincide with tectonic segmentation. We hypothesize that this magmatic segmentation arises from cells of buoyantly upwelling mantle that influence tectonic segmentation from the mantle, up**.** These along-axis variations and the magmatic segmentation exhibited at the Chile Ridge illustrate that mid-ocean ridge processes are inherently three-dimensional, especially at slow and intermediate plate separation rates.

Previous two-dimensional modeling studies of fault generation and lithosphere bending at mid-ocean ridges broadly explain the globally observed trends in abyssal hill spacing and ridge axis morphology [e.g. *Chen and Morgan*, 1990a; b; *Shaw and Lin*, 1993; *Buck et al.*, 2005b; *Behn and Ito*, 2008; *Ito and Behn*, 2008]. However, these modeling efforts did not address how changes in magma supply along a ridge segment lead to the inherently 3D variability of faulting and axial morphology at intermediate and slow-spreading ridges. To this end, in Chapter 4 we use the geodynamic modeling software Lithosphere and Mantle Evolution Model (LaMEM) [*Kaus et al.*, 2016] to simulate high-resolution, 3-D tectonomagmatic interactions in a visco-elasto-plastic lithosphere under extension.

We model a single ridge segment subjected to an along-axis gradient in the rate of magma injection. Our results illuminate the effects of lithosphere coupling both along and across the ridge axis on faulting and ridge morphology, and provide an explanation for the presence of smaller fault blocks near long-lived detachments faults. Further, these models are among the first to emphasize that the depth of the axial valley should increase with the size of normal faults. Describing the effect that lithosphere coupling has on the tectonic, magmatic, and topographical structure of the ridge motivates further investigations into along-axis variations in the magmatic budget of slow-spreading ridges and the evolution of the fault zones themselves.

The investigations and results presented here have wide-reaching implications for processes at both transform and divergent plate boundaries. The study of the San Andreas Fault System (Chapter 2) has already sparked public interest in better understanding the observed vertical motions, and will act to guide future instrument deployment and contribute to reports of seismic hazards and sea level rise in southern California. Additionally, our survey of the seafloor at the Chile Ridge (Chapter 3) uncovered novel links between mantle chemistry and faulting on the surface, provided evidence for a new conceptual model of abyssal hill formation and growth, and further demonstrated that mid-ocean ridge processes are inherently three-dimensional. Finally, our numerical models of these three-dimensional processes (Chapter 4) highlight the importance of lithosphere coupling, predict that axial morphology is directly related to the vertical relief on faults, and motivate future studies of rock mechanics and magmatic processes.

CHAPTER 2. THE VERTICAL FINGERPRINT OF EARTHQUAKE CYCLE-INDUCED LOADING OF THE SAN ANDREAS FAULT

Abstract

The San Andreas Fault System, one of the best-studied transform plate boundaries on Earth, is well known for its complex network of locked faults that slowly deform the crust in response to large-scale plate motions. Horizontal interseismic motions of the fault system are largely predictable, but vertical motions arising from tectonic sources remain enigmatic. Here we show that when carefully treated for spatial consistency, GPS-derived vertical velocities expose a small-amplitude (±2 mm/yr), but spatially considerable (200 km), coherent pattern of uplift and subsidence straddling the fault system in southern California. We employ the statistical method of model selection to isolate this vertical velocity field from non-tectonic signals that induce velocity variations in both magnitude and direction across small distances (<10s km), and find remarkable agreement with the sense of vertical motions predicted by physical earthquake cycle models spanning the last few centuries. We suggest that these motions reveal the subtle, but identifiable, tectonic fingerprint of far-field flexure due to 300+ years of fault locking and creeping depth variability. Understanding this critical component of interseismic deformation at a complex strike-slip plate boundary will better constrain regional mechanics and crustal rheology, improving the quantification of seismic hazards in Southern California and beyond.

As published in: Howell, S., B. Smith-Konter, N. Frazer, X. Tong, and D. Sandwell (2016), The vertical fingerprint of earthquake cycle loading in southern California, *Nature Geosci*., doi: 10.1038/ngeo2741

2.1. Introduction

The San Andreas Fault System, one of the best-studied transform plate boundaries on Earth, is well known for its complex network of locked faults that slowly deform the crust in response to large-scale plate motions [*Massonnet et al.*, 1993; *Deng et al.*, 1998; *Fialko et al.*, 2001; *Pollitz et al.*, 2001; *Johnson and Segall*, 2004; *Smith-Konter and Sandwell*, 2006; *Tong et al.*, 2013; *Smith-Konter et al.*, 2014]. Horizontal interseismic motions of the fault system are largely predictable, but vertical motions arising from tectonic sources remain enigmatic. Here we show that when carefully treated for spatial consistency, GPS-derived vertical velocities expose a small-amplitude (±2 mm/yr), but spatially considerable (200 km), coherent pattern of uplift and subsidence straddling the fault system in southern California. We employ the statistical method of model selection to isolate this vertical velocity field from non-tectonic signals that induce velocity variations in both magnitude and direction across small distances (<10s km) [*Blume et al.*, 2013], and find remarkable agreement with the sense of vertical motions predicted by physical earthquake cycle models spanning the last few centuries [*Smith and Sandwell*, 2004; *Smith-Konter and Sandwell*, 2006]. We suggest that these motions reveal the subtle, but identifiable, tectonic fingerprint of far-field flexure due to 300+ years of fault locking and creeping depth variability. Understanding this critical component of interseismic deformation at a complex strike-slip plate boundary will better constrain regional mechanics and crustal rheology, improving the quantification of seismic hazards in Southern California and beyond.

Crustal motions surrounding the San Andreas Fault System (SAFS) in southern California are densely sampled by EarthScope's Plate Boundary Observatory (PBO) GPS array, providing high-quality, well-behaved horizontal surface velocity solutions spanning a major and active transform plate boundary. When imposed as boundary conditions on physical models of deformation throughout the earthquake cycle (interseismic strain accumulation, coseismic displacement, and postseismic relaxation), these velocity measurements can be used to constrain the SAFS's faulting characteristics (e.g., slip rates, fault locking depths [*Smith-Konter and Sandwell*, 2006; *Tong et al.*, 2014]) and lithospheric rheology (e.g., crust/mantle viscosities and thicknesses [*Deng et al.*, 1998; *Pollitz et al.*, 2001; *Johnson and Segall*, 2004; *Hetland and Hager*, 2005; *Smith-Konter and Sandwell*, 2006]).

While vertical deformation from earthquake cycle loading is a measurable process at subduction zone plate boundaries, where steady interseismic motion is augmented by step displacements during an earthquake [*Melini et al.*, 2004; *Sieh et al.*, 2008], vertical deformation at transform plate boundaries is much more challenging to detect [*Pollitz et al.*, 2001]. Unlike the smooth, predictable crustal motions exhibited by the horizontal velocity field, PBO vertical velocity data are typically dominated by short wavelength (<10s km), non-tectonic signals that potentially mask underlying long wavelength tectonic deformation (Figure 2.1).

Recently, several high-profile studies have used vertical velocity measurements to investigate groundwater storage and depletion in California [*Amos et al.*, 2014; *Argus et al.*, 2014; *Borsa et al.*, 2014]. However, no such study has investigated the large-scale tectonic component of vertical rates along the SAFS, which we suggest contains a dominant and smoothly varying signal from earthquake cycle loading.

2.2. Statistical analysis of vertical GPS velocities

2.2.1. Statistical approach

To inspect the vertical motions associated with the SAFS earthquake cycle, we utilized published EarthScope PBO GPS vertical velocity estimates (epoch year 2014 [*EarthScope-PBO*, 2015]). We first omitted GPS stations likely affected by non-tectonic sources of deformation based on anomalies revealed by high-resolution InSAR data [*Tong et al.*, 2013], as well as stations with velocities >5 mm/yr and low signal-to-noise ratios (≤5:1). We then processed the remaining stations into a local reference frame (115 – 121°W, 32 – 36°N) by removing the mean velocity of the remaining stations. Vertical GPS measurements are known to be sensitive to a variety of factors (i.e., variations in GPS monument type and stability, monument substrate material, local surface geology, proximity to reflectors, ionospheric and tropospheric signal delays, satellite orbits, and response to local changes in water-storage, pore pressure, precipitation, and water runoff), all of which can introduce complex and widely varying vertical signals [*Blume et al.*, 2013].

As non-tectonic signals appear to dominate the first-order vertical velocity field of the SAFS, we employed the statistical method of model selection to carefully distinguish more subtle long-wavelength signals that could be of tectonic origin [*Burnham and Anderson*, 2002]. Model selection provides an objective estimate of the velocity field that optimizes goodness of fit while penalizing model complexity, as measured by the number of model terms [*Burnham and Anderson*, 2002; 2004]. We inverted the velocity data to obtain phenomenological statistical model (s-model) surfaces of increasing complexity that minimized the sum of squared residuals of the data and the s-model on a 1 km spaced grid spanning the 560 × 440 km study area. As the complexity of the s-model increased, the fit necessarily improved, and so did the likelihood of over-fitting the dominant short spatial-scale variations.

Thus, the sample size corrected Akaike Information Criterion was used to select the point at which increasing the number of model terms did not improve the fit sufficiently enough to warrant a higher order model [*Burnham and Anderson*, 2004]. The resultant s-model contains 15 terms (Appendix 3.1).

2.2.2. Statistical method

The premise of this study relies on nested models of the form

$$d(x, y) = \beta_0 + \beta_1 x + \beta_2 y + \beta_3 xy + \beta_4 x^2 + \beta_5 y^2 + \beta_6 x^2 y + \beta_7 x y^2 + \ldots + \varepsilon \tag{1}$$

where the data vector, d, is the GPS measured vertical velocity at location (x, y), β_m are the least squares polynomial coefficients to invert for, and ε characterizes the data noise about the modeled surface. The model order, l, is the sum of the exponents of the highest-order term. For example, the model ending with the term xy^2 is considered to be order $l = 3$. For increasing model order, cross terms are added first, then terms with higher powers of x than y, and finally those with higher powers of y than x. The terms for model order $l = 2$ would thus be arranged $\beta_3 xy + \beta_4 x^2 + \beta_5 y^2$ as above.

We begin with the linear equation

$$d = G m + \varepsilon, \tag{2}$$

where G is the design matrix, with columns comprised of the independent terms (x_n, y_n) in Eq. 1, and m is a vector of polynomial coefficients β_m.

$$\begin{bmatrix} d_1 \\ d_2 \\ d_3 \\ \vdots \\ d_N \end{bmatrix} = \begin{bmatrix} 1 & x_1 & y_1 & x_1 y_1 & x_1^2 & \dots \\ 1 & x_2 & y_2 & x_2 y_2 & x_2^2 & \dots \\ 1 & x_3 & y_3 & x_3 y_3 & x_3^2 & \dots \\ \vdots & \vdots & \vdots & \vdots & \vdots & \ddots \\ 1 & x_N & y_N & x_N y_N & x_N^2 & \dots \end{bmatrix} \begin{bmatrix} \beta_1 \\ \beta_2 \\ \beta_3 \\ \vdots \\ \beta_M \end{bmatrix} + \ \varepsilon. \tag{3}$$

Here, G is $N \times M$, where N is the number of GPS data in d, and M is the number of coefficients being solved for. Before building the design matrix, the latitude and longitude of each data point were converted to UTM zone 11S easting (x) and northing (y) to provide an isotropic Cartesian coordinate system. The coordinate positions then had their mean removed and were scaled to unit variance to ensure stability of the inversion. We repeated this process with a rotation of the design matrix into a coordinate system that minimized areas of the modeled region with no data (white space) to ensure that the results were not affected by artifacts of the grid orientation. After building the design matrix, Eq. 2 was inverted for the least squares solution of m

$$m = (G^T G)^{-1} G^T d. \tag{4}$$

This inversion was performed for $K = 2$ to 751 (through polynomial orders up to $l=38$), where K is the number of parameters used in the model, M, plus one (we independently estimated data noise from the inversion). The criterion for model selection used in this study was the sample-size corrected Akaike Information Criterion, AICc [*Burnham and Anderson*, 2002; 2004; *Gelman et al.*, 2014],

$$\mathrm{AICc} = N \ln(\mathrm{RSS/N}) + 2KN/(N–K–1), \tag{5}$$

in which RSS is the residual sum of squared prediction errors. The first term in the AICc penalizes models that fit poorly, as measured by high RSS/N, while the second term penalizes model complexity, as measured by high K. Minimizing the AICc then yields the s-model that best fits, but does not overfit, the data; it is the simplest model that explains the correlated velocity field.

The variance of the sampling distribution (signal noise) was estimated using the explained sum of squares [*Akaike*, 1974], ESS,

$$\mathrm{ESS} = (N\text{-}K)^{-1}\,(G\,m - y)^{\mathrm{T}}\,(G\,m - y). \tag{6}$$

In order to produce an s-model surface and surface of standard deviation calculated on an evenly spaced UTM grid that spans the region containing the GPS data, we first calculate the covariance matrix, C_m, of the posterior distribution of parameters:

$$C_m = (G^{\mathrm{T}}\,(C_n)^{-1}\,G)^{-1}. \tag{7}$$

Here C_n is the covariance of the signal noise, ESS I_N. We then constructed a 1 km spaced UTM grid that spans the study area to populate a new design matrix, G', at N' locations, and calculated the selected model vertical velocities, d', on the grid, as well as the covariance of the s-model prediction, $C_{d'}$,

$$d' = G'\,m + \varepsilon', \tag{8}$$

$$C_{d'} = G'^{\,\mathrm{T}}\,C_m\,G' + C_{n'},$$

in which $C_{n'}$ = ESS $\mathrm{I}_{N'}$.

At every grid location, we computed one standard deviation in the prediction of GPS velocities from the predicted model surface using the prediction covariance. Grid coordinates were fed as x, y pairs into the design matrix, G', at locations where we predicted the coherent velocity field values, y'. The easting and northing positions were then scaled back to their true mean and variance before being converted to latitude and longitude. Results of this statistical technique for example model orders are provided in Table 2.1, Figure 2.2.

We tested the sensitivity of this method to short-wavelength vertical velocity signals using synthetic data. We interpolated 5 mm/yr squares of increasing edge length (10 km – 100 km) at the center of the model domain to the GPS station locations and performed model selection on nested polynomials. The approach consistently selected high-order polynomial models that fit the square vertical velocity anomalies. When modeling the synthetic data using only the long-wavelength polynomial chosen for the GPS data used in this study (15th order), features smaller than the ~100 – 200 km wavelength of the model were smeared into broad, low amplitude signals that would have a negligible effect on the overall solution. For example, a 50 × 50 km square of 5 mm/yr is averaged into a ~150 × 200 km region of uplift with an amplitude of 0.4 mm/yr.

For independent verification of these modeling results, we also used Generic Mapping Tools (GMT) 2D Green's function spline function "greenspline" [*Wessel*, 2009], as well as the thin plate splining function "tpaps" in MATLAB 2014b [*MATLAB*, 2014]. Both techniques provided qualitative and quantitative verification of the long-wavelength quadrant pattern revealed by model selection (see Figure 2.2). GMT's greenspline tool for continuous curvature splines and MATLAB's tpaps tool for thin plate splines produce a smoothed data surface that lies between the two extremes where the model output is equal to the model input and where the model output has zero curvature. While these functions do not use a robust information criterion, the smoothing value chosen is a relatively good starting guess for the value that optimizes goodness of fit while best penalizing high spline curvature.

2.2.3. Statistical results

This optimal s-model (Figure 2.3a) reveals a distinct, smoothly-varying quadrant pattern of uplift and subsidence in the southern California vertical velocity field, while excluding the higher-order signals which dominate the visual scatter of the data. The northwest and east quadrants of the s-model show ~200 km diameter “lobes” of uplift (maximum 1.9, median 0.6 mm/yr), while the north and southwest quadrants reveal similar-sized lobes of subsidence (minimum -2.1, median -0.4 mm/yr). Smaller amplitude, shorter wavelength postseismic deformation following the 1992 M7.3 Landers and 1999 M7.1 Hector Mine earthquakes may also influence the solution obtained with higher order models, but these local patterns are smoothed into the broader regional pattern at the preferred model order. Because results obtained with this approach can be mildly affected by model order, these results were also verified independently using splining techniques [*Wessel*, 2009; *MATLAB*, 2014].

2.3. 3-D earthquake cycle deformation model

2.3.1. Physical modeling approach

Using a semi-analytical physical model (p-model) representing 3-D elastic-viscoelastic earthquake cycle deformation [*Smith and Sandwell*, 2004; *Smith-Konter and Sandwell*, 2006] that includes the restoring force of gravity [*Sandwell et al.*, 2012], we calculated the present-day vertical velocity field from an a priori inversion of horizontal PBO velocity data [*Tong et al.*, 2014]. Interseismic deep slip below locked fault patches generates the first-order orientation and magnitude of this velocity field, while second-order effects arise from local slip-rate variability, earthquake cycle viscoelastic relaxation, and abrupt changes in fault locking depth (Figures 2.3b, 2.4; 2.5).

2.3.2. Physical modeling method

We model the North American-Pacific plate boundary as a series of vertical connected faults embedded in an elastic plate overlying a viscoelastic half-space [*Smith-Konter and Sandwell*, 2006]. The 4-dimensional model simulates interseismic strain accumulation, coseismic displacement, and post-seismic viscous relaxation of the mantle. The mathematical deformation solution is analytic in the vertical and time dimensions, while the solution in the two horizontal dimensions is provided in the Fourier transform domain [*Steketee*, 1958; *Smith and Sandwell*, 2003; 2004]. The solution satisfies the zero traction surface boundary condition [*Williams and Richardson*, 1991; *Richards-Dinger and Shearer*, 2000; *Wdowinski et al.*, 2007; *Smith-Konter et al.*, 2011] and maintains stress and displacement continuity across the base of the plate [*Smith and*

Sandwell, 2004]. A far-field velocity step across the plate boundary of 45 mm/yr is simulated using a cosine transform in the *x* direction (i.e., across the plate boundary). A uniform far-field velocity boundary condition at the top and bottom of the grid is simulated by arranging the fault trace to be cyclic in the *y* direction (i.e., parallel to the plate boundary). The numerical aspects of this approach involve generating a grid of vector force couples that simulate complex fault geometry, taking the two dimensional (2D) horizontal Fourier transform of the grid, multiplying by the appropriate transfer functions and time-dependent relaxation coefficients, and finally inverse Fourier transforming to obtain the desired results [*Smith and Sandwell*, 2004]. Fault elements are embedded in an elastic plate and a displacement discontinuity across each fault element is simulated using a finite width force couple embedded in a fine grid [*Smith and Sandwell*, 2004]. Because the computational aspects of the model are only 2D, the entire plate boundary (2048 km by 1024 km, 1 km cell size) can be simulated very efficiently.

Faults within the elastic plate extend from the surface to a prescribed locking depth. Below this, fully relaxed secular slip (assuming infinite time) takes place down to the base of the elastic plate. Assumed quantities of the homogeneous elastic plate are a Young's modulus of 70 GPa and a shear modulus of 30 GPa [*Boussinesq*, 1885; *Smith-Konter and Sandwell*, 2006]. Coseismic slip is kinematically prescribed along fault segments with known historical ruptures. Transient deformation follows each earthquake due to viscoelastic flow in the underlying half-space. The duration of the viscoelastic response, characterized by the Maxwell time, depends on the viscosity of the underlying half-space and the elastic plate thickness (see Figure 2.6 for model parameter comparison). The Maxwell rheology used is consistent with viscoelastic post-seismic studies of Southern California [*Burmister et al.*, 1944; *Weertman*, 1964; *Rundle and Jackson*, 1977; *Fay and Humphreys*, 2005]. Full details of this model are provided in previous studies [*Smith and Sandwell*, 2003; *Smith-Konter and Sandwell*, 2006].

The model is purely kinematic; slip on faults is prescribed based on geologic, geodetic, and historical seismic data. Deep slip along the plate boundary (below the locking depth) drives the secular interseismic crustal block motions. Long-term slip rates (i.e. over many earthquake cycles) are constrained by geologic estimates [*Pollitz*, 2003] and geodetic velocity measurements [*Tong et al.*, 2014]. Small adjustments to local fault geometry to account for fault step-overs [*Tong et al.*, 2013] were adopted in the present-day velocity model (Figure 2.5). Fault segments were locked from the surface down to a variable locking depth, which was tuned to match the present-day EarthScope PBO GPS measurements [*Tong et al.*, 2014]. Note that earthquake cycle effects [*Pollitz*, 2005; *Hearn et al.*, 2009], as well as a smooth transition from locked to unlocked fault[42], are known to complicate estimations of true locking depth. Apparent locking depths range between 0 and 22 km, and are primarily consistent with seismicity depths [*Savage*, 1990; *Probabilities*, 2008] and provide an RMS residual velocity model misfit of less than 2 mm/yr [*Tong et al.*, 2014]. The model accounts for recent postseismic vertical motions from the Hector Mine and Landers events, which contribute less than, on average, 0.2 mm/yr of localized uplift and subsidence at the ends of each rupture.

Traditionally, this model has been used to investigate 1000-year earthquake cycle viscoelastic deformation of the San Andreas Fault System (SAFS) [*Smith and Sandwell*, 2003; *Smith-Konter and Sandwell*, 2006; *Smith-Konter et al.*, 2014]. For a purely elastic model, deep interseismic slip below a locked fault produces narrow regions of uplift along compressional bends and subsidence along tensile regimes. This is a known and intuitive result of elastic half-space deformation models [*Smith and Sandwell*, 2003; *Meade and Hager*, 2004]. For example, large mountain ranges north of Los Angeles are recognized to be a result of compressional uplift along the Big Bend of the SAFS. To obtain this same physical behavior using a viscoelastic layered model that includes the effect of gravity, however, requires an omission of east-west directed body forces that comprise the deep interseismic slip (below the locking depth) mode of the model. When the SAFS is projected into a pole-of-deformation model space [*Savage*, 2006] (which aligns the fault system in a predominantly N-S direction), only regions with large deviations in orientation from north are impacted by this technique, such as the Big Bend. The end result is a realistic near-field uplifting zone along the Big Bend that simulates geologic uplift in this compressive region [*Smith and Sandwell*, 2003; *Smith-Konter and Sandwell*, 2006; *Smith-Konter et al.*, 2014], in addition to a far-field quadrant pattern of alternating uplift and subsidence zones due to earthquake cycle interactions of adjacent fault segments. Geodetic data, however, largely report motions occurring over earthquake cycle timescales (10s – 100s years), not necessarily motions occurring on geologic timescales (1000s+ years), as is evident from the lack of strong uplift (and noticeable subsidence) present in the PBO data straddling the Big Bend of the SAFS. To significantly improve our modeling fit in this region, and to ultimately focus our analysis to deformation expected over realistic earthquake cycle timescales, we restored the deep-seated east-west body forces that act below the locking depth of the fault system. This resulting viscoelastic vertical deformation field yields a dominant far-field quadrant pattern of uplift and subsidence with no localized near-field uplift along the Big Bend, in strong agreement with modern GPS observations.

2.3.3. Physical modeling results

The p-model shows two large lobes of uplift (maximum 0.9, median 0.3 mm/yr) and subsidence (minimum -0.7, median -0.2 mm/yr) in response to the interseismic loading history of the SAFS. The geometry of the p-model vertical velocity lobes varies with assumed lithospheric thickness, while the magnitude of uplift and subsidence varies with asthenospheric viscosity and prescribed fault locking depth. If another significant event like the 1857 rupture occurs, the moment will extinguish and the vertical lobate pattern will relax over the Maxwell timescale [*Smith and Sandwell*, 2004].

2.4. Model comparison and discussion

Although this clear quadrant pattern of vertical motions straddling the SAFS may seem perplexing, similar, but smaller-scale, patterns of uplift and subsidence have been observed for large strike-slip earthquakes as a result of coseismic fault slip and postseismic viscoelastic relaxation [*Massonnet et al.*, 1993; *Deng et al.*, 1998; *Fialko et al.*, 2001; *Pollitz et al.*, 2001; *Freed and Burgmann*, 2004]. Likewise, interseismic strain accumulation at depth can generate long-wavelength, low-magnitude quadrant lobate patterns in vertical velocity that arise from a major transition in locking-creeping depth [*Smith and Sandwell*, 2004; *Smith-Konter and Sandwell*, 2006] (Figure 2.4). Along the SAFS, variations in fault locking depth, constrained by horizontal GPS and InSAR data [*Smith-Konter and Sandwell*, 2006; *Tong et al.*, 2014], are well documented, extending fromthe Salton Trough to Parkfield, where the upper ~10 – 15 km of the fault has remained locked since at least the 1857 M7.9 Fort Tejon rupture (Figure 2.7). Critical to this study, however, are the major sections of fault creep bounding this locked zone: the `Creeping' segment north of Parkfield [*Moore and Rymer*, 2007] and shallow creep accommodated by the collection of faults that bound the southern edge of the Salton Trough (Superstition Hills, Brawley, Imperial, and Cerro Prieto segments) [*Lyons et al.*, 2002].

The first-order vertical velocity trends predicted by the p-model are remarkably consistent with those preferred by the GPS-derived s-model. Quantitative comparisons (mean residual, ratio of uplift and subsidence medians, and alignment) of the s-model with a suite of different p-model rheologies (elastic plate thicknesses of 30 – 70 km and asthenospheric viscosities of 3×10^{18} – 3×10^{19} Pa-s) provide critical insight into the overall agreement between model and data. The alignment was calculated as the fraction of the study region where both the s-model and p-model predicted the same direction of vertical motion. We found that the residual norm is minimized and the alignment maximized for a p-model with a 50 km thick lithosphere overlying a 1×10^{19} Pa-s asthenosphere (Figure 2.3b), consistent with previous work [*Smith-Konter and Sandwell*, 2006; *Smith-Konter et al.*, 2014; *Tong et al.*, 2014]. We also found that the p-model underpredicted median uplift and subsidence by greater than a factor of 2 compared to the s-model. The source of this difference is not well resolved, although it may be partially attributed to an over-estimation of elastic plate thickness; a thinner elastic plate will yield higher velocity amplitudes at the expense of a smaller-wavelength deformation pattern.

2.5. Conclusions

It is remarkable that the physical (p-) earthquake cycle models, constrained using only horizontal interseismic GPS measurements, accurately predict the appropriate sense, relative magnitude, and spatial pattern of far-field vertical velocity variations exhibited by the optimal statistical (s-) model. Such agreement has several important implications. First, vertical GPS observations, although noisy by nature, are capable of documenting elastic plate flexure caused by bending moments applied at the ends of locked sections of faults. Lateral variations in vertical velocities of such extent may have significant bearing on studies of glacial melting and sea level change [*Peltier*, 1998; *Conrad*, 2013]. Second, the agreement between data and models suggests that the earthquake cycle loading process, including the role of gravity-induced plate flexure and fault locking depth variability, is sufficiently well-understood to predict complex patterns of vertical deformation. Third, recent studies of vertical GPS velocities in California largely attribute long-wavelength uplift and subsidence signals to the isostatic response of the crust to changes in the storage and discharge of groundwater [*Amos et al.*, 2014; *Argus et al.*, 2014; *Borsa et al.*, 2014]. These studies have been critical to advancing our understanding of groundwater use and replenishment, and the extent of the ongoing historic drought affecting the region. However, elastic models of crustal rebound due to San Joaquin water extraction, for example, have underpredicted vertical GPS velocities in some regions by almost 2 mm/yr, leaving open the possibility of a time-dependent tectonic contribution [*Amos et al.*, 2014]. Given the contribution of vertical motions from the historical earthquake cycle demonstrated in this study, the dominant sources of vertical deformation in California are likely a combination of long-wavelength groundwater-induced isostasy and regional earthquake cycle strain of the many active faults within the SAFS. Finally, the current GPS array is ideally situated to map and model the large-scale time-dependent relaxation of the mantle resulting from the next significant rupture of the SAFS. These results have implications for seismic moment deficit [*Tong et al.*, 2015] and seismic hazard mitigation of active faults in southern California.

2.6. Tables and figures

Table 2.1. Model comparison results. Mean residual and model alignment between preferred order 15 s-model and each of the 9 tested p-models. Here, alignment is the percent of the study region where the s- and p-models predict the same sense of motion.

Model		Mean Residual [mm/yr]	% Alignment
H [km]	η [Pa-s]		
30	3×10^{18}	1.25	62
30	1×10^{19}	0.52	63
30	3×10^{19}	0.56	60
50	3×10^{18}	0.84	55
50	$\mathbf{1\times10^{19}}$	**0.44**	**76**
50	3×10^{19}	0.52	66
70	3×10^{18}	0.69	55
70	1×10^{19}	0.48	71
70	3×10^{19}	1.74	64

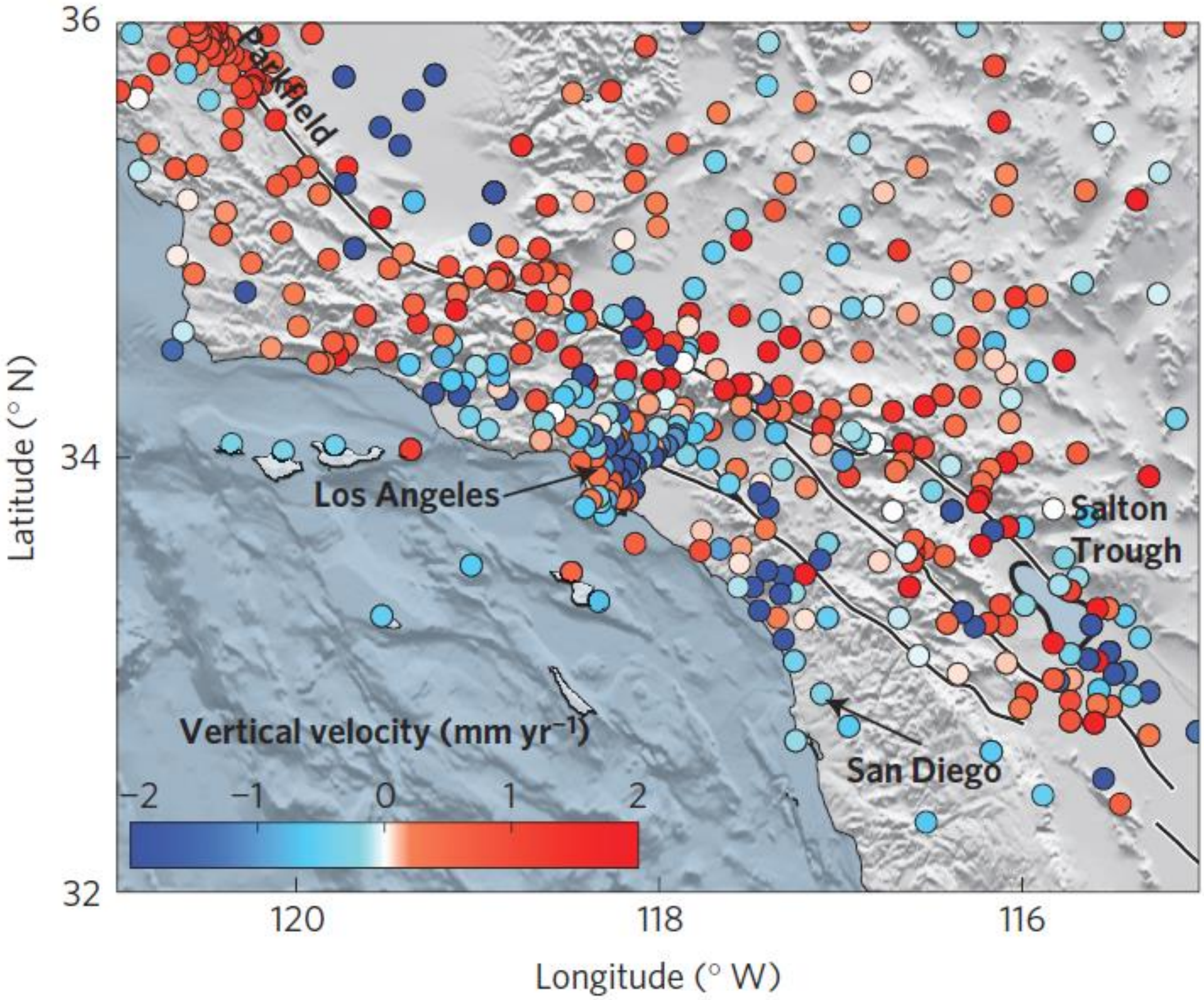

Figure 2.1. Southern California vertical GPS velocity data. Unfiltered vertical EarthScope PBO GPS velocities in Southern California, revealing sporadic variation over distances of 10s of km, attributed to non-tectonic signals.

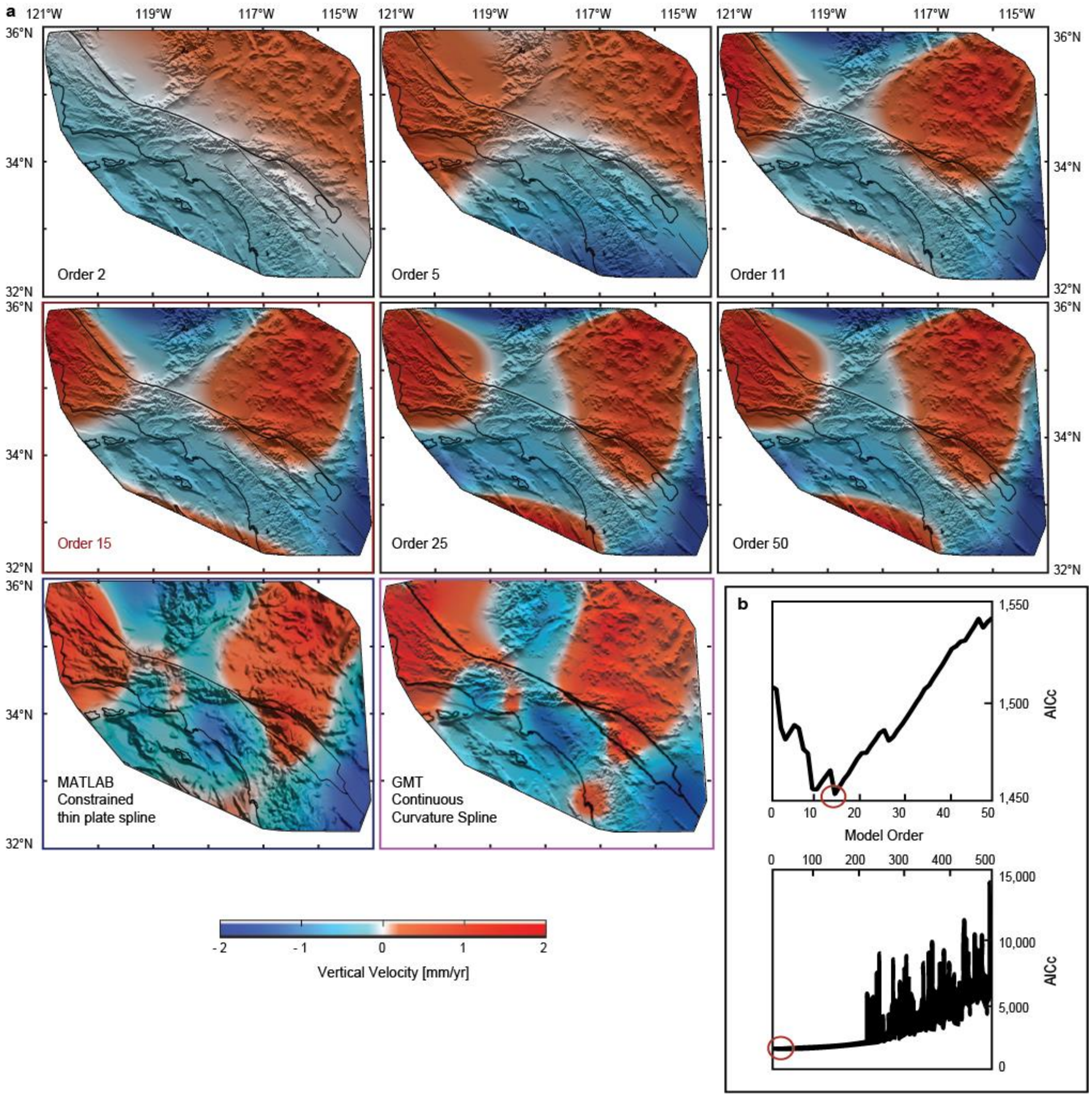

Figure 2.2. Statistical modeling results. (a) Statistical models for different model selection orders (top two rows), with preferred model order 15 highlighted (red box), and splines used for independent verification of results, including a constrained thin plate spline result (blue box) produced with MATLAB's tpaps, and a continuous curvature spline (purple box) produced with GMT's greenspline tool. (b) Sample-size corrected Akaike Information Criterion (AICc) showing a global minimum at model order 15.

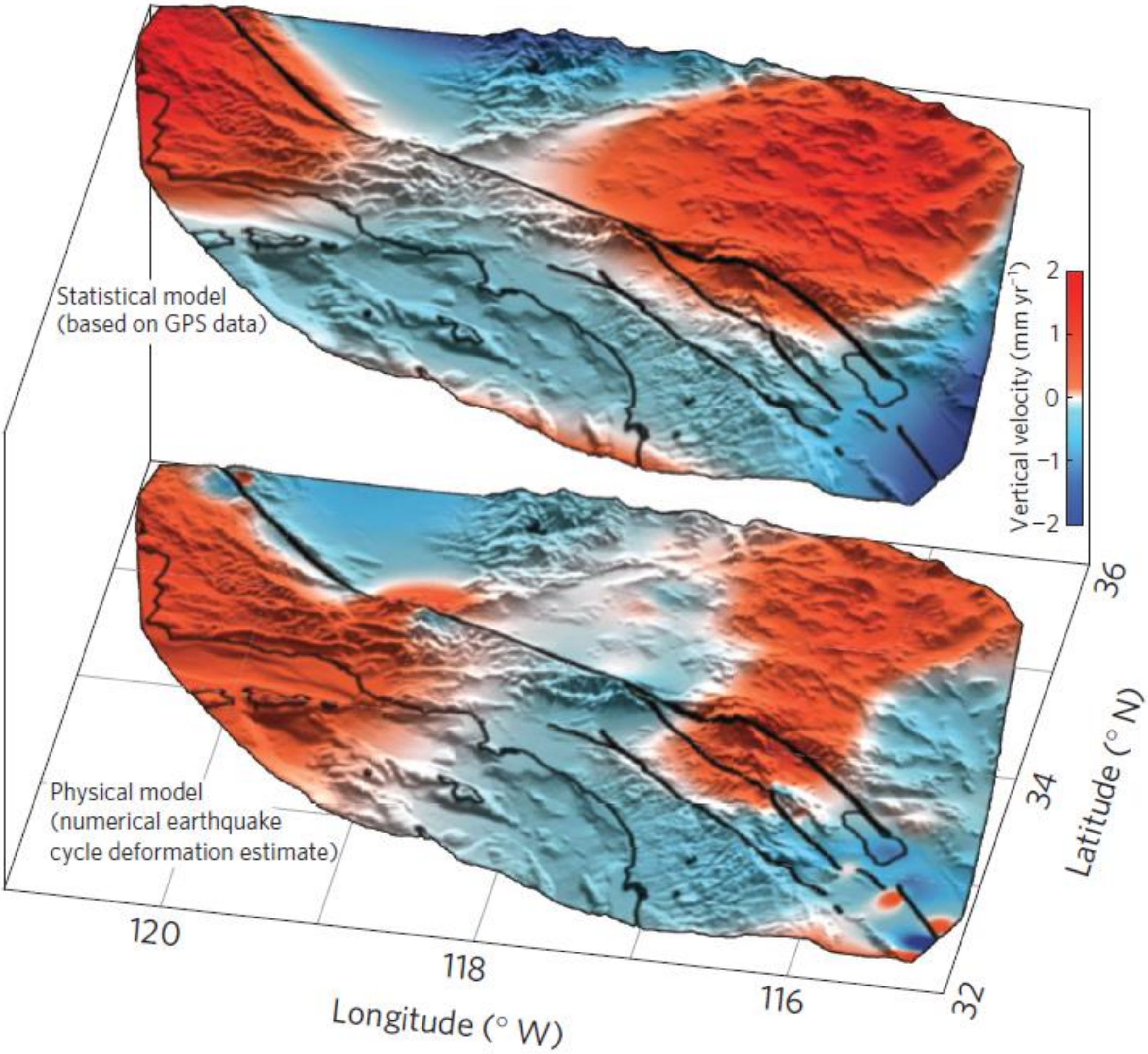

Figure 2.3. GPS and physical model comparison. Vertical velocities predicted by model selection (statistical, s-model) using GPS data and the best-fitting physical deformation model (p-model) simulating the vertical crustal response of earthquake cycle loading at depth throughout the last 300+ years. The p-model velocity estimate represents regional vertical motion due to the interaction of creeping and locked faults embedded within a 50 km thick elastic plate overlaying an asthenosphere with a viscosity of 1×10^{19} Pa-s. Vertical velocity estimates overlaying shaded topographic relief are saturated near +/- 1.5 mm/yr to highlight agreement in the sense of motion between data and model predictions.

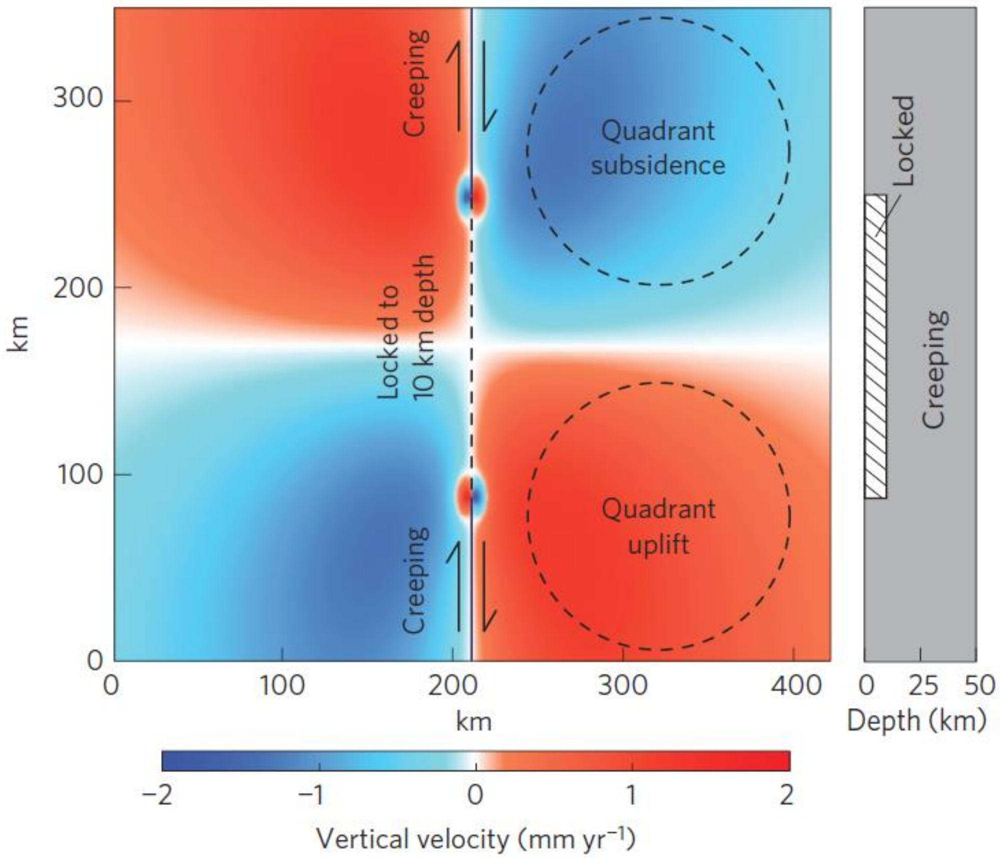

Figure 2.4. Simplified physical model vertical velocity pattern. (Left) Map view representation of interseismic quadrant lobate patterns of vertical motion from bending moments induced by variations in fault locking (or creeping) depth. (Right) Cross-section view of fault geometry. Here a centrally locked fault extends from the surface to 10 km depth and is embedded within a 50 km thick elastic plate overlaying an asthenosphere with a viscosity of 1×10^{19} Pa-s. The fault is surrounded by top-to-bottom creeping zones to the north and south.

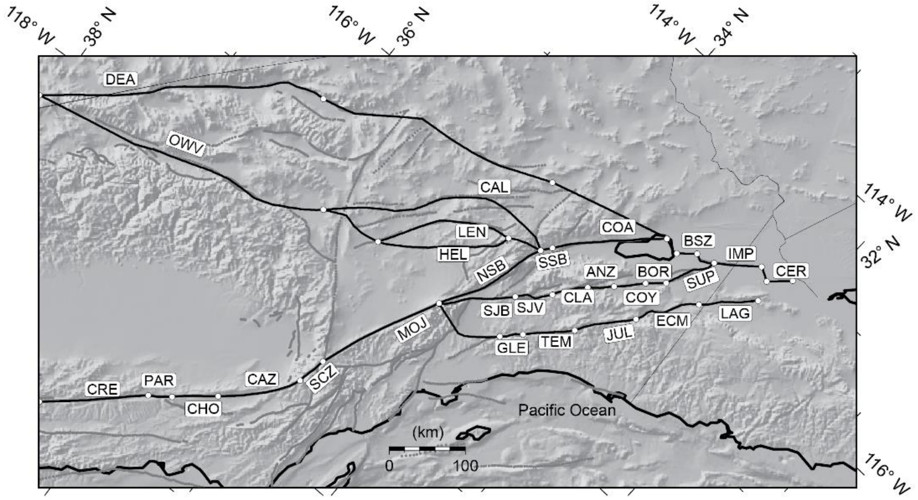

Fault label	Fault name
CER	Cerro Prieto
IMP	Imperial
BSZ	Brawley
COA	Coachella
SSB	South San Bernardino
NSB	North San Bernardino
SUP	Superstition Hills/Mount
BOR	Borrego Mountain
COY	Coyote Creek
ANZ	Anza
CLA	Clark
SJV	San Jacinto Valley
SJB	SJ San Bernardino Valley
MOJ	Mojave
SCZ CAZ	S. Carrizo (Big Bend)
CHO	Carrizo
PAR	Cholame
CRE	Parkfield
LAG	Creeping
GLE	Glen Ivy
TEM	Temecula
JUL	Julian
ECM	Coyote Mountain
LEN	Lenwood/Lockhart/Old Woman Spring
HEL	Helendale
CAL	Calico/Hidalgo
OWV	Owens Valley
DEA	Death Valley

Figure 2.5. Schematic of SAFS fault segments used in physical deformation models. Figure adapted from Tong et al. (2014, with permission), where black lines represent the fault segments used in the physical deformation model, represented by a three-character label. For additional fault model details See *Tong et al.* [2014].

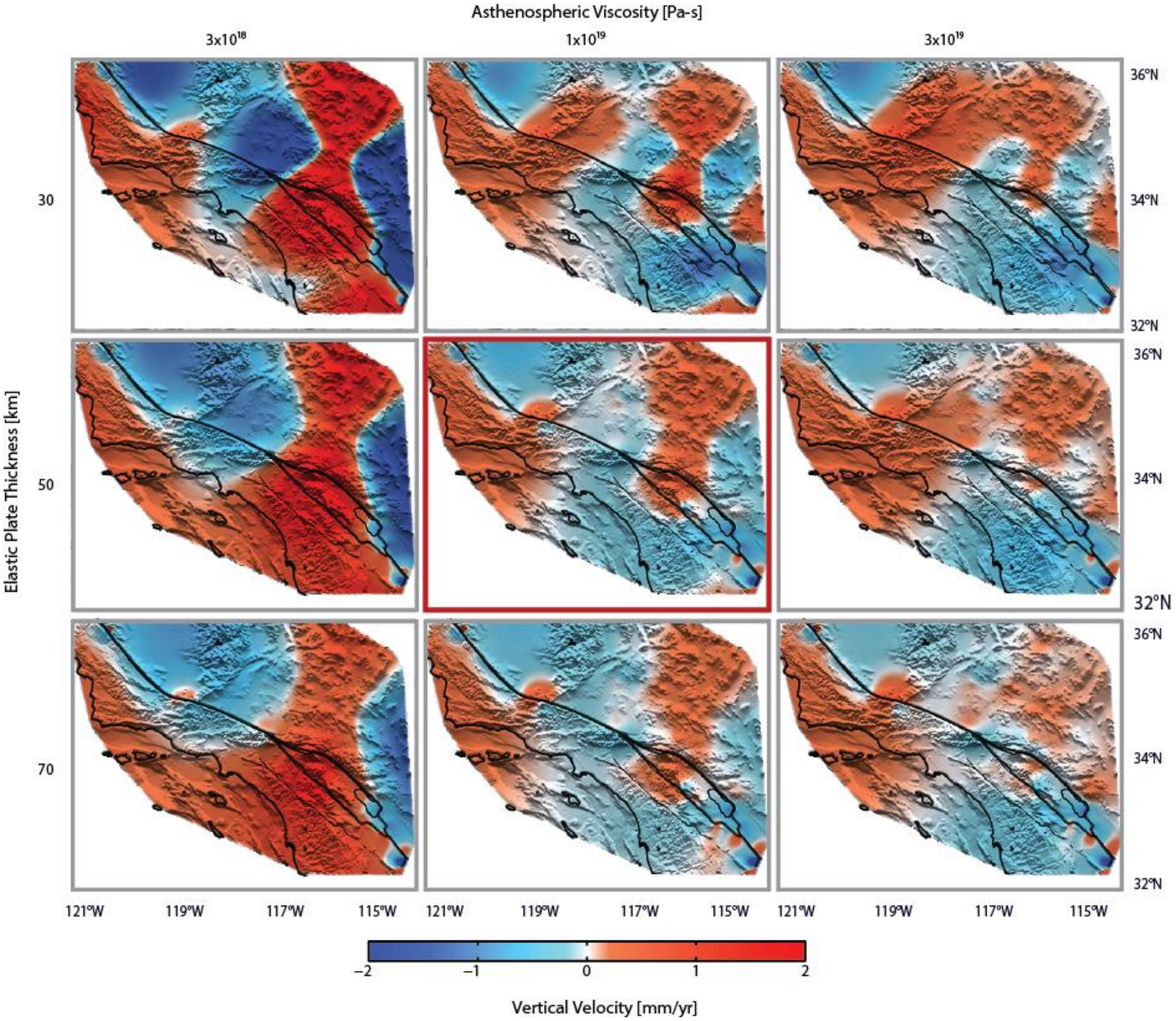

Figure 2.6. 3-D earthquake cycle deformation modeling results. 3D semi-analytic physical models of viscoelastic vertical deformation in response to the past few centuries of earthquake cycle loading (variations in locking depth and historical ruptures). Example models illustrate deformation variations arising from an elastic plate with a thickness of 30-70 km overlaying a viscoelastic asthenosphere with a viscosity of $3x10^{18}$ – $3x10^{19}$ Pa-s. The model in the center panel (red outline) minimizes data residuals while maximizing alignment (See Table 2.1).

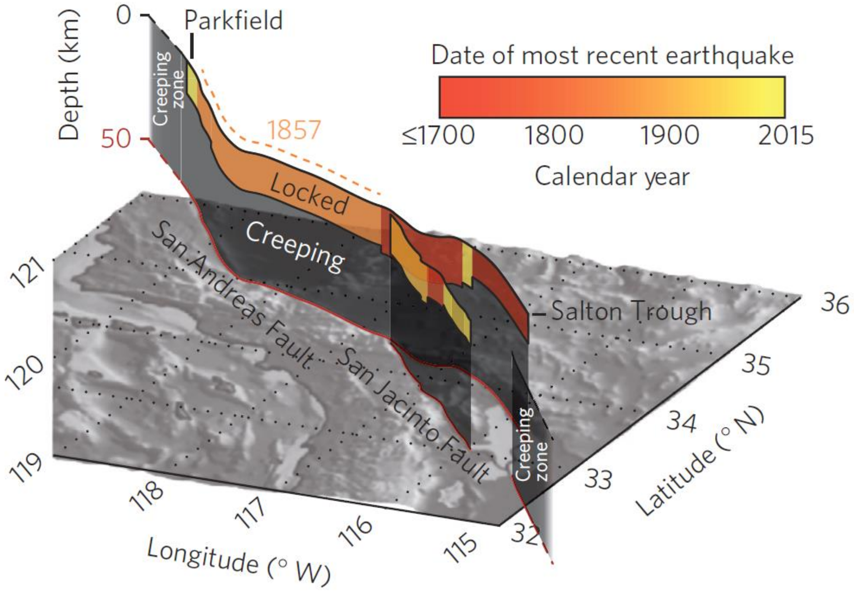

Figure 2.7. Simplified schematic of SAFS locking depth variations and historical earthquake sequence. Locked SAFS segments are represented in color to illustrate the historical earthquake sequence. Creeping and partially creeping (south of the Salton Trough) sections of the fault are shown in grey. Segments from Parkfield to the Salton Trough have been locked since at least the M7.9 1857 Fort Tejon earthquake, while segments bounding this region accommodate strain primarily through aseismic creep.

CHAPTER 3. MAGMATIC AND TECTONIC EXTENSION AT THE CHILE RIDGE: EVIDENCE FOR MANTLE CONTROLS ON RIDGE SEGMENTATION

Abstract

We use data from an extensive multibeam bathymetry survey of the Chile Ridge to study tectonomagmatic processes at the ridge axis. Specifically, we investigate how abyssal hills evolve from axial faults, how variations in magmatic extension influence morphology and faulting along the spreading axis, and how these variations correlate with ridge segmentation. The bathymetry data are used to estimate the fraction of plate separation accommodated by normal faulting, and the remaining fraction of extension, *M*, is attributed primarily to magmatic accretion. Results show that *M* ranges from 0.85 to 0.96, systematically increasing from first- and second-order ridge segment offsets towards segment centers as the depth of ridge axis shoals relative to the flanking highs of the axial valley. Fault spacing, however, does not correlate with ridge geometry, morphology, or *M* along the Chile Ridge, which suggests the observed increase in tectonic strain toward segment ends is achieved through increased slip on approximately equally spaced faults. Variations in *M* along the segments follow variations in petrologic indicators of mantle melt fraction, both showing a preferred length scale of 50+/-20 km that persists even along much longer ridge segments. In comparison, mean *M* and axial relief fail to show significant correlations with distance offsetting the segments. These two findings suggest a form of magmatic segmentation that is partially decoupled from the geometry of the plate boundary. We hypothesize this magmatic segmentation arises from cells of buoyantly upwelling mantle that influence tectonic segmentation from the mantle, up**.**

As published in: Howell, S. M., G. Ito, M. D. Behn, F. Martinez, J.-A. Olive, and J. Escartín (2016), Magmatic and tectonic extension at the Chile Ridge: Evidence for mantle controls on ridge segmentation, *Geochemistry, Geophysics, Geosystems*, 17(6), 2354-2373.

3.1. Introduction

The origin of abyssal hills and the morphology of mid-ocean ridges has long been a subject of interest [e.g., *Macdonald*, 1982; 1986], and many workers have contributed to an evolving understanding of the critical underlying processes. The earliest, first-order observation was that fault-generated abyssal hills and ridge morphology differ drastically with spreading rate. Slow spreading ridges are characterized by kilometers-wide axial valleys flanked by shallow topography and ~ 10^3 m-tall abyssal hills comprised of one or more normal faults, whereas fast spreading ridges exhibit relatively smooth, topographically high axial ridges and ~ 10^2 m-tall fault topography [e.g., *Searle and Laughton*, 1981; *Macdonald*, 1982; *Goff et al.*, 1997; *Small*, 1998].

To understand these differences, many studies have investigated the role of dynamic lithospheric stresses [e.g., *Tapponnier and Francheteau*, 1978; *Lin and Parmentier*, 1989; *Chen and Morgan*, 1990b; a]. Early modeling efforts by *Chen and Morgan* [1990b] showed that axial valleys are supported by dynamic stresses, and the magnitude of axial valley relief that the stresses can support increases with axial lithospheric thickness. Their models predicted slow spreading ridges to have thick lithosphere, and thus deep axial valleys, and fast spreading ridges to have thin lithosphere and minimal dynamic stresses that yield a nearly isostatically supported axial topographic high. Closely following this work, *Chen and Morgan* [1990a] and *Phipps Morgan and Chen* [1993a; 1993b] were seminal in quantifying the links between lithosphere thickness and magmatism. These studies showed that the low magma flux at slow spreading ridges delivers a reduced heat flux to the ridge axis, which—combined with efficient hydrothermal cooling—leads to a thicker axial lithosphere. Conversely, the relatively high magma heat flux delivered to fast spreading ridges was predicted to lead to thin lithosphere. These heat balance arguments further reinforced the concept that lithospheric thickness and stresses control the differing styles of faulting and axial morphology.

Within this context, numerous studies have investigated the sources of variations in faulting and morphology along mid-ocean ridge spreading segments. One motivating observation at some slow and intermediate spreading ridges is that near segment ends, axial valleys tend to be deeper and flanked by larger and more widely spaced faults than near segment centers [*Chen and Morgan*, 1990a; *Shaw*, 1992; *Shaw and Lin*, 1993]. Additionally, workers discovered geophysical evidence for thinner crust, and hence lower magma supply, near segment ends compared to segment centers [*Kuo and Forsyth*, 1988; *Lin et al.*, 1990; *Forsyth*, 1992; *Lin and Phipps Morgan*, 1992], as later shown seismically at the Mid-Atlantic Ridge [*Tolstoy et al.*, 1993; *Hooft et al.*, 2000; *Dunn et al.*, 2005]. To better understand these observations, *Shaw and Lin* [1996] included the effect of along-axis variations in melt supply and mantle flow in three-dimensional thermal models of segmented ridges. At slow spreading rates, their thermal models predicted that segment ends are characterized by thicker axial lithosphere than segment centers, and their cyclic models of faulting showed a corresponding increase in fault slip and axial valley depth toward segment ends.

An important shift in our understanding of the linkage between magma flux, faulting, and axial morphology began with early concepts of *Shaw and Lin* [1993], who suggested that the ratio of magmatic to amagmatic spreading is an important control on faulting. The kinematic arguments and fully dynamic models of *Buck et al.* [2005] demonstrated that the most direct control on the size and spacing of faults is the fraction of extension accommodated by magmatic emplacement, *M*, and not the influence of magmatism on axial thermal structure. Subsequent studies confirmed the direct response of faulting to *M* [e.g., *Behn and Ito*, 2008; *Ito and Behn*, 2008; *Tucholke et al.*, 2008], and *Ito and Behn* [2008] further demonstrated that *M* directly influences axial topography because, in a time-averaged sense, *M* controls the magnitude of the dynamic lithospheric stresses identified by *Chen and Morgan* [1990a; 1990b] (tensile stress is relieved during periods of magmatic extension and enhanced during periods of tectonic extension). Changes in *M* from relatively low to high values lead to a transition from deep axial valleys to shallow axial topographic highs, with intermediate values producing transitional axial topography similar to that observed at intermediate spreading ridges. Whereas *M* is becoming recognized as the most direct control on fault characteristics and ridge morphology, relatively few studies have quantified this fraction at mid-ocean ridges and explored how variations in *M* between and within segments correlate with variations in ridge characteristics [*Escartín et al.*, 1999; *Ito and Behn*, 2008; *Schouten et al.*, 2010; *Paulatto et al.*, 2015].

This study aims to quantify variations in faulting, axial valley relief, and ridge geometry to understand the relationships between *M*, fault characteristics and evolution, plate boundary geometry, and axial morphology at the intermediate-spreading Chile Ridge (Figure 3.1). The Chile Ridge strikes northwest from the southern coast of Chile, and has spread relatively uniformly (31 km/Myr half spreading rate) since at least 5.9 Ma [*Tebbens et al.*, 1997]. All spreading segments are orthogonal to the spreading direction, facilitating their identification. Additionally, the wide range of segment lengths and offset distances in this ridge section make it well-suited to study the effects of segmentation geometry. To address these issues, we first measure ridge segment length, segment offset distance, axial relief, and individual fault throws and dips at five first-order (bounded by transform faults) and four second-order (bounded by oblique shear zones and axial valley jogs [*Macdonald et al.*, 1991a]) ridge segments. We then estimate the fraction of plate separation taken up by prominent, lithosphere-scale normal faults (Figure 3.2), and consider the remaining, unaccounted fraction of extension, *M*, to be a proxy for magmatic accretion. Finally, we compare segment-scale variations in *M* with variations in seafloor chemistry. Our results provide evidence for the mechanisms by which small axial faults evolve into abyssal hills, elucidate how variations in magmatic extension influence fault characteristics and ridge morphology, and relate magmatic and tectonic segmentation to the style of mantle upwelling beneath this intermediate spreading ridge.

3.2. Tectonic setting

The Chile Ridge extends southeast from the junction of the Pacific, Antarctic, and Nazca plates at the Juan Fernandez microplate to the triple junction of the Antarctic, Nazca, and South American plates (Figure 3.1) [*Tebbens et al.*, 1997, and references therein]. The proximity of the

Chile Ridge to the equator of its Euler pole yields a relatively uniform half-spreading rate of ~31 km/Myr along its length since 5.9 Ma [*Tebbens et al.*, 1997]. The spreading segments range in length from < 20 km to >200 km, and are offset from each other by distances of ~ 10 km to >1100 km.

The Chile Ridge is separated into northern and southern sections by the transform-dominated Valdivia Fracture Zone, which offsets the two sections of the ridge by more than 600 km east-to-west. The northern section of the ridge consists of 10 first-order spreading segments (N1-N10); the Valdivia Fracture Zone consists of five first-order segments (V1-V5); and the southern section of the ridge consists of five surveyed first-order segments (S1-S5). Segments N9 and S5 are each broken into two second-order segments (N9N-N9S and S5N-S5S) by non-transform offsets (Figure 3.1). We analyze the longest segments in each section where data coverage and quality are highest, while avoiding segments where faulting is irregular and complex. Hence, we focus on segments N1, N5, N8, N9N, N9S, N10, V4, S5N, and S5S.

3.3. Methods

3.3.1. Measurements of fault characteristics

We used SeaBeam 2000 multibeam bathymetry data collected during research cruise PANR04MV in January-March 1998 aboard the R/V Melville [*Karsten et al.*, 1999]. To quantify fault characteristics, the data were first gridded at 100 m x 100 m. We then applied a high-pass Fourier filter that isolated wavelengths ≤ 20 km to distinguish the short-wavelength structure of individual faults from the longer-wavelength morphology of the axial valley ridge (Figure 3.3a-c). Three grids were subsequently used in our analysis: the original unfiltered bathymetry, the filtered bathymetry containing the short wavelengths, and the filtered bathymetry containing the long-wavelengths. For each grid, we examined individual transects along spreading flowlines determined from the relevant opening pole of *Tebbens et al.* [1997] (Figure 3.3d-f). Between 3 and 18 transects were defined for each segment. When possible, we selected transect locations within the well-resolved parts of the multibeam swaths (i.e., away from swath edges) to sample seafloor uniformly along each segment while capturing topography near both segment ends and segment centers. This resulted in transect spacings of 3–15 km.

To identify individual faults, we examined maps of the unfiltered bathymetry, the short-wavelength bathymetry, its gradient and curvature, and profiles of these maps taken along the individual transects (Figure 3.4). 2,157 faults were identified as continuous, linear features that terminate or branch at both ends, distinguished from volcanic features with rounded margins and no clear termini (Figure 3.4a). The continuous, high-slope scarp faces were accentuated in maps of filtered bathymetry gradient (Figure 3.4b). Faults appeared in maps of filtered bathymetry curvature (Figure 3.4c) as long, linear bands, marking the high-curvature break in slope at the top and bottom of fault scarps. Volcanic and hummocky material appeared in maps of curvature as pseudo-circular closed loops, marking the break in slope at the top and bottom of cones and hill-like fabrics.

After the faults were identified, we used the original unfiltered bathymetry to pick the shallowest parts of the fault as scarp tops and the deepest level of the basins as scarp bottoms along the transects (Figure 3.4e-g). These picks were used to estimate the original, undegraded throw of the fault. Estimates of the least-degraded, original fault dip were obtained by selecting the most continuous, high-angle face of each scarp. The mean spacing of faults along each transect was computed by dividing the distance between the westernmost and easternmost fault scarp tops by the total number of faults crossed.

To verify our measurements, we examined the frequency distribution of fault throws. Natural fault populations are predicted to display an exponential frequency distribution for faults having lengths comparable to or greater than the brittle layer thickness [*Cowie et al.*, 1993; *Carbotte and Macdonald*, 1994a], and exponential distributions in scarp heights and fault spacing have indeed been observed at the East Pacific Rise [*Bohnenstiehl and Kleinrock*, 1999; *Bohnsenstiehl and Carbotte*, 2001]. Consistent with these studies, the observed distribution of fault throws (Figure 3.5a) shows little deviation from exponential behavior, confirming that we identified a representative fault population without the picking process or limited data resolution obscuring all of the smaller faults. Methodological and natural biases lead to problems in estimating the dips of active faults, and are discussed below 3.4.1.

3.3.2. Measurements of *M*, axial relief, segment length, and offset distance

To characterize relationships between tectonomagmatic variables, axial morphology, and ridge geometry, we estimated the fraction of extension taken up as slip on normal faults, $(1 - M)$, and attributed the remaining fraction, M, primarily to extension accommodated by the accretion of new crust. A value of $M = 1$ would correspond to completely magmatic spreading with no faults, while $M = 0$ would correspond to completely amagmatic spreading accommodated entirely by fault slip. Estimating M required measurements of the cumulative horizontal displacement of the faults as a function of distance from the axis. Unfortunately, the degradation of bathymetry by erosion and mass wasting prohibited accurate measurements of the heave and dip of the original fault surface. Therefore, following *Escartín et al.* [1999], we estimated heave using the present-day throw, the observable least impacted by erosion and mass wasting, and an average dip for an active fault of 45°, which we justify below in Section 4.1. We next calculated $(1 - M)$ for each transect by measuring the cumulative heave between the westernmost and easternmost faults and dividing by the total distance between them (Figure 3.2). This method produces values of mean $(1 - M)$ nearly identical to those obtained with the approach of *Escartín et al.* [1999], who find the best-fit slope of cumulative heave varying with distance to the ridge axis. The standard deviation in $(1 - M)$ is estimated from the variation in the best-fit slope of cumulative heave versus across-axis distance within 10-km-wide windows along each transect.

To characterize axial morphology, we measured the relief of the axial valley as the difference in depth between the deepest part of the valley and the mean depth of the shallowest peaks flanking the valley along transects of the filtered bathymetry containing the long-wavelengths (Figure 3.3e). We also measured the length of each ridge segment as the distance along-axis between first- and second-order segment offsets, and the distance of each offset as the distance between first- or second-order spreading segments.

3.3.3. Quantifying correlations between measurements

We tested for relationships between observables in several ways. First, we tested for correlations between transect means of axial relief, M, fault throw, fault spacing, and the along-axis distance to the nearest segment end. A total of $n = 57$ transects were used. To examine the effect of (first- and second-order) offset distance, we tested for correlations between offset distance between adjacent segments and the means of axial relief, M, fault throw, and fault spacing within different groups of transects. Four of the groups were defined based on bins of the proximity, d, of each transect to the nearest segment end: $d \leq 10$ km ($n = 16$), $10 < d \leq 20$ km ($n = 15$), $20 < d \leq 30$ km ($n = 14$), $d > 30$ km ($n = 12$). A fifth grouping ($n = 18$) was done by separating transects within the northern and southern half of each segment. Further, we tested for correlations between segment length and the segment mean ($n = 9$ segments) of all fault parameters.

Correlations were quantified using Spearman's rank correlation coefficient. Although Pearson's product-moment correlation coefficient is more widely used in the geologic literature, it only detects linear correlations. Spearman's rank correlation is more general; it detects any monotonic relationship, linear or curved, and is less sensitive to outliers. We also computed a "*p*-value" for each correlation, which gives the probability that the computed correlation coefficient, or larger, occurs by random sampling from a population with a true correlation of zero. The *p*-value depends on the size of the sample being considered. For correlations between axial valley relief, fault characteristics, and along-axis distance, we computed $n = 57$ individual transect means. For correlations of axial relief and fault characteristics with the nearest ridge offset distance, we computed $n = 12 – 16$ means for the four transect bins of proximity d to the offset, and $n = 18$ means for the fifth transect grouping based on the north–half versus south–half division of each segment. For correlations of axial relief and fault characteristics with segment length, we computed $n = 9$ segment means. Low *p*-values indicate a small probability of the true correlation being zero. We considered *p*-values less than 0.05 to indicate a significant correlation.

We also tested for differences between the measured properties at segment inside corners (seafloor on the transform-fault side of the ridge segment) and outside corners (seafloor on the fracture zone side of the ridge segment) by dividing each segment into equal-area quadrants. East and west sides were separated at the ridge axis, and these half-segments were sectioned into northern and southern groups by the mid-point between segment ends. We tested for differences in the mean values of M, fault spacing, fault throw, and axial relief between the inside and outside corner groups using the non-parametric Mann-Whitney U-test. This test determines the probability that incomplete sampling of a single population yields different sample means, even though the true means are identical.

3.3.4. Comparisons with geochemical proxies of extent of partial melting and crystallization

To explore whether variations in the supply of magma to the ridge axis or the crustal magma plumbing system might influence the amount of extension accommodated on faults measured at the surface, we qualitatively compared estimates of *M* with geochemical indicators of the extent of partial melting from the analyses of *Milman* [2002]. We examine two geochemical proxies recorded in seafloor basalts: (1) the mean degree of melting, *F*, as inferred from $[Na_2O]_8$ and $[CaO]_8/[Al_2O_3]_8$ (estimated concentrations at 8 wt % MgO using regression), and (2) MgO content, which generally decreases with increasing extent of fractional crystallization in magma storage zones in the crust. Values of *F* and MgO content were smoothed along-axis to aid in the visual comparison between geochemical data and *M* using a 2 km running-average filter.

3.4. Results

3.4.1. Relations between measured fault dip and throw

Examining how measured scarp dip varies with throw reveals information about fault growth and rotation, and topographic degradation by erosion and mass wasting (Figure 3.5b). Measured scarp dips span a wide range of values at a given throw, and the envelope encompassing the range of scarp dips narrows with increasing fault throw. One boundary of this envelope occurs at the smallest throws, where the maximum observed dip increases sharply from < 5° up to ~ 50° as throw increases from 0 to ~ 200 m. This boundary is readily explained by data resolution limits: the maximum observable dip is given by the arctangent of the throw divided by the horizontal resolution of the multibeam data, which is ~ 100 m. The envelope boundary of maximum fault dips for faults with throws > 200 m can be explained by rotation of the active fault with increasing slip, consistent with predictions of numerical models and analytic scaling laws for faulting of an elasto-plastic lithosphere overlying a low-viscosity asthenosphere [*Olive and Behn*, 2014]. The boundary shown is from such a model with an effective elastic plate thickness of 2 km. Indeed, the observed variation in maximum fault dip as a function of throw decreases from nearly 50° at throws of ~ 300 m to ~ 35° at throws > 1 km, but fails to reach the higher predicted dips, presumably due to degradation of the fault scarps. Finally, we attribute the lower envelope boundary to be the maximum extent that mass wasting and erosion can reduce the apparent fault dip. The decreasing influence of erosion and mass wasting on fault dip with increasing topographic wavelength over a given time span is consistent with diffusive erosion models [e.g., *Webb and Jordan*, 2001].

In summary, fault rotation and fault scarp degradation introduce significant complexity into the estimation of original fault dip, which is in turn needed to quantify fault heave and *M* as described in Section 3.3.1. In our preliminary treatments, we consider mean dips of 30°, 45°, 60°, and dips that varied with slip as predicted by the elasto-plastic faulting models of *Olive and Behn* [2014]. All cases produced similar trends despite subtle differences in mean values of *M* (*M* scales with the tangent of fault dip, so an assumed dip of 30° reduces mean *M* by 11%, while a dip of 60° increases *M* by 4%). Additionally, the case where dip decreased with increasing throw slightly strengthened the significance of the reported correlations. Conservatively, we therefore report only the results for a constant mean dip of 45° because it is comparable to the maximum measured dips.

3.4.2. Observations of individual segments

Segment N1

The northernmost segment of the Chile Ridge, N1 (Figure 3.6a), is a 70-km-long first-order spreading segment bounded in the north by a ~ 1,000-km-long transform fault zone, and in the south by en-echelon transform faults and intra-transform spreading centers (ISCs) that offset N1 east of segment N5 by ~ 250 km. Segment N1 exhibits an "hourglass" morphology, defined by depth contours running along the spreading axis that widen near the segment ends as the axial valley deepens and narrow towards the segment center as the valley shoals. The axial valley is asymmetric across the axis near segment ends, deepening more towards the inside corner side of the ridge. Seafloor fabric on both sides of the axial valley is dominated by large, ridge-parallel abyssal hills composed of normal fault complexes that run nearly half the segment length. As shown in Figure 3, these abyssal hills are superimposed on the long-wavelength axial valley topography and tend not to strike parallel to the curving axial valley flanks, but rather initiate at a consistent distance from the axis of approximate east-west symmetry.

Variations in a number of other key observables are seen along the ridge segment. From the segment ends toward the segment center, the relief of the axial valley decreases from > 1 km to ~ 0.75 km. The reduction in relief is ~ 0.1 km more pronounced from the southern segment boundary in response to shallow flank bathymetry on the west side of the ridge axis. As relief decreases from the segment ends to the segment center, fault spacing increases from ~ 1.5 km to ~ 2 km and *M* increases from 0.88 to 0.92. This trend in *M* is seen at both outside and inside corners, but *M* on inside corners is overall greater by approximately one standard deviation.

Segment N5

Segment N5 is a 95 km-long first-order spreading segment that is offset ~ 250 km east of segment N1 (Figure 3.6b). It is bounded in the south by pseudofaults associated with the dueling propagation between the southern end of N5 and northern end of N6, which is offset ~ 20 km east. Segment N5 exhibits an asymmetric hourglass morphology. The narrowest "waist" of the hourglass and shallowest part of the ridge axis occur near a short chain of volcanic cones, ~ 25 km south of the northern segment boundary and ~ 70 km north of the southern boundary. To the south, the relief of the axial valley (1 km) is substantially greater than in the north (~ 0.3 km). From the segment ends to the shallowest part of the ridge, fault spacing increases from ~ 1.5 km to > 4 km, and *M* increases from ~ 0.92 to 0.96. This trend in *M* is similar between the outside and inside corners, except near the seamount chain, where *M* = 0.97 on the inside corner (seamount side) and *M* = 0.93 on the opposite side.

One obvious feature influencing the morphology of segment N5 is the competing spreading segment N6. Segment lengthening and shortening is recorded in the seafloor fabric west of the southern terminus of segment N5, resulting in bathymetric ridges that tend to strike southward and curve towards segment N6. We therefore picked transects away from this complex fabric, and chose not to analyze segment N6.

Segment N8

Segment N8 is a 65-km-long first-order spreading segment (Figure 3.6c), bounded in the north by a transform fault extending from the ISC N7 and in the south by a transform fault that offsets segment N9 80 km to the east. Segment N8 exhibits a more subdued hourglass morphology than N1 or N5, primarily because the segment center is deeper. Like other segments on the Chile Ridge, the axial relief shows a local minimum (~ 0.6 km) at the shallowest part of the segment. However, unlike the other segments, the relief lessens very close to the segment ends where the axial valley flanks deepen toward the transform offset more rapidly than the axial valley. Fault spacing displays no long-wavelength change along the segment, whereas *M* increases towards the shallowest part of the segment with an overall variation from 0.85–0.95. Inside corner values of *M* tend to be lower than outside corners values near the segment ends, but show no difference near the segment center.

Segment N9

Segment N9, the longest segment in the study area, is a 140-km-long first-order spreading segment that is broken into two second-order segments, N9N and N9S, by a non-transform offset (NTO) (Figure 3.6d). N9 is bounded in the north by a transform that offsets it 80 km east of segment N8 and in the south by a transform that offsets it 25 km east of segment N10.

Second-order segment N9N is 110-km-long and bounded in the south by a NTO that offsets it 8 km east of N9S. Unlike other segments studied, segment N9N exhibits a morphology resembling two “stacked” hourglasses. A deep, wide axial valley at the northern transform boundary narrows and shoals for ~ 30 km to the south, where a volcano chain similar to that seen at N5 strikes west from the axis. The valley then deepens and widens for another ~ 20 km southward. This pattern of narrowing and widening then repeats once more before reaching the NTO. Axial relief varies accordingly: it is locally small near the two narrow hourglass waists (minimum 0.5 km in the north and 0.25 km in the south) and locally large between the waists and near the segment ends (0.7 km in the north, 0.8 km in the center, and 0.55 km in the south). *M* varies in a correlated, but opposite manner: it is locally high near the hourglass waists (minima in axial relief) and smaller between the waists and near the segment ends. Thus, N9N exhibits a wavelength of variation in morphology that is distinct from that of tectonic segmentation.

Second-order segment N9S is 30-km-long and exhibits a semi-hourglass morphology evident in the widening of depth contours near the southern segment boundary. Valley flanks on the inside corners of both the NTO in the north and the transform in the south are anomalously shallow. There is a slight southward decrease in axial relief from 1.3 to 0.9 km. Fault spacing tends to decrease from ~ 1.5 km at the segment ends to ~ 1 km at the segment center. The variations in mean *M* along the segment are small compared to the standard deviation.

Segment N10

Segment N10 is a 95-km-long first-order spreading segment (Fig 6e), bounded in the north by a transform fault that offsets it ~ 25 km west of segment N9 and in the south by the Valdivia Fracture Zone: a 600-km-wide east-west trending regime of en echelon ISCs offset by long transform faults (Fig 1). Segment N10 exhibits hourglass morphology, although the strike of the ridge axis varies, making it less linear than many of the other segments. Similar to the trends observed along other segments, there is a decrease in relief from > 1.0 to 0.2 km away from the segment ends towards the segment center. Fault spacing shows little variation, while *M* is highest (0.95) near the segment center. From the southern segment boundary, *M* increases toward the segment center by an amount that is comparable to the standard deviation. Near both segment ends, *M* is lower on the inside corners than on the outside corners.

Segment V4

Segment V4 is a 20-km-long first-order intra-transform spreading center in the Valdivia Fracture Zone, bounded in the north and south by long transform fault segments that offset it from neighboring ISCs (Figure 3.5f). The segment is tectonically dominated by large-slip faults, with an axial valley that is split by a ridge in the north and deepens significantly in the south. The transform fault fabric and short segment length limited fault measurements to only two transects.

Axial relief is greatest in the south where the axial valley is deepest, increasing from 1.2 to 1.5 km from north to south, the highest relief of any measured transect. This corresponds to a decrease in fault spacing from 2.0 to 1.4 km. Like the other segments studied, *M* decreases as relief increases, here from 0.93 to 0.92, though this variability is well within the standard deviation on *M*. Estimates of *M* for both inside and outside corners are ~ 0.93 in the north; inside corner values decrease to 0.9 in the south while outside corner values remain at 0.93.

Segment S5

Segment S5, the southernmost surveyed and studied segment, is a 115-km-long first-order spreading segment that is broken into two second-order segments, S5N and S5S, by a slight eastward jog in the axial valley (Fig 6g). S5 is bounded in the north by a Valdivia Fracture Zone transform fault, and in the south by a transform fault that offsets the next segment ~ 60 km to the east.

Second-order segment S5N is 70-km-long and exhibits an hourglass morphology. The northern inside corner is anomalously shallow and the northern outside corner is anomalously deep. Like many of the other segments, axial relief tends to decreases from the segment offsets toward the segment center (here from > 1 km to 0.5 km), while M increases from the offsets toward the segment center (from 0.92 to 0.96). M at the inside corner is 0.05 greater than at outside corner in the north, and approximately equal in the south. There is no apparent systematic variation in fault spacing.

Second-order segment S5S is ~ 45 km long and exhibits a subdued hourglass morphology. The inside corner of the southern section is shallower than the opposite outside corner. Axial relief decreases from > 1 km near the segment offsets to ~0.8 km near the segment center. From north to south, fault spacing decreases from 1.6 to 1.1 km, and M decreases from 0.93 to 0.92, although this variation in mean M is small compared to the standard deviation. Compared to the outside corners, M at the inside corners is higher near the segment center and lower near the segment ends.

3.4.3. Intrasegment correlations of transect means

Using the observations made at these nine Chile Ridge segments, we now examine correlations between faulting, morphological characteristics, and M to illuminate the relationships governing segment-scale and along-axis variations (Figure 3.7, rows a-b). We find that axial relief correlates significantly with M and fault throw (from which estimates of M are partially derived), demonstrating a close relationship between the longer-wavelength axial morphology and magmatic extension along these segments. However, while M and axial relief correlate strongly, neither variable shows a significant correlation with fault spacing. Thus along-axis changes in M are accommodated by changes in slip along faults without a strong change in fault spacing.

To explore the influence of segment boundaries, we compute correlations between the distance from the nearest segment end along the ridge axis, axial relief, M, and fault characteristics (Figure 3.7, row c). We find that as distance from the segment end increases, axial relief and fault throw tend to decrease, while M tends to increase. This finding is consistent with global trends of shallower axial valleys being associated with greater values of M [*Ito and Behn*; 2008] and mantle magma supply to the ridge axis [*Dunn et al.*, 2005; *Lin and Phipps Morgan*, 1992].

3.4.4. Intrasegment evidence for magmatic segmentation

Magmatic segmentation refers to the spatial separation of magma delivery and plumbing systems at a ridge axis [*Carbotte et al.*, 2015]. In this paper, we use along-axis variations in *M*, axial valley relief, and petrologic indicators as proxies for magmatic segmentation.

First, we compare along-axis variations in *M* to the MgO content of seafloor basalts *Milman* [2002] (Figure 3.8a). Variations in *M* and MgO appear to be positively correlated at some segments, negatively correlated in others, and in some locations are out of phase or entirely lack any correlated variation. Thus there appears to be no systematic relation between the amount of magmatic extension and the processes of magma storage and cooling (i.e., crystallization) in the crust reflected by the MgO content.

We next compare along-axis variations in *M* to estimates of the extent of partial melting of the mantle, *F*, *Milman* [2002] (Figure 3.8b). In all but one segment (N10), *F* tends to be locally low where *M* is locally low (usually near segment ends) and *F* tends to be locally high where *M* is locally high (usually near segment centers). Along segment N9N, two distinct local maxima in *F* and *M* within the second-order segment are separated by a local minimum in both quantities. These findings suggest that local highs in melt supply, inferred from the geochemistry data, contribute to local highs in magmatic extension (and lows in tectonic extension), and that variations in the two demarcate a scale of magmatic segmentation of approximately 50 ± 20 km.

A closer look at the bathymetry in map view offers further insight (Figure 3.9). Segments shorter than or comparable to the 50 ± 20 km wavelength of magmatic segmentation (e.g., N1) exhibit relatively straight axial valleys with north-south symmetry and single maxima in *M* and *F*. Segments with lengths greater than the observed scale of magmatic segmentation display subtle jogs in the axial valley (e.g., N10) or multiple maxima in *M* and *F* (e.g., N9N). Segments that are much longer than 50 ± 20 km exhibit prominent axial jogs and second-order segment offsets that correspond to distinct magmatic segments seen in *M* and *F* (e.g., N5/N6, N9, and S5). Thus we infer that the length scale of magmatic segmentation of 50 ± 20 km is at least partially decoupled from the length scale of tectonic segmentation.

3.4.5. Comparisons of inside and outside corners

We examine the effect of transforms on the cross-axis symmetry of the seafloor structure by computing correlations for inside and outside corners separately (Table 3.1a). Parameter means for inside and outside corner quadrants both show the same significant and insignificant correlations as the full transect means. Comparing the correlation coefficients between the two sides of the ridge axis shows that the across-axis differences in all but two of the coefficients are statistically insignificant (Table 3.1a). Furthermore, the mean values of all the parameters do not differ significantly between the two sides of the axis (Table 3.1b). The two significant differences found are in the correlations of *M* and throw with distance to an offset: the correlation with *M* at inside corners is 1.6 times greater than that for the outside corners. Thus, mean *M* and fault throw do not differ significantly between the two sides of the ridge axis, but change more appreciably toward the inside corner than toward the outside corner.

3.4.6. Intersegment variability and sensitivity to plate boundary geometry

To investigate differences between segments, we examine how measured variables change with offset distance and segment length. Comparing transect means of the northern and southern segment-halves (grouping 5) with the distance of the neighboring offset does not yield any significant correlations (Figure 3.7, row d). Further, means of transects grouped according to, *d*, the transect proximity to the segment end (groupings 1-4) do not show any significant correlations with offset distance (Figure 3.10). Correlations between ridge segment length and segment mean properties show that longer segments tend to exhibit less overall axial relief (Figure 3.7, row e), but are not significant for all the other properties. Together these results suggest that the impact of the plate boundary geometry on faulting, magmatism, and morphology is negligible at the Chile Ridge.

3.5. Discussion and Inferences

3.5.1. Geologic mechanism of fault formation and evolution

Close inspection of the seafloor fabric on and adjacent to the Chile Ridge provides insight into the evolution of faults and the origin of abyssal hills. Between the axially continuous, large abyssal hill fault scarp complexes, the seafloor is typically broken by numerous short strike, small faults (e.g., see Figure 3.11a,b). This pattern is ubiquitous, and can be explained by a new model of cyclic fault growth that is consistent with current concepts of fault initiation and interaction in three dimensions [e.g., *Carbotte and Macdonald*, 1994; *Cowie et al.*, 1993] and the mechanical limits on the width of the active fault zone near the ridge axis [*Behn and Ito*, 2008; *Buck et al.*, 2005; *Chen and Morgan*, 1990a].

At the onset of one of these faulting cycles, extension is accommodated within a few kilometers of the ridge axis through diffuse tectonic deformation on numerous small faults (Figure 3.11b,c, time t_0). With continued extension, some of these faults link, accommodating a disproportionate amount of the tectonic strain, and eventually grow into tall and long abyssal-hill-scale fault complexes (Figure 3.11b,c times t_1-t_3). The large faults then raft the abandoned small faults away from the ridge axis on the back of the footwall. This inferred evolution is consistent with observations and numerical models of normal faults [e.g., *Cowie and Roberts*, 2001; *Dawers and Anders*, 1995; *Manighetti et al.*, 2015], in which continued slip and fault propagation cause many small faults to link along-strike and form much longer and taller faults.

Eventually the large fault moves far enough off axis and has accumulated enough slip that a greater force is required to keep it slipping than to initiate a new fault closer to the ridge axis [*Behn* *and Ito*, 2008; *Buck et al.*, 2005]. When this occurs, diffuse tectonic extension on small faults occurs near the ridge axis as before (Figure 3.11c, time t_4). The cycle repeats, with the next large fault typically forming on the opposite side of the ridge axis (Figure 3.11c t_5-t_6). The result is periodically spaced, axis-parallel fault complexes superimposed on the longer wavelength topography associated with the axial valley (e.g., Fig 3c). It is unclear whether this cycle occurs in discrete stages, as described, or whether multiple stages can be contemporary. We estimate that a new abyssal hill fault-complex generally forms at the Chile Ridge once every 220–340 kyr based on the spreading rate and mean spacing of the large-scale abyssal hill structures.

3.5.2. Changes in magmatic extension with uniform fault spacing

The finding that fault spacing does not change systematically with any variables along the Chile Ridge indicates that the observed changes in *M* are accommodated by changes in mean fault throw, and not changes in fault frequency (i.e., spacing). A small seamount chain at N9N illustrates this behavior (Figure 3.1c and Figure 3.6d-second transect from the top). Here, throw decreases along individual faults as they approach the seamounts where *M* is anticipated to be locally very high. The decrease in fault throw is seen as a deepening of the tops of the faults toward the seamounts, indicating a reduction in total fault slip. This depression of fault scarp tops is not likely due to flexure of the lithosphere, given the small wavelength of the volcanoes relative to the elastic plate thickness [e.g., *Olive et al.*, 2015]. This observation is distinguishable from the alternative situation where magma infills the fault basins, whereby the fault bottoms would shoal and fault tops would remain at constant depth, and the topographic expression of throw would be reduced, but the true throw would not decrease.

We interpret these observations to indicate that the formation of the seamounts occurred near the axial zone of diffuse tectonic deformation and led to a locally high proportion of magmatic extension. In fact, *M* may have been close to 1 where the largest seamounts formed, as evident by the complete termination of the faults on either side of the seamounts (Figure 3.1c). Near the lower topographic bulge just east of the shorter seamount, the fault top deepens, but the fault continues through the bulge, suggesting *M* is locally high, but < 1. This is an example of where a local high in magma flux correlates with a reduction in the amount of slip on the adjacent faults without a clear change in fault spacing.

To explain the lack of a change in fault spacing with proximity to segment offsets and *M*, we refer back to predictions of mechanical models of *Behn and Ito* [2008]. First, they show that the sensitivity of fault spacing on *M* rapidly decreases for high values of *M*. Given the relatively small magnitude of along-axis variations in *M*, it is possible that a dependency of fault spacing on *M* is present, albeit masked by natural variations in the fault population. Additional support for this possibility is that while *M* and fault spacing are not correlated at the 5% confidence level, they are correlated at the 10% confidence level.

Additionally, *Behn and Ito* [2008] showed that decreasing both *M* and the lithospheric thickness tends to increase fault spacing. We hypothesize that the observed decrease in *M* towards segment ends tends to increase fault spacing, while reduced magma delivery near segment ends results in cooler, thicker axial lithosphere and slower off-axis thickening rate, which tends to reduce fault spacing [*Behn and Ito*, 2008]. Thus, the relatively high and uniform values of *M* imply that only small variations in lithospheric thickness are required for the two counteracting effects to obscure any systematic variation in fault spacing. Finally, along-axis stress coupling, which was not addressed by *Behn and Ito* [2008], may be important, as the axis-parallel abyssal hill scale faults can extend over a large fraction (25–60%) of the total segment length. The tendency of faults to preserve their along-axis integrity would tend to minimize changes in the spacing between faults with the relatively subtle changes in *M* along the segment.

Another finding for the Chile Ridge is that mean values of *M* and fault spacing do not differ significantly between inside corners and outside corners; it is only the change in *M* from segment centers toward inside corner offsets that appears to be greater than the change in *M* toward outside corner offsets. No such difference is apparent with fault spacing. These results contrast with those of *Escartin et al.* [1999], who showed little or no change in *M* along-axis, but a significant increase in mean fault spacing and fault throw with proximity to the inside corner of a non-transform offset at Mid-Atlantic Ridge. This contrast indicates a difference in the mechanics of inside corners at that particular offset than along the Chile Ridge, and that the variations we observe in relatively high values of *M* may be too small to have a measurable effect on the segment corners.

3.5.3. Evidence for mantle controls on ridge segmentation

At the Chile Ridge, we find that all measured parameters, including *M* and segment morphology, vary independently of segment offset distance, and that only axial relief depends significantly on segment length. In addition, variations in axial valley relief, *M*, *F*, and the overall ridge structure indicate magmatic segmentation at a preferred length scale of 50 ± 20 km that can occur in the absence of tectonic segmentation. These findings are two separate lines of evidence against plate boundary geometry, characterized by segment length and offset distances, exerting a primary control on along-axis variations in magmatism, faulting, and morphology at the Chile Ridge.

In one end-member case for mantle flow beneath a spreading axis, mantle upwelling is driven entirely as a passive response to the divergence of the overlying plates [e.g., *Parmentier and Phipps Morgan*, 1990]. In this “top-down” scenario, along-axis variations in mantle flow and magma flux are most tightly linked to the geometry of the plate boundary. For example, sections of ridge near the long transforms would have lower magma flux and lower *M* than those near short transforms, and magma flux and *M* would always be high in segment centers and increase with segment length. The predictions of this end-member form of mantle flow and melting are not consistent with our findings of the Chile Ridge.

Another end-member case for mantle flow involves active mantle upwelling driven by buoyancy contrasts resulting from perturbations in mantle melting or temperature, thus causing surface variations from the "bottom-up" [e.g., *Jha et al.*, 1994; *Lin and Phipps Morgan*, 1992; *Parmentier and Phipps Morgan*, 1990; *Sparks et al.*, 1993]. Our findings of a 50 ± 20 km segmentation in *M*, axial relief and *F*, and no correlation between the first two parameters with offset distance are better explained by the presence of active upwelling cells beneath the Chile Ridge. We propose that rapid upwelling in the centers of these cells tend to occur beneath segment centers, and the more slowly upwelling cell edges tend to coincide with segment ends. However, when spreading segments are much longer than the preferred wavelengths (50 ± 20 km) of the cells, the surface is imprinted with periodic along-axis variations, such as the stacked hourglass morphology of segment N9N. These variations in magmatism, faulting, and morphology, and the location of upwelling cells may even promote the later formation of segment offsets. For example, segment N9S, a third hourglass along segment N9, is offset from N9N where *M* is locally minimal, away from the proposed upwelling cell center. Thus, we argue for the bottom-up process whereby variations in magma supply from these upwelling cells control second-order segmentation [*Schouten et al.*, 1985] as opposed to the top-down process whereby segmentation imposes controls on magma supply [*Lonsdale*, 1989; *VanderBeek et al.*, 2014].

Evidence for a bottom-up control along the southern Chile Ridge and along the Southwest Indian Ridge comes from observations of intersegment distinctions in lava isotope compositions, which suggest that tectonic segments are segregated by differing mantle source compositions [*Meyzen et al.*, 2005; *Sturm et al.*, 1999]. Additionally, *Wilson et al.* [2013] propose that reduced melt production due to depleted mantle melting at slow-spreading ridges can cause a transition from magmatic to amagmatic spreading at oceanic core complexes. These relationships between variations in melt supply, magmatic accretion, and ridge morphology hint at an underlying geochemical control on faulting, morphology, and ridge geometry that ultimately originates from within the mantle.

3.6. Conclusions

In this study, we characterized relationships between magmatic accretion inferred from tectonic strain (*M*), fault characteristics, ridge geometry, and axial morphology at the intermediate spreading Chile Ridge. At the intrasegment scale, we find that fault throw generally decreases towards the segment center, but that fault spacing does not change systematically along-axis. Thus, an observed increase in *M* from segment ends to segment centers results in shorter throw, similarly spaced faults. This finding contrasts with the Mid-Atlantic Ridge, where fault spacing tends to be widest near segment ends and decreases toward segment centers. Additionally, while the along-axis increase in *M* towards segment centers may be slightly more pronounced at the inside corners of offsets, we find no significant across-axis variation in mean *M* or fault spacing between inside and outside corners.

Correlated along-axis variations in *M*, axial valley relief, and petrologic indicators of the fraction of partial melting of the mantle indicate a length scale of magmatic segmentation of ~ 50 ± 20 km that persists independently of tectonic segmentation along the longest ridge segments. Further, we observe no systematic correlations between *M* and axial relief with adjacent transform and non-transform offset distances, and find that segment length correlates only with axial relief. Thus, rather than responding passively to plate separation, the mantle beneath the Chile Ridge likely exhibits magmatic segmentation due to deep-sourced variations in melt supply that result from segmented active mantle upwelling that is partly decoupled from the geometry of the plates.

We propose that abyssal hills near the Chile Ridge are created by an initial stage of diffuse tectonic extension near the ridge axis, followed by the linking of small faults to form large fault complexes that form the bounding structures of abyssal hills. These abyssal-hill-scale fault complexes raft packets of small, failed axial faults on their footwall, and are superimposed on the long-wavelength topography associated with the axial valley.

The systematic along-axis variations in *M* and axial morphology without corresponding changes in fault spacing demonstrate the inherently 3-D nature of mid-ocean ridge processes. These findings illuminate the need for detailed studies of bathymetry and ridge structure across all spreading rates, as well as 3-D numerical models of magmatic accretion and faulting, to advance our understanding of the relative importance of along-axis variations in *M*, stress coupling, and crustal temperatures on the structure of the seafloor created at mid-ocean ridges.

3.7. Tables and figures

Table 3.1. Correlations of measured and estimated parameters. (a) Spearman's rank correlation coefficient, *p*-value, and sample size for each pair of measured parameters, computed separately for the whole ridge, and for inside and outside corners. The *p*-value is the probability that random chance and incomplete sampling of the data lead to correlation coefficients as large as or larger than those measured when sampling from a total population having a true correlation coefficient of zero. A correlation comparison significance test utiling the Fisher *r*-to-*z* transformation was used to produce a second *p*-value; this value is the probability that the true correlation coefficients associated with inside and outside corners are equal, but appear different due to incomplete sampling and random chance. (b) Comparison of mean values for *M*, fault spacing, fault throw, and axial relief at outside and inside corners. The non-parametric Mann-Whitney U-test was used to determine the probability that the differing measured means arise even though the true means associated with the outside and inside corners are identical. In all cases, we consider a *p*-value less than 0.05 to be significant. Significantly correlated pairs are highlighted.

(a)

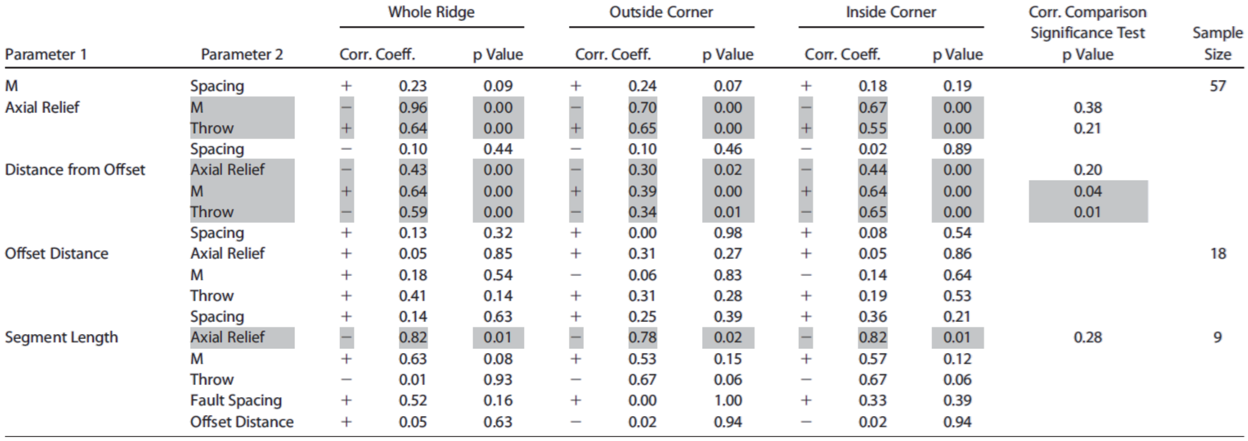

		Whole Ridge			Outside Corner			Inside Corner				
Parameter 1	Parameter 2		Corr. Coeff.	p Value		Corr. Coeff.	p Value		Corr. Coeff.	p Value	Corr. Comparison Significance Test p Value	Sample Size
M	Spacing	+	0.23	0.09	+	0.24	0.07	+	0.18	0.19		57
Axial Relief	M	−	0.96	0.00	−	0.70	0.00	−	0.67	0.00	0.38	
	Throw	+	0.64	0.00	+	0.65	0.00	+	0.55	0.00	0.21	
	Spacing	−	0.10	0.44	−	0.10	0.46	−	0.02	0.89		
Distance from Offset	Axial Relief	−	0.43	0.00	−	0.30	0.02	−	0.44	0.00	0.20	
	M	+	0.64	0.00	+	0.39	0.00	+	0.64	0.00	0.04	
	Throw	−	0.59	0.00	−	0.34	0.01	−	0.65	0.00	0.01	
	Spacing	+	0.13	0.32	+	0.00	0.98	+	0.08	0.54		
Offset Distance	Axial Relief	+	0.05	0.85	+	0.31	0.27	+	0.05	0.86		18
	M	+	0.18	0.54	−	0.06	0.83	−	0.14	0.64		
	Throw	+	0.41	0.14	+	0.31	0.28	+	0.19	0.53		
	Spacing	+	0.14	0.63	+	0.25	0.39	+	0.36	0.21		
Segment Length	Axial Relief	−	0.82	0.01	−	0.78	0.02	−	0.82	0.01	0.28	9
	M	+	0.63	0.08	+	0.53	0.15	+	0.57	0.12		
	Throw	−	0.01	0.93	−	0.67	0.06	−	0.67	0.06		
	Fault Spacing	+	0.52	0.16	+	0.00	1.00	+	0.33	0.39		
	Offset Distance	+	0.05	0.63	−	0.02	0.94	−	0.02	0.94		

(b)

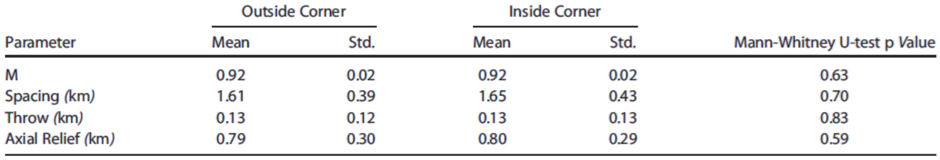

	Outside Corner		Inside Corner		
Parameter	Mean	Std.	Mean	Std.	Mann-Whitney U-test p *Value*
M	0.92	0.02	0.92	0.02	0.63
Spacing *(km)*	1.61	0.39	1.65	0.43	0.70
Throw *(km)*	0.13	0.12	0.13	0.13	0.83
Axial Relief *(km)*	0.79	0.30	0.80	0.29	0.59

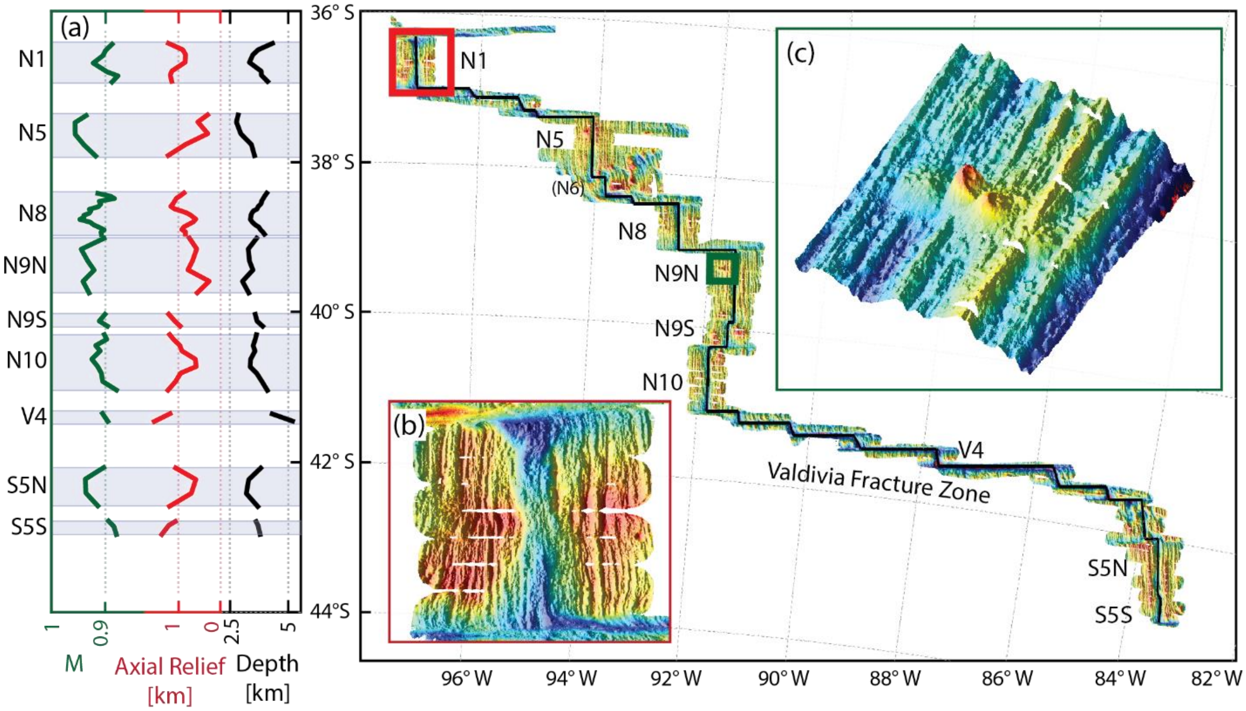

Figure 3.1. Multibeam bathymetry and along-axis variability of the Chile Ridge. (a) Along-axis variations in the ratio of the fraction of total extension accommodated magmatically, M (green), axial valley relief, the depth of the axial valley floor below the flanking topographic highs after removing the short-wavelength topography due to faulting (red), and axial valley floor depth (black). First-order spreading segments are labeled and highlighted with grey boxes. The red square around segment N1 marks the area showing (b) an example of a classic hourglass morphology, characterized by depth contours (e.g., the light blue color) that are far apart near the deep segment ends and become closer together near the shallow segment center. The green square around the northwest quadrant of segment N9N marks (c) the area of a short volcano chain interrupting the continuity of axis-parallel faults.

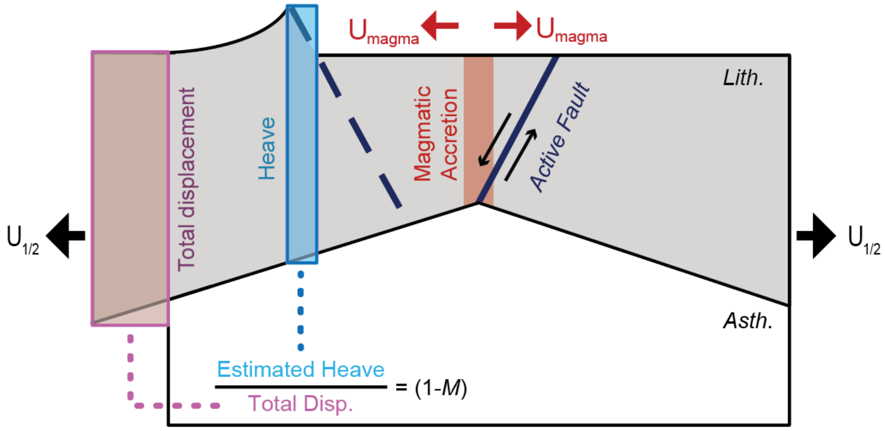

Figure 3.2. Illustration of magmatic and tectonic extension. Oceanic lithosphere (grey) is spreading at a half spreading rate $U_{1/2}$. Magmatism (light red) at the ridge axis accommodates a fraction $M = U_{magma}/U_{1/2}$ of the total spreading. Faults form near the ridge axis and then migrate away from the axis into thicker, stronger lithosphere. They eventually become inactive (dashed line) once the energy required to keep them slipping exceeds that needed to create a new fault (bold line) closer to the ridge axis. The accumulated heave (blue box) on the faults, accommodates a fraction (1-*M*) of the total spreading (purple box).

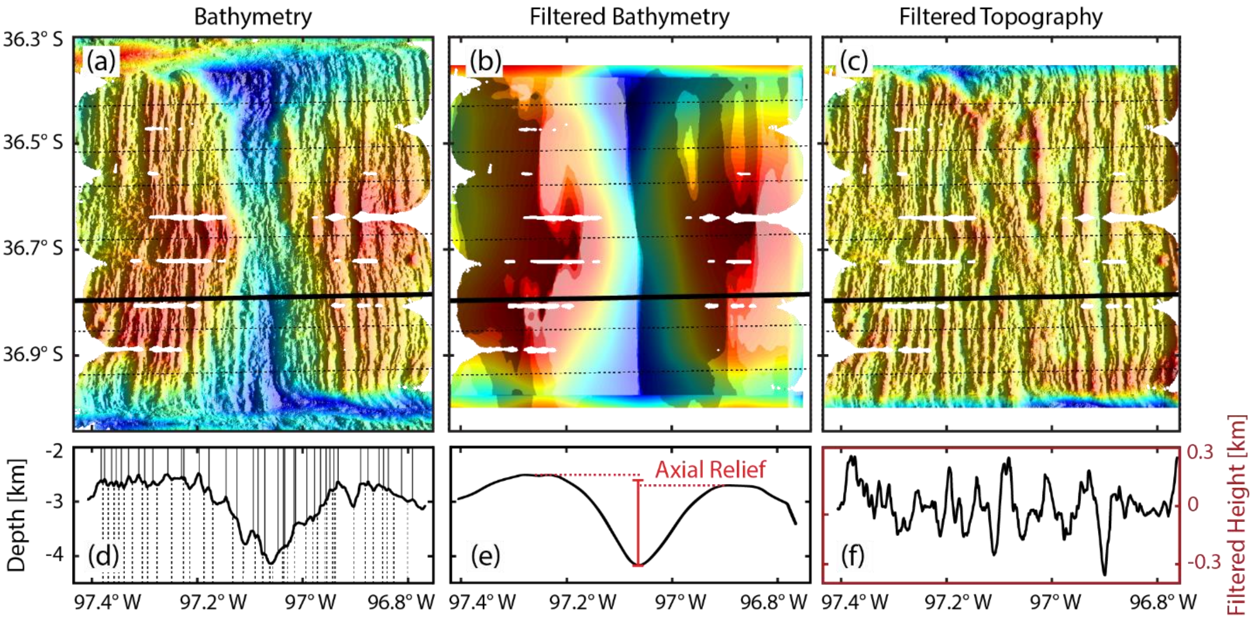

Figure 3.3. Shaded relief maps of segment N1 (a) multibeam bathymetry, (b) low-pass filtered bathymetry with wave numbers > (2□/20) km^{-1} (or wavelengths < 20 km) removed, and (c) the high-pass filtered map found by subtracting the low-pass bathymetry from the raw bathymetry. Lines show transects along which faults were identified and axial relief was measured. Profiles of (d) depth, (e) low-pass filtered depth, and (f) high-pass filtered topography along the bold transect in (a-c); the black depth scale applies to panels (d) and (e), while the red filtered height scale applies to panel (f). The high-pass filtered bathymetry was used to pick fault tops and bottoms, marked with thin solid and dashed lines, respectively, on the unfiltered bathymetric profile (d). The red bar in (e) shows axial relief, derived from the low-pass filtered bathymetry (see text).

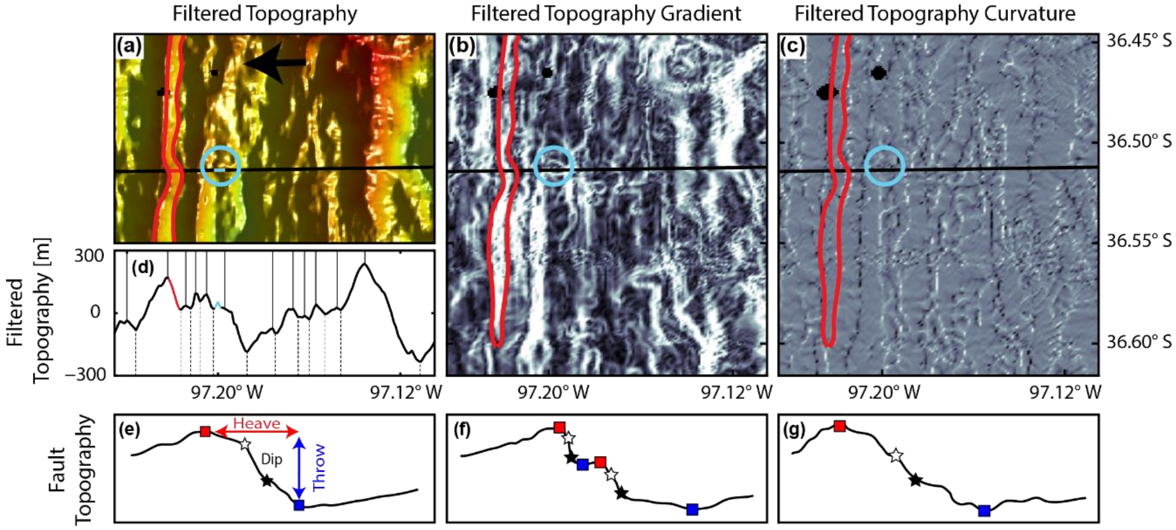

Figure 3.4. Imagery used to distinguish faults (bold red lines) from volcanic/hummocky topography (bold light-blue circles) for segment N1 include shaded relief maps of (a) filtered bathymetry (black arrow shows spreading direction), (b) gradient and (c) curvature of the high-pass (containing short wavelengths) filtered bathymetry. The black line indicates an example flowline transect along which the profile of filtered bathymetry (d) was taken. In (d), picks of fault tops and bottoms are marked by solid and dashed lines, respectively; red and light-blue sections show the highlighted fault and cone in (a-c). (e-g) Example profiles of faults are shown with picks used to measure fault throw, marked by red and blue squares, and to estimate fault scarp dip, marked by white and black stars. Examples include (e) a profile with a clear fault top, bottom, and scarp face, (f) two terraced faults, and (g) a profile that is more difficult to interpret due to a highly degraded fault scarp.

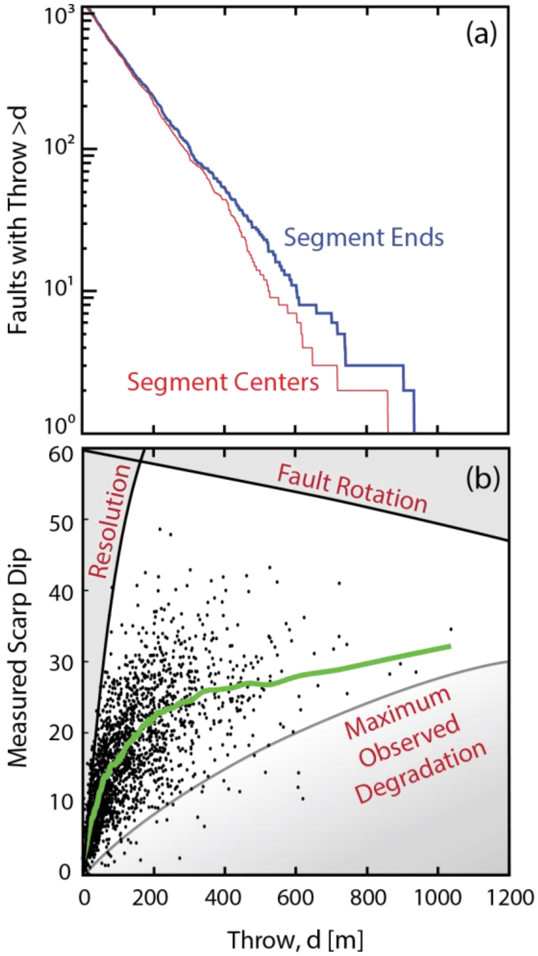

Figure 3.5. (a) Cumulative frequency distribution of fault throws for faults nearer to segment offsets than segment centers (blue line) and nearer to segment centers than segment offsets (red line). The nearly straight lines in these plots indicate approximately exponential distributions, which is predicted for a population of faults having lengths comparable to or greater than the brittle layer thickness [*Cowie et al.*, 1993; *Carbotte and Macdonald*, 1994a]. (b) Measured fault dip (dots) and median measured fault dip (green line) versus throw. Curve marked "Resolution" shows the predicted maximum angles that can be resolved by the 100-m gridding of the bathymetry data. Curve marked "Fault Rotation" is the predicted rotation of an individual fault with increasing throw in a 2 km thick elasto-plastic plate overlaying a viscous asthenosphere [*Olive and Behn*, 2014]. The lowermost curve was sketched by eye to mark the approximate trend of an increase in the minimum angles with throw.

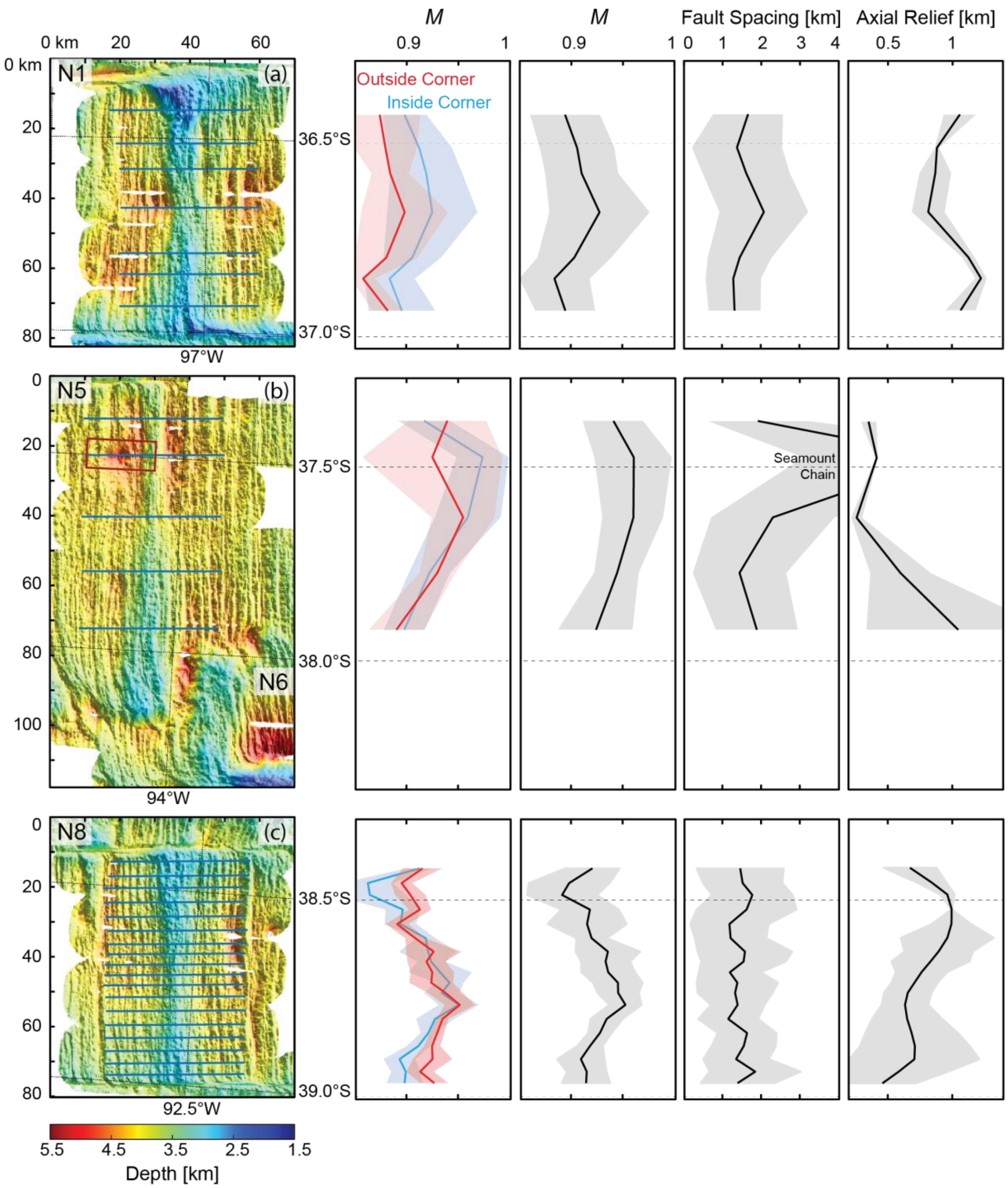

Figure 3.6. Chile Ridge bathymetry maps of studied segments (a) N1 (b) N5 (c) N8 (d) N9N, N9S (e) N10 (f) V5 and (g) S5N, S5S showing transects taken along spreading flow-lines (blue lines) used to identify and measure faults, and to calculate axial relief. From left to right, the accompanying columns are: estimates of mean *M* (lines) and one standard deviation (colored backgrounds) for transect halves grouped by proximity to outside (red) and inside (blue) corners, estimates of total mean *M*, mean fault spacing, and axial relief (black lines) with one standard deviation (grey background) for whole transects.

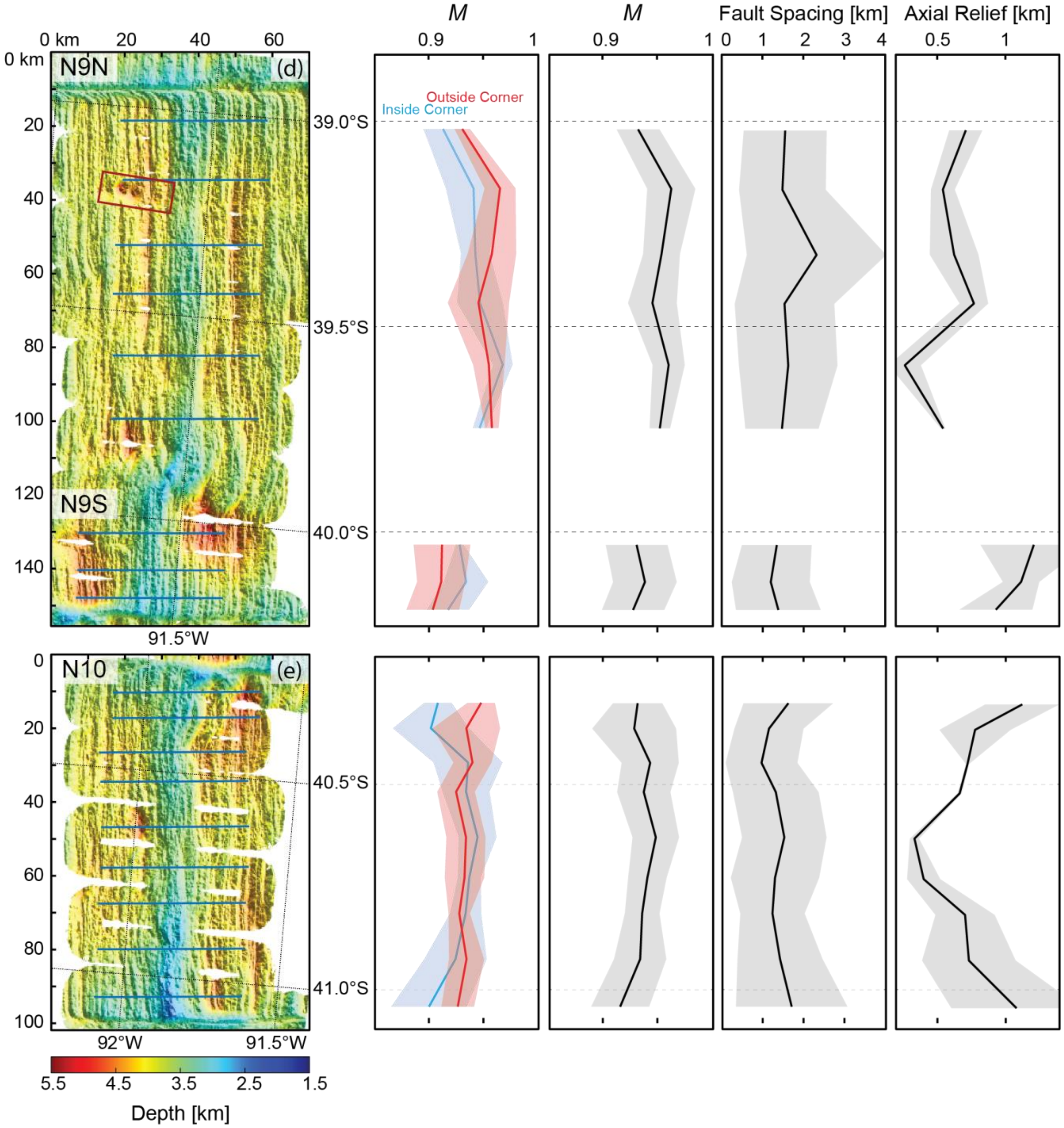

Figure 3.6 continued

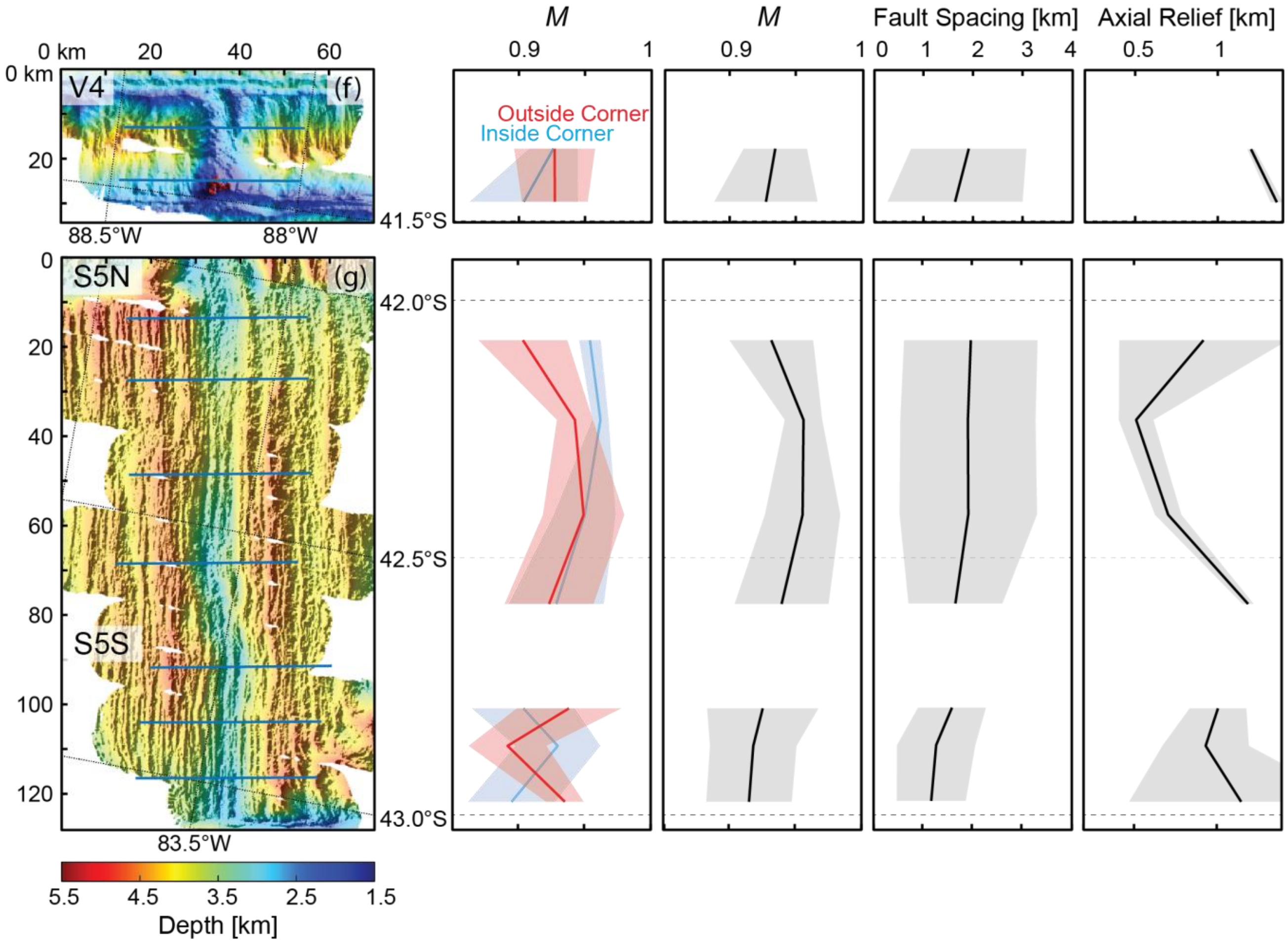

Figure 3.6 continued

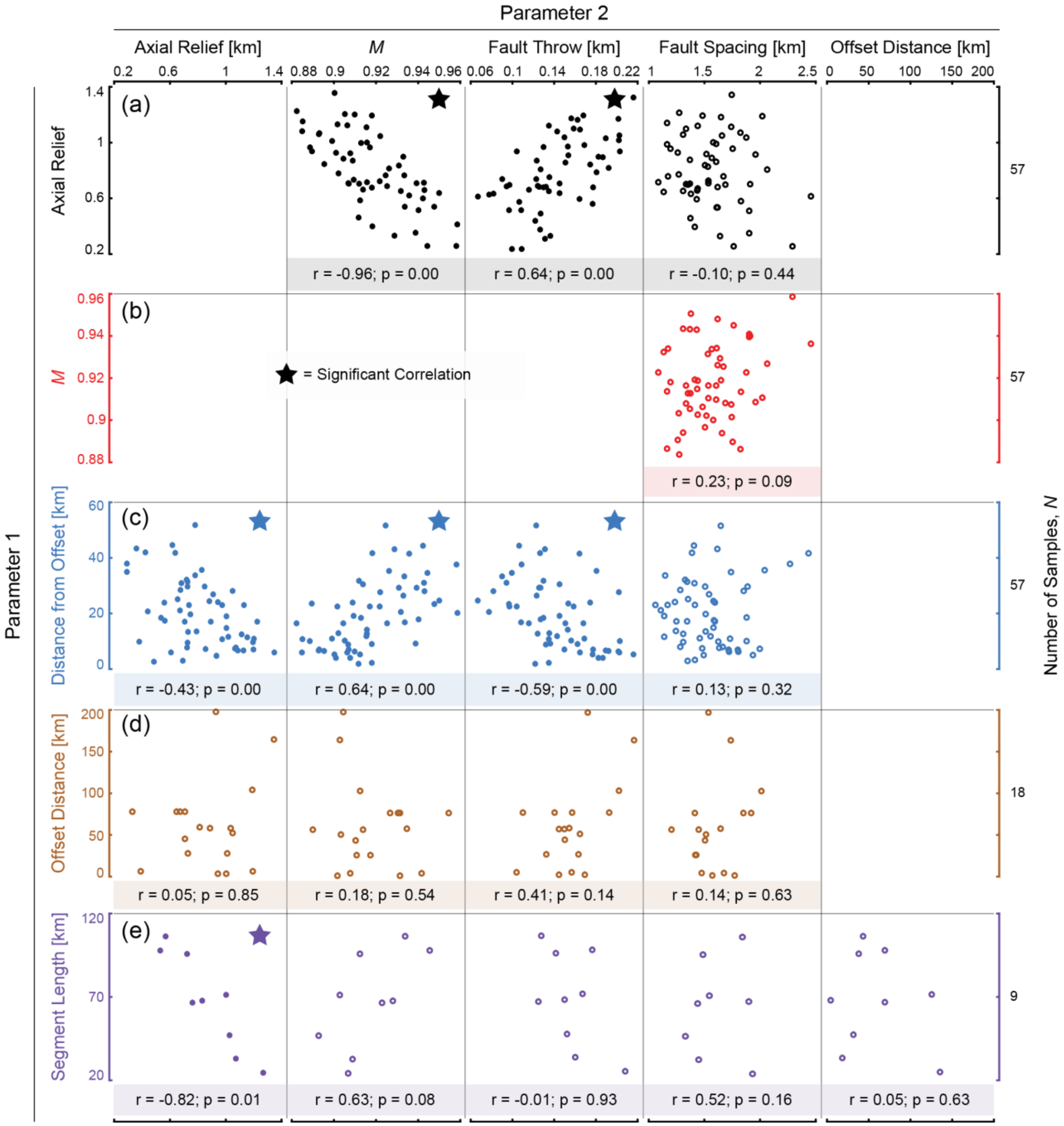

Figure 3.7. Plots showing correlations of (a) axial relief, (b) *M*, (c) distance of the transect from the nearest offset, (d) segment offset distance, and (e) segment length with each measured parameter. Color shaded boxes contain Spearman's rank correlation coefficient, *r*, and a *p*-value. The *p*-value is the probability that a correlation as strong as or stronger than measured would result from a distribution with no correlation through random change and incomplete sampling of the data. We consider a *p*-value less than 0.05 to be significant. Significantly correlated pairs have filled symbols and are marked by a star.

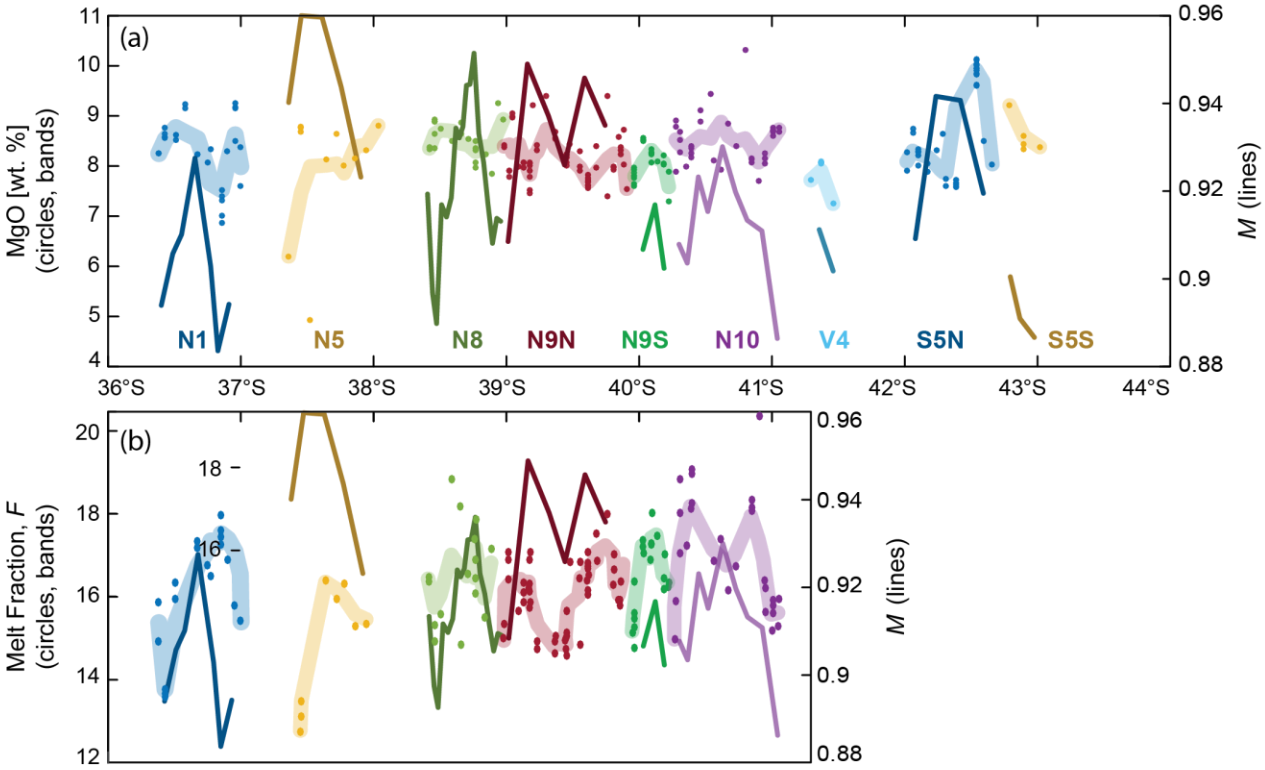

Figure 3.8. Estimated values of (a) MgO content of seafloor basalts and (b) extent of partial melting (in %, colored circles, [*Milman*, 2002]) and values smoothed with a 2 km moving-average window (shaded and colored bands) are shown alongside estimates of *M* (colored lines) for each of the studied segments where geochemical analyses were available.

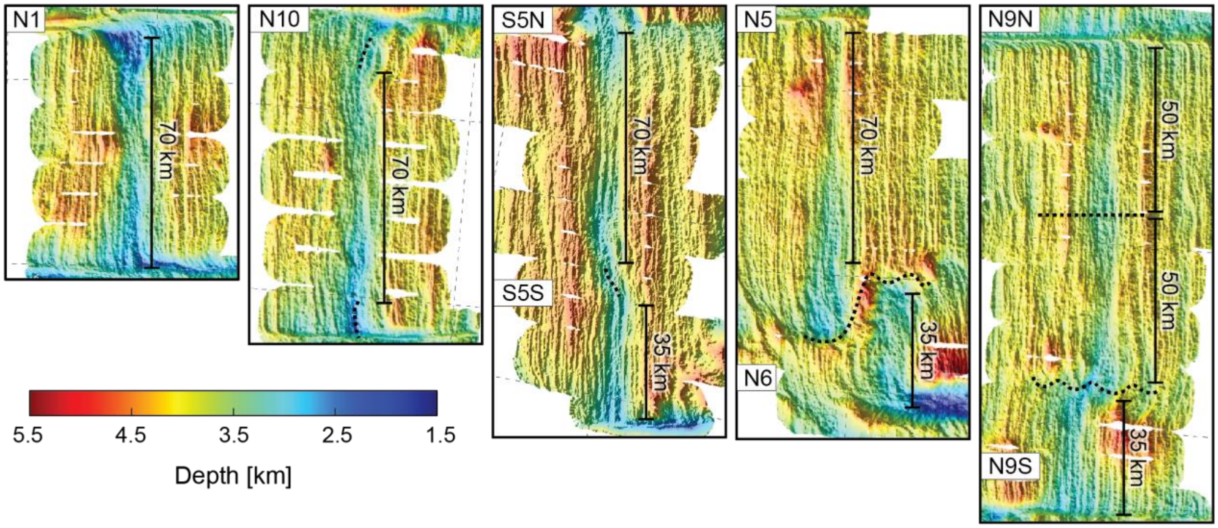

Figure 3.9. Seafloor bathymetry maps of five studied segments. Black bars follow straight, hourglass-like portions of the ridge axis to indicate magmatic segmentation, and dashed lines show magmatic segment boundaries. As the distance between transform offsets lenghtens, the axial valley deviates from linear strike, leading to non-transform offsets and traditional tectonic segmentation of the ridge axis.

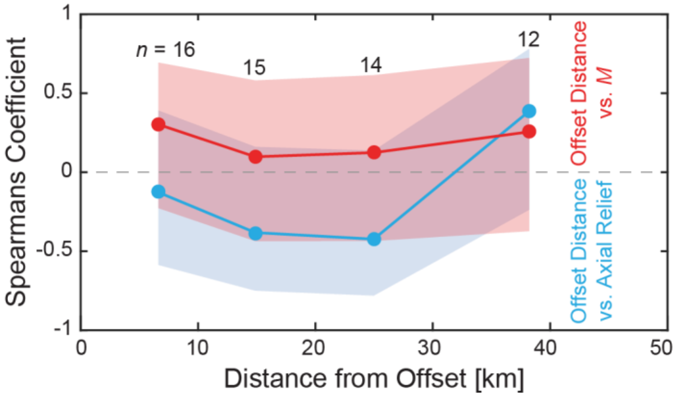

Figure 3.10. Spearman's correlation coefficients and 95% confidince intervals for correlations between offset distance and *M* (red) and axial relief (blue). Correlations were calculated for transects in 10 km bins of along-axis distance from an offset; all distances ≥ 30 km were included in the same bin to maintain similar sample sizes. Data are plotted at the bin mean offset distance, and the plotted numbers show the sample size, *n*, contained in each bin. Confidence intervals for each bin cross zero, showing that within 95% confidince, there are no distinguishiable relationships between offset distance and the estimated parameters at any point along the ridge segments.

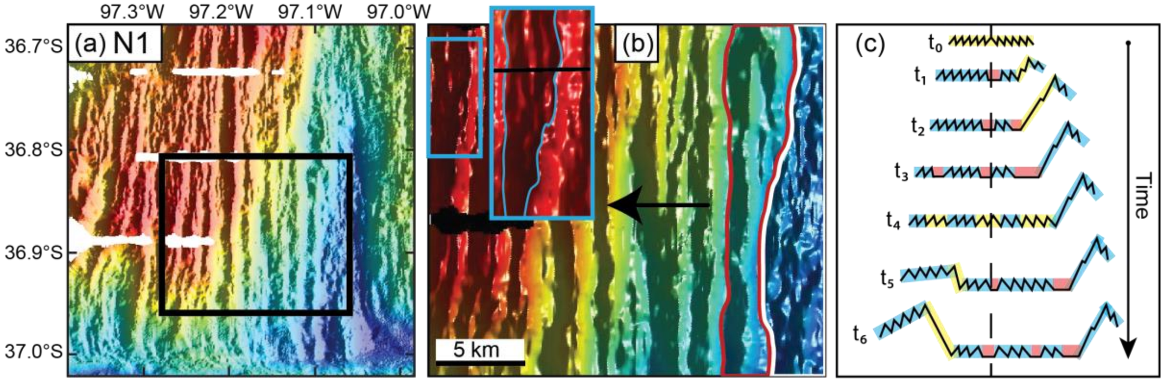

Figure 3.11. (a) Shaded relief map of segment N1 multibeam bathymetry. (b) Close-up of the black rectangle shown in (a). The black arrow shows the spreading direction. The white line in (b) marks the western edge an area of diffuse deformation, where many small sinuous faults occur near the axis. As these small faults move away from the ridge axis, strain begins to concentrate on a few faults that link together along-axis and quickly grow into large abyssal-hill scale faults (the youngest in this panel is outlined by red line). With continued seafloor spreading the large fault stops slipping [*Buck et al.*, 2005b; *Behn and Ito*, 2008] and diffuse extension on small faults accommodate the tectonic extension in the axial zone, beginning the process again. The small blue box shows the location of the subset enlarged footwall region of an older, now inactive abyssal hill scale fault, which still preserves the small-scale axial fault fabric highlighted on the back of the fault. (c) Cartoon illustrating fault evolution with time. At time t_0, a ridge axis undergoes diffuse extension on short, small-throw, sinuous faults (fabric highlighted in yellow signifies active faults). At time t_1, small faults begin to link along the ridge axis, rapidly accumulating strain, and form an abyssal hill scale fault by time t_3 that rafts abandoned axial fabric (fabric highlighted in blue signifies inactive faults) on the footwall. During this time, magmatic extension contributes to spreading (fabric highlighted in red). At time t_4, the abyssal hill scale fault is inactive and the axis again undergoes diffuse extension, and the process repeats.

CHAPTER 4. IMPACT OF VARIABLE MAGMA INJECTION RATES ON FAULTING AND MORPHOLOGY AT INTERMEDIATE SPREADING MID-OCEAN RIDGES: A 3-D NUMERICAL MODELING APPROACH

Abstract

Previous two-dimensional (2-D) modeling studies of fault generation and lithosphere bending at mid-ocean ridges broadly explain the globally observed trends in abyssal hill spacing and ridge axis morphology. However, these modeling efforts do not address how changes in magma supply along a ridge segment lead to the inherently 3D variability of faulting and axial morphology at intermediate and slow-spreading ridges. To this end, we use the geodynamic modeling software LaMEM to simulate high-resolution, 3-D tectonomagmatic interactions in a visco-elasto-plastic lithosphere under extension. We model a single ridge segment subjected to an along-axis gradient in the rate of magma injection, which is simulated by imposing a mass source proportional to the fraction of magmatic extension, *M*, in a plane of model finite volumes beneath the ridge axis. We find that thick lithosphere leads to strong coupling across the magma injection zone such that faults initiate sequentially on alternating sides of the ridge axis. In contrast, thinner lithosphere leads to weak across-axis coupling and promotes faulting on only one side of the ridge axis. In models with variable injection rates imposed along-axis, strong along-axis coupling can destabilize long-lived detachment faults when the lithosphere is thick and lead to smaller spacing along low-*M* portions of a ridge segment. Models also form axial valleys whose depths increase with lithospheric thickness, but also increase proportional to fault throw. Finally, our models explain the presence of smaller fault blocks near long-lived detachments faults as reflecting strong along-axis variations in *M*, rather than the presence of "rider blocks" and minimal variations in *M*.

4.1. Introduction

The axial structure and tectonic fabric of mid-ocean ridges (MORs) are inherently three-dimensional (3-D). Ridge morphology and faulting characteristics change both along and across individual ridge segments in response to variations in magma supply and lithospheric thickness [e.g. *Edwards et al.*, 1991; *Carbotte and Macdonald*, 1994b; *Goff et al.*, 1997]. This 3-D behavior is most prevalent at slow and intermediate spreading rate segments, which can exhibit relatively deep, wide axial valleys bounded by large-offset normal faults near segment ends that transition to shallow, narrow axial valleys characterized by small-offset faults near segment centers [*Chen and Morgan*, 1990b; *Shaw*, 1992; *Shaw and Lin*, 1993; *Howell et al.*, 2016]. Whereas observations of MORs reflect fundamental tectonomagmatic influences on faulting and ridge structure both across and along ridge segments, most geodynamic studies have focused on two-dimensional (2-D) variability across ridge segments.

The prevailing explanation for the origin of axial valleys and the their variability along axis are based on 2-D numerical simulations of seafloor spreading by *Chen and Morgan* [1990b]. Their models, which included variable strength and width of the failure zone, considered pulling on the cool, strong part of the crust and mantle, or lithosphere. They found that dynamic stresses in thicker on-axis lithosphere, defined by the depth at which the brittle lithosphere becomes ductile at the spreading axis, induce deeper axial valleys and shallower valley flanks than those in thinner lithosphere. More recent work by *Ito and Behn* [2008] found that in addition to lithosphere thickness, the relief of the ridge axis and transition from axial valley to axial high was also heavily influenced by the time-averaged magma injection rate.

Studies of the mechanical processes influencing fault characteristics and axial morphology have emphasized 2-D numerical models of seafloor spreading with magmatism and spontaneous fault development [*Buck et al.*, 2005a; *Behn and Ito*, 2008; *Ito and Behn*, 2008]. These studies found that a key parameter is the fraction of the total extension relieved through magma injection, M. Fault spacing was found to increase for higher values of M and for thicker lithosphere. Interpretations of the causes of along-axis variations in observed fault characteristics and axial relief in real-world ridge environments have been based on scaling laws developed in these studies [e.g. *Howell et al.*, 2016]. However, such interpretations may be incomplete because the 2-D modeling studies did not capture the effects of 3-D "coupling", or the dependence of faulting and topography in one part of a ridge segment to magmatism, faulting, and topography in another part. This coupling includes variation and transfer of stresses, as well as variations in M and lithospheric thickness, from one part of the system to another.

Studies of the 3-D mechanical influences on axis morphology and faulting have been more rudimentary and relatively few. Early efforts by *Shaw and Lin* [1993], for example, emphasized 3-D thermal structure without directly modeling realistic mechanical effects. This study predicted that mantle upwelling rates and magma production are more subdued near the ends of segments, producing thicker lithosphere and creating the mechanical conditions to build larger faults and deeper axial valleys. Another study by *Behn et al.* [2002] emphasized stress predictions in lithosphere within and around transform faults bounding ridge segments, which can influence the orientation of nearby normal faults. While these studies have identified influences on the mechanics of faulting and axial topography in 3-D, they did not predict the spontaneous formation and evolution of faults in response to lithospheric stresses.

Quantitative models of self-consistent fault formation and topographic development in 3-D has been simulated in only a small handful of studies. Large scale studies of plume-rift interaction and transform faulting [*Gerya*, 2013a; *Koptev et al.*, 2015] have predicted spontaneous faulting in a visco-plastic lithosphere. Other studies of visco-plastic lithosphere faulting have described how the bulk morphology of mid-ocean ridges initiates and evolves with spreading rate, and the source and style of ridge segmentation and transform faulting [*Gerya*, 2010a; *Gerya*, 2013b; *Püthe and Gerya*, 2014]. At the time of this study, only the emerging models of *Tian and Choi* [2016] have considered the effect of variable along-axis magma injection rates on faulting and ridge morphology for a 3-D, fully visco-elasto-plastic lithosphere. Their models predict that long-lived detachment faults and neighboring abyssal hills at slow spreading ridges are controlled by along-axis gradients in M, but they explored a limited range of variations in M and did not address the effects of lithospheric thickness or axial relief.

The main objectives of this study are to characterize how along-axis variations in M influence along-axis variations in fault characteristics and ridge axis relief, and how these influences change for different lithospheric thicknesses. To accomplish this, we simulate high-resolution 3-D tectonomagmatic interactions in a visco-elasto-plastic lithosphere under extension, as well as use semi-analytical solutions of fault spacing based on simple force-balance arguments. The topography and lifecycle of faulting predicted by our models motivate future studies of fault weakening and healing, describe the impact of coupling on the evolution of faulting and topography, illustrate the role of fault throw in producing axial relief, and describe the evolution of MOR segments that exhibit oceanic core complexes.

4.2. Numerical method

We model a single mid-ocean ridge segment in which seafloor spreading is partially accommodated by magma accretion and partially accommodated by normal faulting (Figure 4.1). To simulate seafloor spreading, we pull oceanic lithosphere apart at the sides of a Cartesian box. The cool lithosphere deforms both elastically and brittlely, and overlays a low-viscosity, warm asthenosphere, and increases linearly in thickness from H_0 at the axis to $2H_0$ at 20 km off-axis. This off-axis thickening of the lithosphere proportional to H_0 simulates rapid, hydrothermal cooling of the lithosphere to a distance 20 km, and much slower, conductive, cooling beyond 20 km [*Phipps Morgan and Chen*, 1993b]. An upper ocean layer allows the lithosphere to deform, capturing the topographic evolution. The ridge axis is defined by a magma injection zone (MIZ), where an imposed volume flux simulates the accretion of magma to form new lithosphere. The injection flux can vary along the axis and imposes the fraction of total extension that is accommodated by accretion, *M*. The remaining fraction of spreading (1-*M*) is accommodated by normal faulting. We aim to relate the nature of these faults and longer wavelength flexural topography to imposed quantities, such as *M* and on-axis lithosphere thickness, H_0. A list of symbol descriptions, units and values is provided in Table 4.1.

4.2.1. Governing equations and mathematical model

The above system is modelled mathematically using the equations for conservation of mass and conservation of momentum for a viscous continuum with zero Reynolds number,

$$\frac{\partial v_i}{\partial x_i} = \begin{cases} 0 & , \quad \text{outside of MIZ} \\ \dfrac{2Mu_{1/2}}{w_{\text{MIZ}}} & , \quad \text{inside of MIZ} \end{cases} , \tag{1}$$

$$\frac{\partial \sigma_{ij}^{'}}{\partial x_j} - \frac{\partial P}{\partial x_i} = -\rho g_i \, . \tag{2}$$

Here, repeated indices in a term imply summation over the three index values, denoting the three Cartesian directions. In the continuity equation (1), v_i and x_i are respectively the Cartesian components of velocity and position, w_{MIZ} is the width of the magma injection zone, and $u_{½}$ is the half-spreading-rate. In the momentum equation (2), $\sigma_{ij}^{'}$, *P*, *ρ*, and g_i are the deviatoric stresses, pressure, density, and acceleration due to gravity, respectively.

Simulating the MIZ by imposing a source term to the continuity equation imposes the desired change in velocity across the MIZ. This is preferable to specifying the absolute velocity on either side of the injection zone because the imposed divergence allows the background MIZ velocity to respond dynamically to lithospheric stresses, and allows faulting to occur on one side or both sides of the ridge axis (Figure 4.2).

This system of equations is closed with a constitutive law that relates deviatoric stresses to strain rates $\dot{\varepsilon}_{ij}$. The constitutive relation is relatively complex because is captures ductile (viscous) deformation in the asthenosphere and warmer parts of the lithosphere, the elastic flexure of the lithosphere, and the brittle (plastic) failure of lithosphere faults.

Ductile deformation is controlled by a creep viscosity, η_v and is an Arrhenius function of temperature. To incorporate elastic deformation, we assume a Maxwell material with elastic modulus, *G*,

$$\dot{\varepsilon}_{ij} = \frac{1}{2\eta_v} \sigma_{ij}^{'(t)} + \frac{1}{2G} \frac{\sigma_{ij}^{'(t)} - \sigma_{ij}^{'(t-\Delta t)}}{\Delta t} , \tag{3}$$

where *t* is time, and the time derivative of stress is discretized by forward time differencing, with Δt being the computational "visco-elastic" time step [*Moresi et al.*, 2003; *Gerya*, 2010b]. Solving

(3) for the ratio of stress to strain rate yields an effective viscosity that captures the ductile and elastic deformation, η_{ve},

$$\eta_{ve} = Z\,\eta_v \;, \tag{4}$$

where the visco-elastic ratio, Z, is

$$Z = \frac{G\Delta t}{G\Delta t + \eta_v} . \tag{5}$$

When Δt is small, the visco-elastic ratio will approach 0, and the material will primarily deform elastically. Conversely, when Δt is large and Z approaches 1, the material deforms viscously.

Finally, brittle failure is simulated by limiting the effective viscosity such that the second invariant of deviatoric stress, $\sigma_{II}^{'}$, never exceeds the yield stress, σ_Y,

$$\eta_{vep} = \begin{cases} \eta_{ve} & , \quad \sigma_{II}^{'} < \sigma_Y \\ \dfrac{\sigma_Y}{2\dot{\varepsilon}_{II}} & , \quad \sigma_{II}^{'} \geq \sigma_Y \end{cases} . \tag{6}$$

The yield stress is determined by enforcing the Drucker-Prager yield criterion [*Patterson and Wong*, 2005],

$$\sigma_Y = P\,\sin(\phi) + C\,cos(\phi) \,, \tag{7}$$

where ϕ is the friction angle and C is the cohesion.

The deformation in regions limited by σ_Y is referred to as "plastic" strain, and these deformation regions tend to localize in bands that resemble fault zones. This plastic deformation is tracked through time and used to calculate an accumulated plastic strain, ε_{aps}. We impose a cohesion law such that C decreases linearly with ε_{aps} to simulate damage-induced weakening of rock material [*Poliakov and Buck*, 1998],

$$C = \begin{cases} \dfrac{C_0\left(1 - \dfrac{\varepsilon_{aps} - \varepsilon_{crit,1}}{\varepsilon_{crit,2} - \varepsilon_{crit,1}}\right)}{0} & , \quad \varepsilon_{crit,1} \leq \varepsilon_{aps} < \varepsilon_{crit,2} \\ & , \quad \varepsilon_{aps} \geq \varepsilon_{crit,2} \end{cases} , \tag{8}$$

where C_0 is the initial cohesion, $\varepsilon_{crit,1}$ is the critical strain required for the onset of cohesion loss, and $\varepsilon_{crit,2}$ is the critical strain required for full cohesion loss. In addition to this weakening mechanism, we simulate "healing" of the damaged rock by decreasing the accumulated plastic strain with time [*Poliakov and Buck*, 1998],

$$\varepsilon_{aps}^{t} = \varepsilon_{aps}^{t-\Delta t}\left(\frac{\Delta t}{\tau}+1\right)^{-1} . \tag{9}$$

The rate of healing is controlled by the imposed healing timescale, τ. Thus, plastic shear deformation tends to localize into bands (fault zones) when tectonic plastic strain growth outpaces the time-healing decay, and accumulated strain builds to the critical value.

With this fully visco-elasto-plastic behavior and the corresponding constitutive relationship, the momentum equation (2) becomes

$$\frac{\partial}{\partial x_j}\left(\eta_{vep}\left(\frac{\partial v_i}{\partial x_j}+\frac{\partial v_j}{\partial x_i}\right)\right)-\frac{\partial P}{\partial x_i} = -\rho g_i - \frac{\partial}{\partial x_j}\Big(\left(1-Z\right)\sigma_{ij}^{\prime(t-\Delta t)}\Big). \tag{10}$$

4.2.2. Computational method

To solve the above equations, we use LaMEM [*Kaus et al.*, 2016], a finite element / marker-in-cell [*Gerya*, 2010b] code designed for high-performance scientific computing that is built upon Portable, Extendable Toolkit for Scientific Computation (PETSc) data structures and libraries for scalable, parallel solving of partial differential equations [*Balay et al.*, 2015]. The governing equations are discretized on a fully staggered, finite difference grid (Figure 4.3). The staggered grid was chosen to reduce the number of unknowns in the central difference problem, to properly conserve stresses when using variable viscosities, and to increase solution accuracy [e.g. *Fornberg*, 1995; *Gerya*, 2010b]. For example, the discretized continuity equation (1) is

$$\frac{v_{x_{i+1}}-v_{x_i}}{\Delta x_i}+\frac{v_{y_{j+1}}-v_{y_j}}{\Delta y_j}+\frac{v_{z_{k+1}}-v_{z_k}}{\Delta z_j} = \begin{cases} 0 & , \quad \text{outside of MIZ} \\ \dfrac{2Mu_{1/2}}{w_{\text{MIZ}}} & , \quad \text{inside of MIZ} \end{cases} . \tag{11}$$

The matrix equation for the discretized governing equations can be arranged as

$$\mathbf{L}\bar{\mathbf{x}} = \begin{bmatrix} \mathbf{K} & \mathbf{G} \\ \mathbf{G^T} & 0 \end{bmatrix}\begin{bmatrix} \boldsymbol{v} \\ P \end{bmatrix} = \begin{bmatrix} \text{momentum rhs} \\ \text{continuity rhs} \end{bmatrix} = \bar{\mathbf{R}} . \tag{12}$$

Here, $\bar{\mathbf{x}}$ is the solution vector containing the velocities, ***v***, and pressures, *P*, being solved for, and $\overline{\mathbf{R}}$ is the effective body-force vector containing the right-hand side terms of the continuity (1) and momentum (10) equations. $\bar{\mathbf{x}}$ and $\overline{\mathbf{R}}$ have entries for each governing equation (continuity, *x*-momentum, *y*-momentum, and *z*-momentum) evaluated at each element. The $m \times m$ coefficient matrix, **L**, is composed of discrete "blocks"; the **K** submatrix is the velocity stiffness matrix, and **G** and $\mathbf{G^T}$ are the gradient and divergence operators, respectively (Figure 4.4).

This is a nonlinear equation because the plastic and elastic viscosity contributions to **L** depend on the velocity, which is contained in $\bar{\mathbf{x}}$. Thus, at each time step, the discretized coupled system of equations is solved using the preconditioned Jacobian-Free Newton-Krylov (JFNK) method [*Knoll and Keyes*, 2004] with line-search, as implemented in the PETSc Scalable Nonlinear Equations Solver (SNES) nonlinear solver framework [*Balay et al.*, 2015; *Kaus et al.*, 2016],

$$\mathbf{A}^{-1}\mathbf{J}\left(\bar{\mathbf{x}}_k\right)\partial\bar{\mathbf{x}}_k = -\mathbf{A}^{-1}\bar{\mathbf{r}}\left(\bar{\mathbf{x}}_k\right), \quad \bar{\mathbf{x}}_{k+1} = \bar{\mathbf{x}}_k + \alpha\,\partial\bar{\mathbf{x}}_k \, . \tag{13}$$

Here, **A** acts as a preconditioning matrix, $\partial\bar{\mathbf{x}}_k$ is the correction vector for each JFNK iteration, $\bar{\mathbf{r}}$ is the residual vector, $\bar{\mathbf{r}} = \mathbf{L}\,\bar{\mathbf{x}} - \bar{\mathbf{R}}$, α is a parameter that tunes the line-search step length, and *k* is the iteration number. The preconditioning matrix **A** is equal to the **L** matrix when using only the current velocity estimate to calculate viscosity and populate matrix coefficients. The full Jacobian matrix, $\mathbf{J}$, is the partial derivative of the residual,

$$\mathbf{J} = \frac{\partial\bar{\mathbf{R}}}{\partial\bar{\mathbf{x}}} \, . \tag{14}$$

However, solving for this is computationally expensive, and is avoided by approximating the matrix-vector product on the left-hand-side of (13) using finite differencing.

Within each iteration, we must also solve the linear inverse problem. To take advantage of massively scalable computing resources, the inversion of the preconditioning matrix is approximated using a multigrid method. This iterative method performs operations at resolutions coarser than the original grid, reducing the complexity of the problem, and then interpolates those solutions back to the finer grids. Solutions at coarse levels are obtained directly using LU decomposition, while solutions at fine levels are found iteratively using the flexible generalized minimal residual method (FGMRES). This process continues until the change in the solution converges to a specified tolerance.

After each full nonlinear solve, the computational time step is calculated according to the maximum model velocity, the minimum element dimension, and the dimensionless Courant-Friedrichs-Lewy condition number, *CFL*,

$$\Delta t = CFL\left(\min\left(\frac{\Delta x_i}{v_i}\right)\right). \tag{15}$$

This is chosen to preserve solution accuracy while maintaining the viscous behavior of the asthenosphere and elastic behavior of the lithosphere. Time evolution is then simulated by updating the stress, accumulated strain, viscosity, and pressure quantities that are stored on Lagrangian markers. Initially ~ 125 markers are placed randomly within each finite element cell. The markers are advected using a fourth-order Runge-Kutta interpolation in space according to the solution velocities and computational time step. The imposed thermal structure (described below in section 4.2.3) is then reapplied to the markers, plastic healing of accumulated strain occurs per the computational time step and specified healing rate, and the process repeats.

4.2.3. Numerical model design

The geometry and boundary conditions of the numerical model are shown in Figure 4.1. The Cartesian model box extends 50 km along-axis, 80 km across-axis, and 30 km in height, at a resolution of 128 × 256 × 128 elements (240 – 390 m spacing). We include three layers: a low-viscosity water layer, an elasto-plastic lithosphere, and a viscous asthenosphere. The magma injection zone is imposed in a plane of elements beneath the ridge axis, such that $w_{\mathrm{MIZ}} = \Delta x_{axis}$.

The water layer has an imposed viscosity of 1×10^{17} Pa-s that is independent of temperature, while the ductile viscosity of the mantle obeys an Arrhenius temperature dependence [*Hirth and Kohlstaedt*, 2003]. While this viscosity is large compared to the viscosity of water in nature, the viscosity is high enough to promote numerical stability and low enough to allow the much higher viscosity lithosphere to deform without significant resistance. In this initial study of the 3D mechanics of faulting with magmatic accretion the temperature structure is imposed—rather than allowed to evolve dynamically—so that we can precisely control the structure of the brittle layer. The imposed structure is one that simulates the natural increase in lithospheric thickness with age as caused by a combination of conductive and hydrothermally advective heat loss [*Behn and Ito*, 2008]. Temperature increases linearly with depth from 0 °C at the surface to 600 °C at a depth H, as η_v decreases from 1×10^{24} to $\sim1\times10^{20}$ Pa-s. The temperature then increases to 1,300 °C across a thermal boundary layer of thickness ½ H as the lithosphere transitions to asthenosphere, while η_v decreases to $\sim1\times10^{18}$ Pa-s. For each time step, the lithosphere structure is draped beneath a passively-advected free surface that tracks the seafloor topography.

We model a lithosphere that increases from a thickness H_0 at the ridge axis to $2H_0$ at a distance 20 km off-axis before flattening out [*Behn and Ito*, 2008]. Thus, the off-axis lithospheric thickening rate is proportional to H_0. Lithosphere extension is imposed using a Dirichlet velocity boundary condition at the sides of the domain set to equal the intermediate half-spreading rate, $u_{½}$, of 30 cm/yr. The bottom of the model is open to allow the inflow of asthenosphere to naturally respond to the dynamic behavior of the lithosphere. The top of the model imposes an inflow water velocity that conservatively balances water outflow from the sides.

4.3. Semi-analytical and numerical models of uniform magma injection rate

We first consider models in which the imposed along-axis injection rate in the MIZ is uniform along the ridge segment. While these models are fully 3-D, their configuration varies only in the across-axis direction and with depth, making them suitable for comparison with well-established fault spacing predictions that consider 2-D fault evolution. In these models, we vary M and the imposed lithospheric thicknesses beneath the ridge axis. We then measure the resulting spacing of faults and long-wavelength axial relief, and compare these measurements to semi-analytical force-balance predictions of fault spacing for a 2-D elasto-plastic plate [e.g. *Forsyth*, 1992; *Buck*, 1993; *Lavier et al.*, 2000; *Behn and Ito*, 2008].

4.3.1. Semi-analytical solutions for 2-D fault spacing

The main concepts behind the force-balance-derived solutions for fault spacing are based on prior 2-D numerical models, which predicted alternating faults that tend to be most active on one side of the ridge at a time (Figure 4.5) [*Forsyth*, 1992; *Buck*, 1993; *Lavier et al.*, 2000; *Behn and Ito*, 2008]. Near the onset of extension, plastic strain begins to accumulate in the lithosphere and cohesion weakening acts to localize deformation onto a single active fault. This fault accommodates the full fraction of tectonic extension, (1-*M*), on a single side of the ridge axis, while the MIZ accommodates the remaining magmatic fraction of extension, *M*. With continued slip, the active fault rotates to a shallower dip and migrates into thicker lithosphere due to spreading accommodated in the MIZ at the ridge axis. Eventually, the force required to continue slip on the shallow fault penetrating thick lithosphere is greater than that required to break a new fault near the ridge axis. The old fault stops slipping and the new fault takes up the tectonic fraction of extension, beginning the cycle anew.

Force balance framework

This mathematical model for the evolution of lithospheric forces with increasing fault slip predicts that new normal faults form adjacent to the ridge axis whenever the force required to continue slip on the active fault exceeds the force required to break the axial lithosphere and initiate a new fault, F_I. The force balance is expressed as,

$$F_F + F_B \geq F_I \ . \tag{16}$$

where the force required to continue slip on the active fault is the sum of the force required to overcome the frictional strength of the fault, F_F, and the force required to bend the adjacent lithosphere, F_B. This equation is used to predict the total fault heave and the distance off-axis each fault remains active, and therefore how the spacing of faults relates to key variable such as *M*, *H*, and weakening of the lithosphere. The derivation of these fault characteristics is as follows.

The force required to initiate a new fault on the opposite side of the ridge axis from the active fault is the depth-integrated yield strength of the undamaged axial lithosphere [*Forsyth*, 1992; *Behn and Ito*, 2008], F_I, given by

$$F_I = \frac{\mu \rho g H_0^2 / 2 + H_0 C_0}{\mu \sin(\theta_0)^2 + \sin(\theta_0)\cos(\theta_0)} \ . \tag{17}$$

Here μ is the coefficient of rock friction, ρ is the density, g is the acceleration due to gravity, H_0 is the thickness of the brittle layer at the axis, C_0 is the initial cohesion of the undamaged lithosphere, and θ_0 is the initial fault dip. The force required to overcome friction on the active fault plane is similar to (17), but considers the migration of the fault off-axis into thicker lithosphere due to magmatic spreading at the MIZ, the effect of plastic weakening (8) and healing (9) with continued slip and the associated time, and the rotation of the fault plane to shallower dips with increasing slip [*Forsyth*, 1992; *Behn and Ito*, 2008],

$$F_F = \frac{\mu \rho g H^2 / 2 + HC\left(\varepsilon_{aps}\right)}{\mu \sin(\theta)^2 + \sin(\theta)\cos(\theta)}. \tag{18}$$

The force required to further bend the lithosphere with increasing slip is given by

$$F_B = AH^2\left(1 - e^{-B\Delta h/H}\right), \tag{19}$$

where A and B are empirically derived elasto-plastic lithosphere properties, and Δh is an increment of fault heave, h [*Lavier et al.,* 2000].

To calculate changes in these forces with increasing fault slip, we discretize (17), (18), and (19) using backward finite differences for incremental fault heave. Following *Behn and Ito* [2008], the off-axis distance of the active fault, x_{af}, increases by Δx_{af} for an increase in fault heave of Δh according to

$$x_{af}^{h} = x_{af}^{h-\Delta h} + \Delta x_{af}, \quad \Delta x_{af} = \Delta h\left(\frac{M - 0.5}{1 - M}\right). \tag{20}$$

As the fault migrates off-axis, four key properties also evolve: lithospheric thickness, the angle of the fault plane, time, and accumulated plastic strain (which influences the strength of cohesion on the fault plate). The thickness of the lithosphere changes according to

$$H^h = H^{h-\Delta h} + \Delta x_{af}\frac{\partial H}{\partial x}, \tag{21}$$

where $\partial H/\partial x$ is the slope of the lithosphere moving away from the ridge axis in the direction, x, of spreading,

$$\frac{\partial H}{\partial x} = \begin{cases} H_0 / 20\text{ km} & , \quad x \leq 20\text{ km} \\ 0 & , \quad x > 20\text{ km} \end{cases}. \tag{22}$$

By draping this thermal structure beneath the numerical model topography each time step, rather than considering the natural evolution of model temperatures, we have precise control over the geometry of the lithosphere [*Behn and Ito*, 2008].

Slip increases and the lithosphere thickens as the fault migrates off-axis, rotating the fault to a shallower dip,

$$\theta^h = \theta^{h-\Delta h} - \frac{\partial \theta}{\partial h}\Delta h, \tag{23}$$

where $\partial\theta/\partial h$ describes the rate of fault rotation with increasing heave [*Behn and Ito*, 2008],

$$\frac{\partial \theta}{\partial h} = \begin{cases} 5\ ^\circ/\text{km} & , \quad \theta > 38^\circ \\ 0 & , \quad \theta \leq 38^\circ \end{cases}. \tag{24}$$

The velocity at which the fault migrates off-axis, u_{af}, depends on the spreading rate and M [*Behn and Ito*, 2008],

$$u_{af} = 2u_{½}(M - 0.5)\,. \tag{25}$$

The rate at which the fault accumulates heave, u_h can be calculated from the fault migration rate and half spreading rate,

$$u_h = u_{½} - u_{af} = 2u_{½}(1 - M)\,, \tag{26}$$

And used to find the amount of time that passes during the finite difference step,

$$\Delta t_h = \Delta h / u_h\,. \tag{27}$$

Finally, we can discretize equations (8) and (9) to write accumulated plastic strain as a function of incremental fault heave,

$$\varepsilon_{aps}^{h} = \left(\varepsilon_{aps}^{h-\Delta h} + \Delta h \sqrt{\left(\frac{1}{\Delta x}\right)^2 + \left(\frac{\tan(\theta^h)}{\Delta z}\right)^2} \right) \left(\frac{\Delta t_h}{\tau} + 1 \right)^{-1}, \tag{28}$$

Where Δx and Δz are width and height of the localized model shear band, respectively, used to calculate incremental strain in the dip-direction. The force-balance (16) is now formulated to consider the discretized accumulated plastic strain (28) in the cohesion law (8), and discretized lithosphere thickness (21) and fault dip (23) in the equations for frictional fault strength (18) and bending force (19). These semi-analytical force-balance solutions are then used to calculate the final heave and off-axis distance of the active fault when the formation of a new fault becomes favored.

Force balance fault spacing predictions

Fault spacing is defined as the distance between the intersection of one fault plane and the hanging wall surface with the same intersection point of the next adjacent fault. To calculate fault spacing, we consider two end-member faulting regimes (Figure 4.6). In the first "one-sided" regime, faulting occurs exclusively on a single side of the ridge axis and new material injected at the MIZ is emplaced asymmetrically across the axis over time, with more material being injected into the unfaulted side. In the second "two-sided" regime, faulting occurs successively on alternating sides of the axis and new material emplaced symmetrically across the axis over time. For the one-sided case, a new fault forms with initial spacing,

$$\Delta S_i^{asymm} = u_{af} t_{af} = x_{af}\,. \tag{29}$$

Accumulated heave on the newly active fault increases its separation from the previous fault, yielding a final spacing of

$$\Delta S_f^{asymm} = \Delta S_i^{asymm} + h = x_{af} + h\,. \tag{30}$$

For the two-sided case, a newly active fault initiates with a spacing from the adjacent inactive fault of

$$\Delta S_i^{symm} = u_{af} t_{af} + u_{½} t_{af} = \left(\frac{M}{M - 0.5} \right) x_{af}\,, \tag{31}$$

and reaches a final spacing,

$$\Delta S_f^{symm} = \Delta S_i^{symm} + h = \left(\frac{1}{M - 0.5} \right) x_{af}\,. \tag{32}$$

The one-sided regime produces more closely spaced faults (on the one side of the ridge axis) than the two-sided regime, all else being equal. Thus, the semi-analytical model of *Behn and Ito* [2008] has been modified to include the time-dependent effects of plastic healing and predict minimum and maximum fault spacing for both the one-sided and the two-sided cases, rather than only the minimum spacing for two-sided faulting.

As shown by *Behn and Ito* [2008], this modified force balance predicts that fault spacing decreases for increasing *M* and H_0 (with the proportional off-axis lithospheric thickening rate) (Figure 4.6a-b). Additionally, we observe that fault spacing predictions can be sensitive to the ratio of the fault slip distance over which plastic healing occurs to the slip distance over which the fault loses cohesion (Figure 4.6c-d). By estimating the healing slip distance-scale as $\tau \times u_h$, we defne a “healing-to-weakening slip ratio” as,

$$\Lambda = \frac{2\tau u_{½}(1 - M)}{\varepsilon_{crit,2}\sqrt{\Delta x^2 + \left(\frac{\Delta z}{\tan(\theta_0)} \right)^2}}\,. \tag{33}$$

For shorter τ and greater *M*, and thus smaller Λ, plastic healing outpaces tectonic strain weakening, and the minimum fault cohesion is non-zero. This results in greater frictional fault strength and decreased fault spacing (Figures 4.6d-e, 4.7). Each numerical model in this study was run with τ = 20 kyr to promote clearly defined fault zones that are adequately resolved over a wide range of *M*.

4.3.2. Numerical models with uniform magma injection rate

We ran 24 models with uniform *M* along the ridge axis: three on-axis lithospheric thicknesses (H_0 = 4, 6, and 7 km) for each of eight different *M* values (0.5, 0.6, 0.65, 0.7, 0.75, 0.8, 0.85, and 1.0). These values of H_0 were chosen because H_0^3 and $H_0^{3/4}$ are approximately evenly spaced, and control the elastic rigidity and flexural wavelength, respectively. Models were run until the initial lithospheric material was completely advected out of the model domain (longer than 1.33 Myr) to minimize any impact of the initial condition on faulting. We then examined the topography of the lithosphere-water boundary (tracked by markers), and calculated fault spacing as well as the longer-wavelength relief of the ridge axis.

Measuring fault spacing and axial morphology

To measure model fault spacing and axial relief, we used the method of *Howell et al.* [2016], designed for analyzing seafloor bathymetry at the intermediate spreading Chile Ridge. Following their approach, we first applied a spectral filter using fast Fourier transforms to separate the topography containing wavelengths longer than and shorter than 20 km (Figure 4.8). This approach separated the short-wavelength (high-pass) structure of individual faults from the long-wavelength (low-pass) flexural morphology of the ridge segment. Faults were then identified in cross-sections of the high-pass topography, and estimates of spacing were made by measuring the distance in x between the westernmost and easternmost fault scarp bottoms on a single side of the ridge axis and dividing by the total number of observed faults.

Axial relief was estimated using cross-sections of the low-pass filtered, long-wavelength topography (Figure 4.8). For models that exhibited an axial valley, axial relief was estimated as the difference in depth between the deepest part of the valley and the mean depth of the shallowest lithosphere flanking the valley to either side. For cases that produced an axial topographic high, axial relief was calculated as the difference in depth of the highest part of the ridge axis and the deepest extent of each flank. Positive relief corresponds to axial highs, and negative relief to axial valleys. The error in axial relief was estimated as the difference in depth of the two axial-valley-bounding flanks.

Uniform injection-rate model results and comparison to semi-analytical solutions

3-D models of uniform along-axis magma injection rates with $M \leq 0.85$ tend to produce two-sided faulting patterns and a median axial valley (Figure 4.9), whereas the models of $M = 1.0$ produce no faults or asymmetry of the seafloor about the ridge axis. The cases with the thinnest modeled on-axis lithosphere, $H_0 = 4$ km, and $M = 0.6 – 0.85$ tended to exhibit two simultaneously active faults on opposing sides of the ridge axis whose lifespans of initiation and slip were out-of-phase, whereas models of $H_0 = 6$ and 7 km predicted a single active fault at a time. The width of the axial valley observed in the unfiltered model topography tends to increase with increasing axial lithospheric thickness and decreasing M. With increasing values of H_0, the depth of the axial valley relative to its flanks (observed in the low-pass filtered topography) tends to increase, whereas fault throw and spacing (observed in the high-pass filtered topography) tends to decrease.

The semi-analytical estimations of fault spacing predict both the magnitude and trend of fault spacing observed in model topography for varying H_0 and M (Figure 4.10). For all lithospheric thicknesses, models of $M = 0.5$ exhibit a single long-lived detachment fault that accommodates half of total model extension on one side of the MIZ, while the MIZ relieves half of total extension of the other side. As M increases from 0.5 to 0.85, fault spacing tends to decrease. Models of H_0 = 6 and 7 km produce faults spacings that fall mostly within the two-sided spacing regime predicted by the semi-analytic solutions.

In contrast, faulting in models of H_0 = 4 km is transitional between the one- and two-sided predictions. Transitional regimes occur when two faults are simultaneously active on opposite sides of the ridge axis. Average fault spacing is least when the active fault lifecycles are perfectly in-sync (i.e. they initiate, accumulate slip, and migrate off axis at the same time and rate), and greatest when fault lifespans are perfectly out-of-sync. Transitional fault spacing ranges from the minimum one-sided prediction to the maximum two-sided prediction for given values of M and H_0.

Measurements of the long-wavelength axial depth show that the axial valley deepens relative to the ridge flanks with increasing lithospheric thickness (Figure 4.11). Additionally, axial valleys tend to deepen with decrease M for all models, and this increase is more pronounced for thicker lithosphere.

4.4. Variable along-axis magma injection rate

To test how along-axis variations in magma injection rates affect fault spacing and ridge morphology, we next consider models in which M varies as a function of distance along the ridge segment. Models were run for values of M that varied between the endmember cases of M = 0.5, where fault spacing and fault heave are predicted to be infinite, to M = 1, where no faults are predicted to form. In total, 27 models were run; for each of nine variations in M, simulations were performed for lithospheric thicknesses of H_0 = 4, 6, and 7 km.

One set of models imposes values of M that increase linearly from M_S = 0.5 in the south (y =0) to $M = M_N$ = 0.6 – 1.0 in the north (y = 50 km). With these modes, we examine how the style of faulting transitions from a single detachment fault associated with theoretically infinite spacing to multiple closely-spaced faults. A second set of models were run with M increasing linearly from M_S = 0.5 – 0.9 to $M = M_N$ = 1. With these modes, we examine how the style of faulting transitions multiple widely-spaced faults to a regime where semi-analytical relations predict no faulting.

4.4.1. Measuring along-axis variations in fault spacing and axial relief

As with the models of uniform injection rate, fault spacing was measured in across-axis profiles of the (high-pass filtered) short-wavelength surface topography. To capture along-axis variations, fault spacing was estimated for ten, 5 km-wide across-axis swaths at each segment. When three or more faults were present on one side of the axis, a standard deviation in fault spacing was found for each half-swath bisected by the ridge axis. Axial relief was measured for each y-value of the finite element grid point of the surface mesh.

4.4.2. Variable injection-rate model results and comparisons with scaling laws

3-D models of variable along-axis magma injection rates and injection rate gradients exhibit one-sided, two-sided, and transitional faulting patterns (Figure 4.12). Simulations of thicker lithosphere and higher M tend to promote two-sided faulting, whereas models of $M_S = 0.5$ tend to form detachment faults with many 10s km of offset on a single side of the ridge axis. In simulations with $M_S \geq 0.6$, faults form on both sides of the MIZ, but sequential faults do not always alternate sides. In every case, moving from the low-M_S, southern edge of the model to the higher-M_N, northern edge, fault throw and spacing tend to decrease, the axial valley tends to narrow, and the axial valley shoals.

The evolution of faulting in the one-sided and two-sided regimes is illustrated in Figure 4.13. The initiation of a new fault in the one-sided regime is demonstrated for a case of $H_0 = 4$ with $M_S = 0.5$ and $M_N = 0.9$. This case typifies the one-sided faulting regime, in that new faults initiate periodically in northern high-M regions—at a frequency that scales with M—and then migrate southward and eventually link with the ongoing detachment fault in the low−M southern region. The initiation of a new fault in the two-sided regime is demonstrated for a case of $H_0 = 7$ km with $M_S = 0.6$ and $M_N = 1$. Here, new faults sometimes propagate from the northern high-M regions southward to the low-M regions on the same side of the axis as an active fault in the south, but at other times initiate along the entire length of the axis opposite the previous fault.

Plots of fault spacing with M show that spacing tends to decrease with increasing values of M and the axial lithospheric thickness (Figure 4.10). In models of the thinnest lithosphere, $H_0 = 4$ km, detachment faults initiate on southern boundary when $M_S = 0.5$ and terminate along the section of the ridge where M is about 0.6 (Figure 4.10a). North of the detachment fault, where $M > 0.6$, fault spacing tends to follow semi-analytical predictions for one-sided faulting. Models of $H_0 = 6$ km exhibit the same behavior of detachment faulting in the south when $M_S = 0.5$ (Figure 4.10b), but show intermediate fault spacing behavior above $M = 0.6$. In contrast to the behavior of the faulting simulations in thinner lithosphere, models of $H_0 = 7$ km and $M_S = 0.5$ do not exhibit infinitely long-lived detachment faults (Figure 4.10b). In models of $H_0 = 7$ km and $M_S = 0.5$, the spacing is smaller along the southern portion of ridge segment where $M = 0.5 – 0.6$ than predicted by semi-analytical solutions and models of uniform M. In the northern portions of the ridge segment where $M \geq 0.7$, fault spacing tends to occur at transitional values or within the two-sided regime. The gradient in M with along axis distance does not appear to have a major effect on fault spacing, as no systematic difference is observed between cases with high gradients (e.g. $M_S = 0.5$ to $M_N = 1.0$) and low gradients (e.g. $M_S = 0.5$ to $M_N = 0.6$).

Plots of long-wavelength axial relief for variable magma injection rate models show similar values and overall trends with the uniform injection rate models having the same axial lithosphere thickness (Figure 4.11): axial-valley depths tend to decrease with increasing local values of M and decreasing H_0. One key difference appears on the north end of the ridge segment for $M_N = 1.0$

where the height of the ridge axis is greatly elevated relative to its flanks compared to uniform *M* cases (Figure 4.11b). Another key difference is apparent for models with $M_S = 0.5 – 0.9$; in these models the southernmost portions of the segment exhibit substantially deeper axial valleys than the uniform *M* models (Figure 4.11c). The overall magnitude and trend in axial relief observed in our models is consistent with estimations of *M* versus axial relief of *Howell et al.* [2016] for the intermediate spreading rate Chile Ridge.

4.5. Discussion

4.5.1. The effect of strain weakening and healing on fault spacing

One piece of insight gained from our modifications to the semi-analytical force balance predictions of *Behn and Ito* [2008] is how the rate of plastic healing can influence faulting (Figures 4.6, 4.7). The common practice among prior geodynamic modeling studies for handling the recovery of cohesion with time to is to impose a constant healing timescale, τ [e.g. *Poliakov and Buck*, 1998; *Buck et al.*, 2005a; *Behn and Ito*, 2008; *Ito and Behn*, 2008; *Olive et al.*, 2014; *Olive et al.*, 2015]. However, what the geologically appropriate value and behavior of τ should be is not known. Selecting a value should therefore be done based on a characterization of the dynamical consequences, which may be guided with appropriate scaling. The *M*-dependent healing-to-weakening length ratio, Λ, is an effective scaling because it ensures that faults both strengthen and weaken at approximately the same rate. Thus, models with the same Λ should share a common dynamic response to healing across a wide range of parameters, including magma injection rates, model resolution, fault localization, and spreading rate. In this study, our choice of τ sets $\Lambda \geq 1$ for all but the highest (≥ 0.9) values of *M*, and for these values of Λ our semi-analytical solutions predict the models behave in a dynamically similar sense (Figure 4.6). The finding of *Tian and Choi* [2016] that faults are more closely spaced for “fast-weakening”, where fault cohesion is lost rapidly, and more widely spaced for “slow-weakening”, where fault cohesion is slowly reduced, are consistent with a change in Λ from being near one to a value less than one. These new semi-analytical force balance solutions motivate future studies that will relate the micro-mechanics of damage weakening and healing to macro-scale understanding fault evolution.

4.5.2. The effect of lithospheric thickness on faulting

In models of uniform *M*, we observe a change from transitional faulting behavior in thin axial lithosphere, where two faults are sometimes simultaneously active on opposite sides of the axis, to two-sided behavior in thick lithosphere, where only one fault is active at a time on alternating sides of the ridge axis. We hypothesize that the difference in faulting regime observed for different lithospheric thicknesses relates to the degree of coupling across the ridge axis. In the extreme case of zero across-axis coupling, faults on each side of the ridge would evolve independently in time from the faults on the other side. The transitional faulting behavior in thin lithosphere partially resembles such a situation. In the other extreme case of infinitely strong coupling, faulting on one side of the ridge axis completely controls the timing and across-axis location of subsequent fault initiation. The two-sided fault behavior in thick lithosphere resembles this end-member.

The simulations of along-axis variations in M show one-sided faulting for H_0 = 4 km, transitional behavior for H_0 = 6 km, and transitional to two-sided faulting for H_0 = 7 km. This result does not change with increasing model width or resolution. The predictions for H_0 = 7 km are consistent with our hypothesis of strong across-axis coupling, and those for H_0 = 6 km are consistent with lower cross-axis coupling. For H_0 = 4 km, the tendency toward one-sided faulting can be interpreted as little or no cross-axis coupling in the sense that the two sides of the ridge axis show distinct behavior from one another (faulting versus no faulting). However, models of H_0 = 4 and 6 km form a persistent detachment fault on the south side of the axis, and we hypothesize that moderate coupling along, rather than across the ridge, is responsible for initiating faults further north exclusively on that same side of the ridge axis. In summary, the first effect of lithospheric thickness with along-axis variations in M is to control the strength of cross-axis coupling and thus the (one- versus two-sided) regime of faulting.

The second influence of lithospheric thickness is on the spacing of faults. A prominent way in which the models of H_0 = 7 km differ from the models of thinner lithosphere is the absence of a single long-lived detachment along the portions of the ridge where $M \leq 0.6$. Instead, single detachments are not as stable and give way to multiple faults, presumably due to the influence of more closely spaced faults forming further north of these areas in higher M portions of the ridge. Thus, we observe a reduced sensitivity of fault spacing to M in these models with the thickest lithosphere that we attribute to strong along-axis coupling. The persistence of long-lived detachment faults where $M \leq 0.6$ in the other models is interpreted as reduced along-axis coupling as an influence on fault spacing owing thinner lithosphere.

These results are consistent with the 3-D modeling efforts of *Tian and Choi* [2016], which find evidence for coupling effects that tend to average M near detachments along the axis. However, they also argue for this effect at higher values of M where along-axis coupling is less obvious in our simulations, and is obscured by a transition in fault regime attributed to across-axis coupling.

4.5.3. The origin of axial relief and the effect of along-axis coupling

The prevailing understanding of the cause of axial valley relief is built upon *Chen and Morgan* [1990b] predictions that pulling forces acting on the sides of the lithosphere induce bending moments that depress the ridge axis and uplift the flanks. Their early 2-D modeling efforts showed that relief of these valleys scales with the maximum stress supported by the lithosphere, which increases with the thickness of the lithosphere beneath the ridge axis. This mechanism is consistent with our model results of increasing in axial valley depth with increasing H_0 at a given value of M (Figure 4.11). However, this mechanism does not explain the increasing axial valley depth with decreasing M because the maximum tensile stress in the lithosphere is limited by the strength of the unfaulted material near the ridge axis and is independent of M [*Buck et al.*, 2005a]. The observed dependence of axial valley depth on M therefore requires an additional mechanism.

This mechanism is revealed upon noticing that for uniform-M models (Figure 4.9), the throw of faults which bound the ridge axis influences the relief seen in the low-pass filtered, long-wavelength topography. This is most clear in the models of M = 0.5 where the long-lived detachment fault contains substantial long-wavelength topography apparent in the low-pass, filtered topography. Furthermore, in cases where M = 0.7 and 0.8, the unfiltered topography shows an axial valley whose edges are delineated by the steep slopes of axis-bounding fault scarps. In these cases, multiple faults accumulate throw on each side of the ridge axis to construct a stair-step pattern rising out of what appears in the long-wavelength topography as the sides of the axial valley. We therefore propose that individual faults uplift the axial flanks and depress the seafloor as they accumulate throw, subsequent faults on the same side of the ridge axis re-enforce the growth of the axial valley relief and extend the relief to wavelengths that are longer than that of individual faults, and that these effects are frozen into the lithosphere over time (Figure 4.14a). It follows that because fault throw is greatest for low values of M, the “long-wavelength” axial valley would be deeper relative to its flanks for decreasing M. Our proposed conceptual model also explains the more extreme values of axial relief for larger throw faults and lower M values at the Chile Ridge [*Howell et al.*, 2016].

A mixture of fault-induced axial relief and along axis coupling can also partially explain the observed deepening of the axial valley at the very southern portions of the ridge segments (i.e., where M is near M_S) in variable injection-rate models compared to the corresponding uniform-M models (Figure 4.11). Without along-axis coupling, large faults in the south would accumulate a great deal of heave, but have a maximum throw that is limited by the elastic properties of the lithosphere. But with along-axis coupling to regions of higher M, the spacing of large southern faults is reduced and more faults form, thus enhancing axial relief over time (Figure 4.14b). This effect, however, does not explain cases where M = 0.5 and H_0 = 4 and 6 km, which exhibit only a single detachment but still deeper axial relief than the corresponding uniform-M models.

4.5.4. Implications for oceanic core complexes

A direct application of our variable magma injection rate models to real-world ridge systems involves the predictions of a one-sided faulting regime (e.g. Figure 4.12, H_0 = 4km, M_N = 0.9 km). Here, a long-lived, detachment fault in the south evolves to have a scarp bottom that bows towards the ridge axis, producing a dome-like structure in the seafloor. These detachments exhibit axis-perpendicular corrugations on the scarp surface (Figure 4.15). This model structure is morphologically similar to portions of slow-spreading Mid-Atlantic Ridge (MAR) segments (e.g. 13 N) where long-lived, detachments display corrugated fault scarps on one side of the ridge axis. On the MAR, these convex corrugated surfaces can extend along axis for up to 10s of km before giving way to smaller fault blocks. Though the full along-axis extent of these detachment faults is uncertain [*Spencer*, 1999; *Smith et al.*, 2006], one leading hypothesis proposes that the detachments persist beyond the associated convex corrugated surface and below the smaller fault blocks. These small blocks are interpreted as pieces of the overriding hanging wall that have broken off of the rest of the hanging wall and are now "riding" in the opposite direction on the foot-wall scarp [*Reston and Ranero*, 2011]. These "rider blocks" explain the fault blocks adjacent to the exposed corrugated surface of the detachment fault.

Whereas this explanation of core complexes adjacent to rider blocks would predict more tectonic strain, and therefore marginally lower values of M where rider blocks form, we offer an explanation that relies on significant along-axis gradients in M. We propose that along-axis variations in magma injection rate can lead to long-lived detachment faults where M is locally near 0.5 and a transition to short-lived, more closely-spaced faults where M is greater than 0.5. One test that could distinguish between these two cases would be to seismically estimate along-axis gradients in crustal thickness, and therefore magma availability.

4.6. Conclusions

In this study, we performed high resolution, 3-D simulations of faulting in MOR lithosphere for ridge segments subjected to along-axis gradients in magma injection rates. We characterized how along-axis variations in M influence along-axis variations in fault characteristics and ridge axis relief, and how these influences change for different lithospheric thicknesses. To aid in this characterization we modified previously published semi-analytical predictions of fault spacing based on simple force-balance arguments to consider the effects of time-dependent fault healing, as well as one- versus two-sided fault behavior.

Our force balance solutions show that the healing-to-weakening length scale ratio, Λ, is an effective scaling because it ensures that faults both strengthen and weaken at approximately the same rate across a wide range of parameters, including magma injection rates, model resolution, fault localization, and spreading rate. Further, the new force balance solutions describe two end-member fault regimes: two-sided faulting exists where successive faults form on opposite sides of the axis, and one-sided faulting exists where faults form on the same side of the axis.

Our 3-D numerical models suggest that thicker axial lithosphere leads to strong across-axis coupling and promotes two-sided faulting, whereas thinner axial lithosphere leads to weak across-axis coupling and promotes one-sided faulting or a transitional faulting regime in which faulting occurs coincidentally on both sides of the ridge axis. In models with variable injection rates imposed along-axis, strong along-axis coupling can destabilize long-lived detachment faults when the lithosphere is thick and lead to smaller spacing along portions of a ridge segment where $M \leq 0.6$.

Additionally, we observe that axial relief increases with lithospheric thickness, as predicted by the 2-D models of *Chen and Morgan* [1990b], but models also predict the axial valley to deepen with decreasing M. We attribute this directly to the increase in fault slip with decreasing M, and faulting that depresses the axial valley and uplifts the flanks proportional to fault throw. We propose that successive faults are frozen into the lithosphere as inactive faults migrate off-axis, providing a tectonic source of long-wavelength axial valley relief.

The models predict long-lived detachment faults with convex, corrugated surfaces along portions of a ridge segment where M close to 0.5, but as M increases along axis away from the detachment fault, the faulting style transitions to multiple smaller faults. We propose that such a variation in M may be responsible for Mid-Atlantic Ridge segments that exhibit oceanic core complexes adjacent to smaller fault blocks. This is distinct from the previously proposed hypothesis that the smaller faults are blocks riding on top of a detachment fault that extends much further along the ridge segment where M is near 0.5 and relatively uniform along axis. Future studies that quantify the along-axis variation in magma budget near oceanic core complexes are needed to distinguish among these hypotheses.

4.7. Tables and figures

Table 4.1. Descriptions, values, and units for model parameters.

Symbol	Description	Value	Units
v_i	Velocity field		mm/yr
x_i	Cartesian position		m
M	Fraction of magmatic extension	0.5 – 1.0	-
$u_{1/2}$	Ridge half-spreading rate	30	mm/yr
w_{MIZ}	Magma injection zone width	312.5	m
$\sigma_{ij}^{'}$	Deviatoric stress		MPa
P	Pressure		MPa
ρ	Density	1,000 – 2,900	kg/m^3
g_i	Gravitational acceleration	9.81	m/s^2
$\dot{\varepsilon}_{ij}$	Strain rate		1/s
η_v	Lithosphere creep viscosity	$1\times10^{18} - 1\times10^{24}$	Pa s
G	Elastic shear modulus	40	GPa
Δt	Computational visco-elastic timestep	< 3.9	kyr
η_{ve}	Visco-elastic viscosity	$< 1\times10^{24}$	Pa s
$\mathbf{Z}$	Visco-elastic ratio		-
σ_Y	Yield stress		GPa
C	Cohesion	0 – 30	MPa
ϕ	Friction angle	30	degrees
ε_{aps}	Accumulated plastic strain		-
$\varepsilon_{crit,1}$	Critical ε_{aps} for onset of cohesion loss	0.02	-
$\varepsilon_{crit,2}$	Critical ε_{aps} for full cohesion loss	0.1	-
τ	Plastic healing timescale	20	kyr
η_{vep}	Full visco-elasto-plastic viscosity	$< 1\times10^{24}$	Pa s
H_0	Axial lithosphere thickness	4, 6, 7	km
H	Lithosphere thickness	4 – 8, 6 – 12, 7 – 14	km
θ	Fault dip	38 – 50	degrees
A	Maximum bending force change	1,200	Pa/M
B	Bending force tuning parameter	50	-
x_{af}	Off-axis fault migration distance		m
h	Fault heave		m
u_{af}	Off-axis fault migration velocity		mm/yr
ΔS	Characteristic fault spacing		m
u_h	Fault slip rate		mm/yr
Λ	Healing-to-weakening length scale ratio	~ 1	-

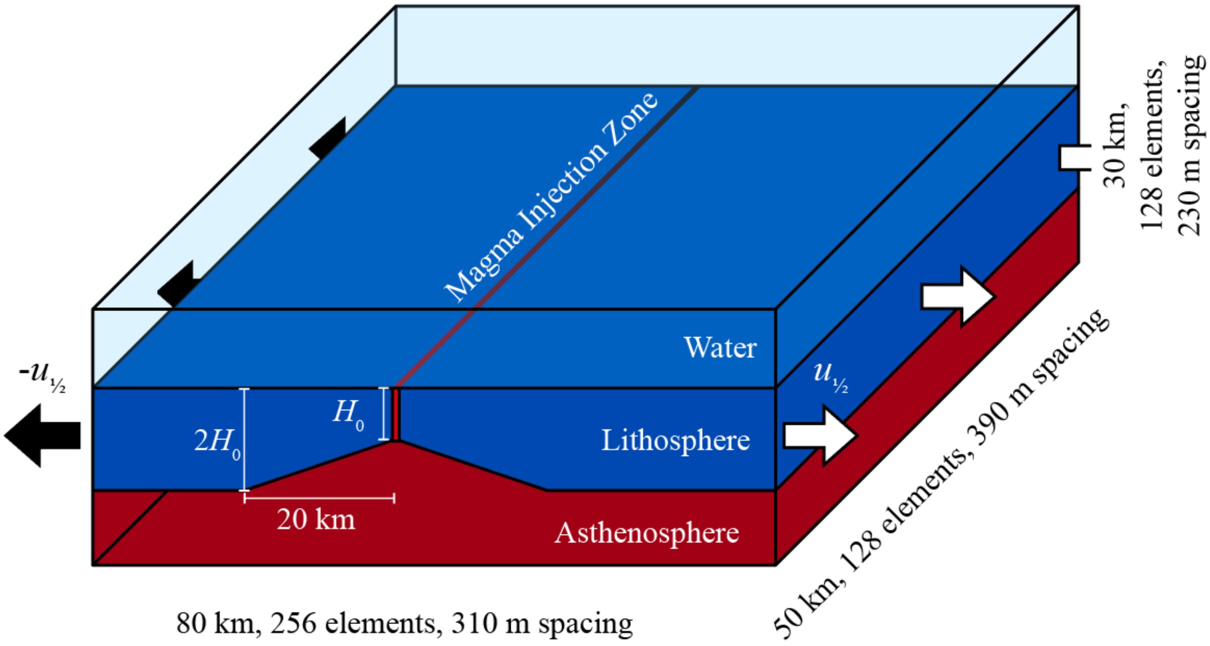

Figure 4.1. Basic model setup: a low-viscosity "ocean" (transparent blue) overlays an elasto-plastic lithosphere (solid blue) defined by temperature that increase from 0° at the surface to 600°C at a depth of ½ *H*. The lithosphere then transitions to a 1,300 °C viscous asthenosphere (red) over an additional depth of 5 *H*. The depth of the 600°C-isosurface doubles from H_0 at the ridge axis to $2H_0$ at a distance 20 km from the axis. Material is injected in a narrow "Magma Injection Zone" (MIZ) that defines the ridge axis (red). The volumetric rate of injection is proportional to the fraction of total extension accommodated magmatically, *M*. The left and right model boundaries impose zero shear traction and have a Dirichlet normal velocity condition equal to half spreading rate, ± $u_{1/2}$. The front and back boundaries have zero normal velocities and zero shear tractions. Material is free to flow into the bottom of the model dynamically, but is set to have an imposed inflow velocity at the top that conserves water volume; both boundaries have zero shear tractions.

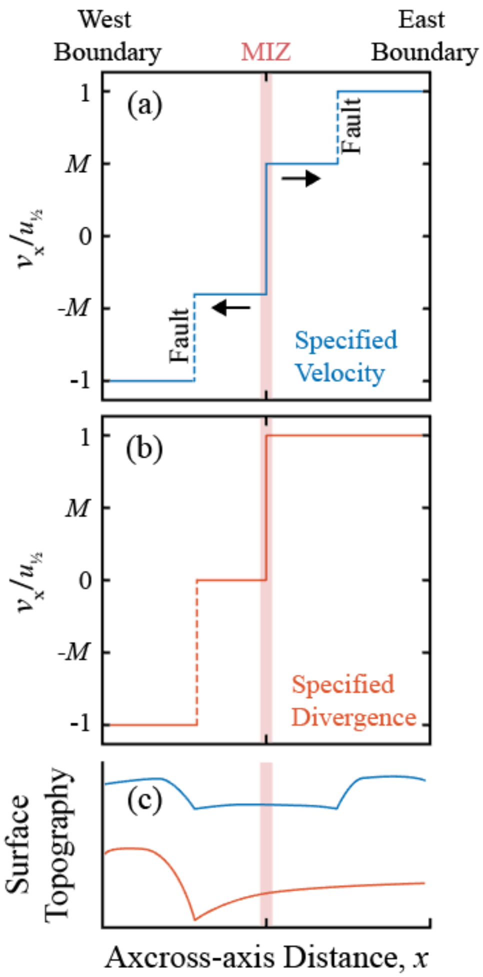

Figure 4.2. Schematic of lithosphere velocities, v_x, for a magma injection zone (MIZ) imposed through (a) specified velocity on either side of the MIZ and (b) specified divergence across the MIZ. (c) Corresponding cartoons of surface topography for velocity (blue) and divergence (orange) specification. Imposing velocities on the sides of the MIZ would force faulting to occur on both sides of the ridge axis, whereas imposing a divergence in the MIZ is allows faulting to respond dynamically, sometimes occurring on one side of the ridge axis and other times occurring on both sides.

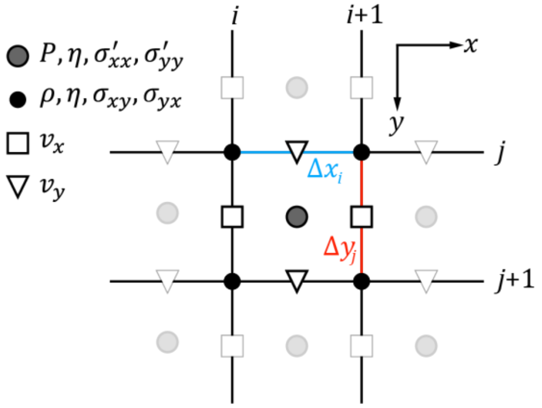

Figure 4.3. Stencil for a fully-staggered grid for a 2-D finite difference model. Four sets of nodes are the evaluation points of pressure, viscosity, and normal stresses (grey circles), density, viscosity, and shear stresses (black circles), and the two velocity components (open shapes).

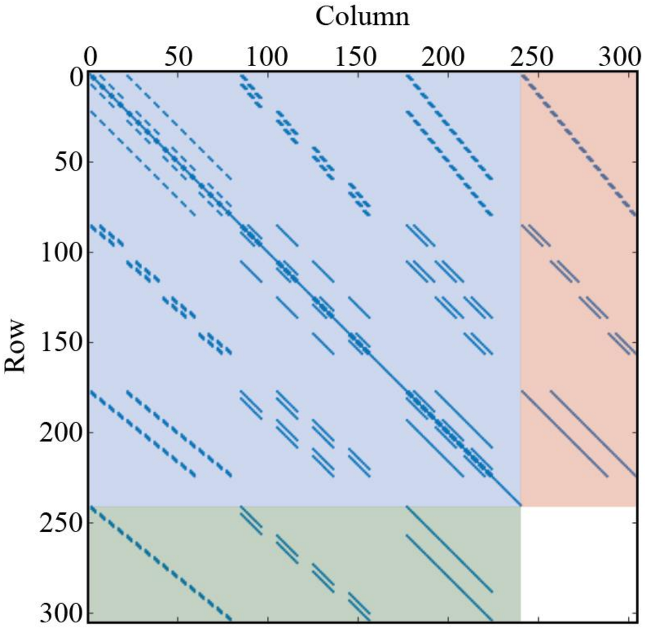

Figure 4.4. Diagram of an example 3-D finite difference *L* matrix for a 4 × 4 × 3 model setup. Lines mark nonzero entries, and colored backgrounds highlight the velocity stiffness submatrix, *K* (blue), the gradient operator matrix, *G* (red), and the divergence operator matrix, G^T (green).

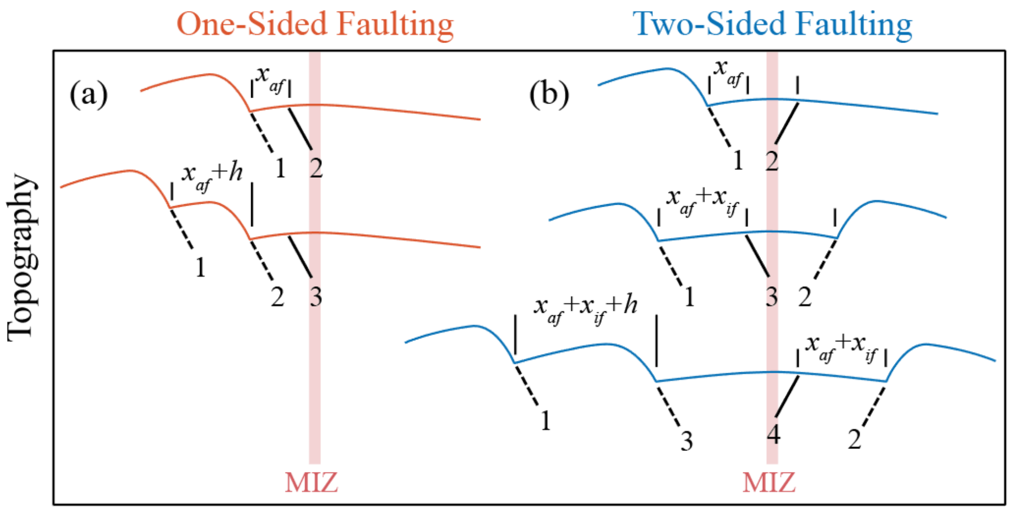

Figure 4.5. Cartoons of seafloor topography for the (a) one-sided (red) and (b) two-sided (blue) faulting regimes. Solid dipping black lines denote active faults, dashed black lines denote inactive faults, and vertical black lines show fault scarp bottoms where the fault scarp intersects the seafloor. (a) In the one-sided faulting regime, Fault 1 initiates at the axis, and then migrates off-axis a distance x_{af} before achieving its total heave. Eventually, Fault 2 initiates on the same side of the MIZ as Fault 1 near the ridge axis. Fault 2 then migrates off-axis and achieves a total heave, h, by the time Fault 3 initiates, resulting in a final spacing between Faults 1 and 2 of $x_{af} + h$. (b) In the two-sided regime, Fault 2 initiates on the opposite side of the axis and the inactive Fault 1 continues to migrate off-axis an additional distance x_{if}. Fault 3 then forms on the same side of the axis as Fault 1 at an initial spacing of $x_{af} + x_{if}$. Following this, Fault 3 migrates off-axis and achieves a total slip h by the time Fault 4 initates, resulting in a final fault spacing of $x_{af} + x_{if} + h$.

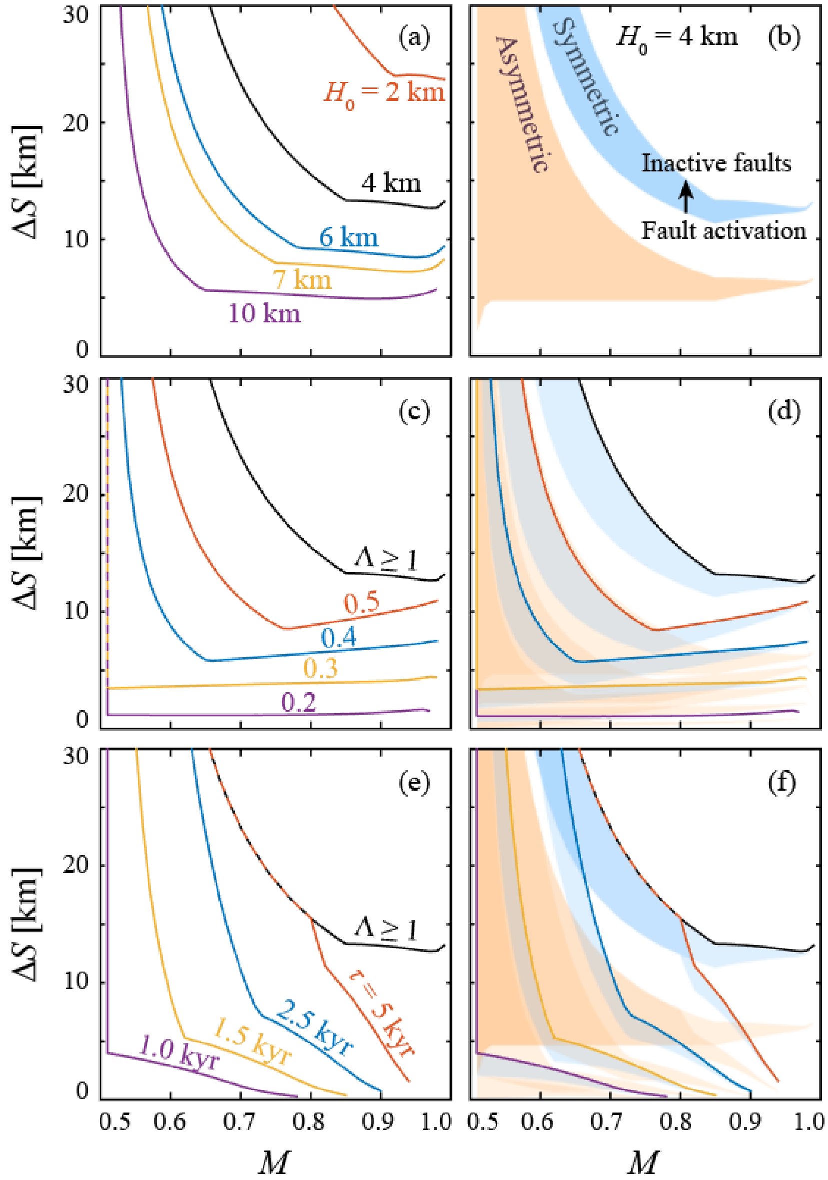

Figure 4.6. (a) Semi-analytical force balance predictions of the maximum characteristic fault spacing for various on-axis lithospheric thicknesses. (b) Colored fields show the predicted fault spacing for two-sided (blue) and one-sided (red) faulting patterns for a thickness of H_0 = 4 km. The bottom of each field denotes the initial spacing when a new fault activates; tops indicate the final spacing after all heave has occurred before the fault deactivates. In (c) and (d) reducing the healing-to-weakening ratio, Λ, causes a reduction in the maximum spacing for a thickness of H_0 = 4 km. In (e) and (f) reducing the healing timescale, τ, for H_0 = 4 km causes a reduction in the maximum predicted spacing starting at increasing values M for greater values of τ (τ = 5 kyr corresponds approximately to $\Lambda = 1$ for $M = 0.7$).

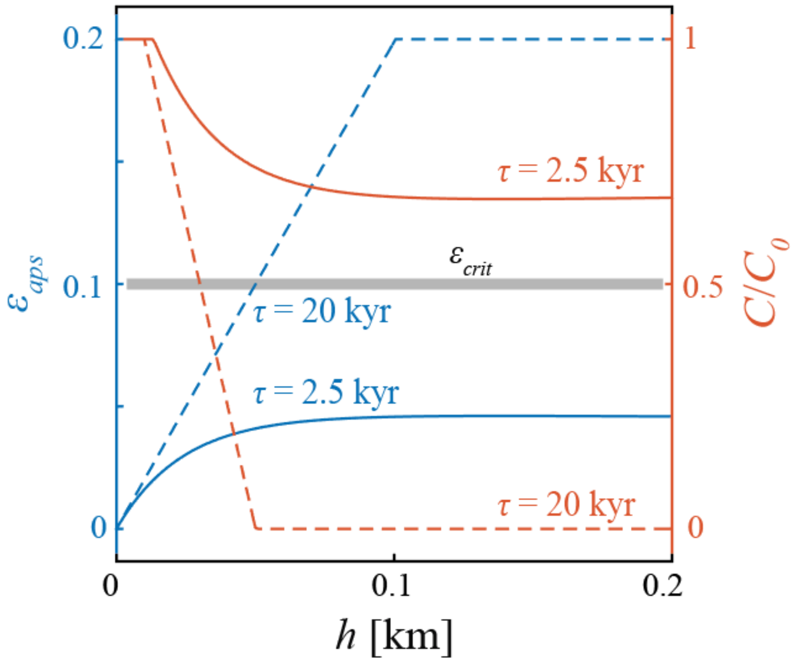

Figure 4.7. Force balance predictions of accumulated plastic strain (blue) and normalized cohesion (orange) for a system with H_0 = 4 km and M = 0.7. Decreasing the healing timescale from τ = 20 kyr (dashed lines) to τ = 2.5 kyr (solid lines) reduces the plastic strain that accumulates and limits cohesion to larger minimum values.

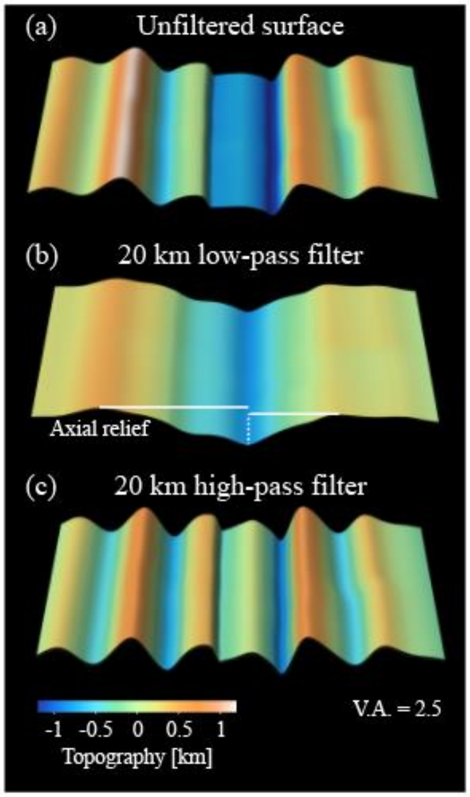

Figure 4.8. Illuminated model seafloor (lithosphere-sticky water boundary) for a model with uniform M along the ridge axis with H_0 = 4 km and M = 0.7. Topography is shown for the (a) output surface, (b) long-wavelength (low-pass filtered) topography after removing wavelengths ≤ 20 km in the spectral domain; white lines showing the estimation of axial relief between the deepest part of the valley and the shallowest part of the valley flanks, and (c) short wavelength (high-pass filtered) topography after removing wavelengths > 20 km.

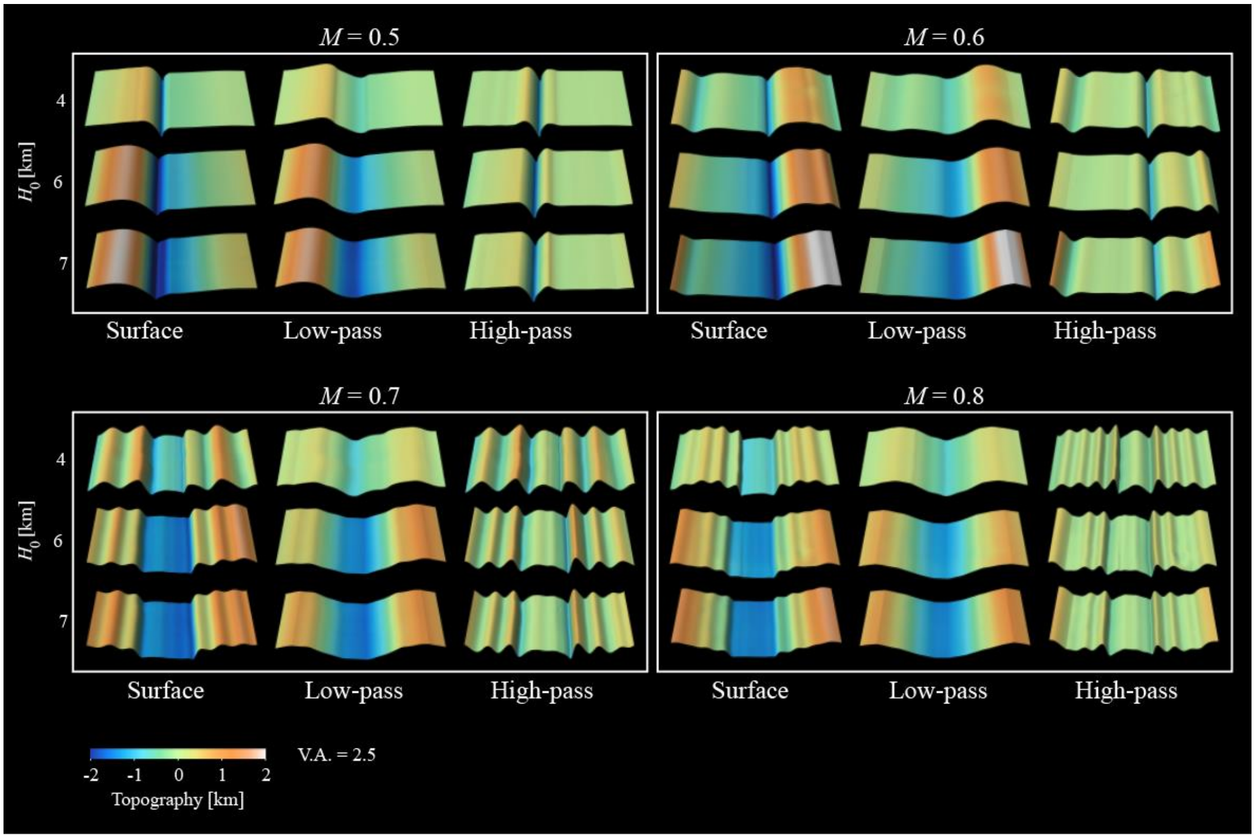

Figure 4.9. Examples of illuminated model seafloor for uniform injection-rate models with the labeled values of *M* and on-axis lithosphere thickness. Each panel shows the output topography, the long-wavelength (low-pass filtered) topography, and the short-wavelength (high-pass filtered) topography.

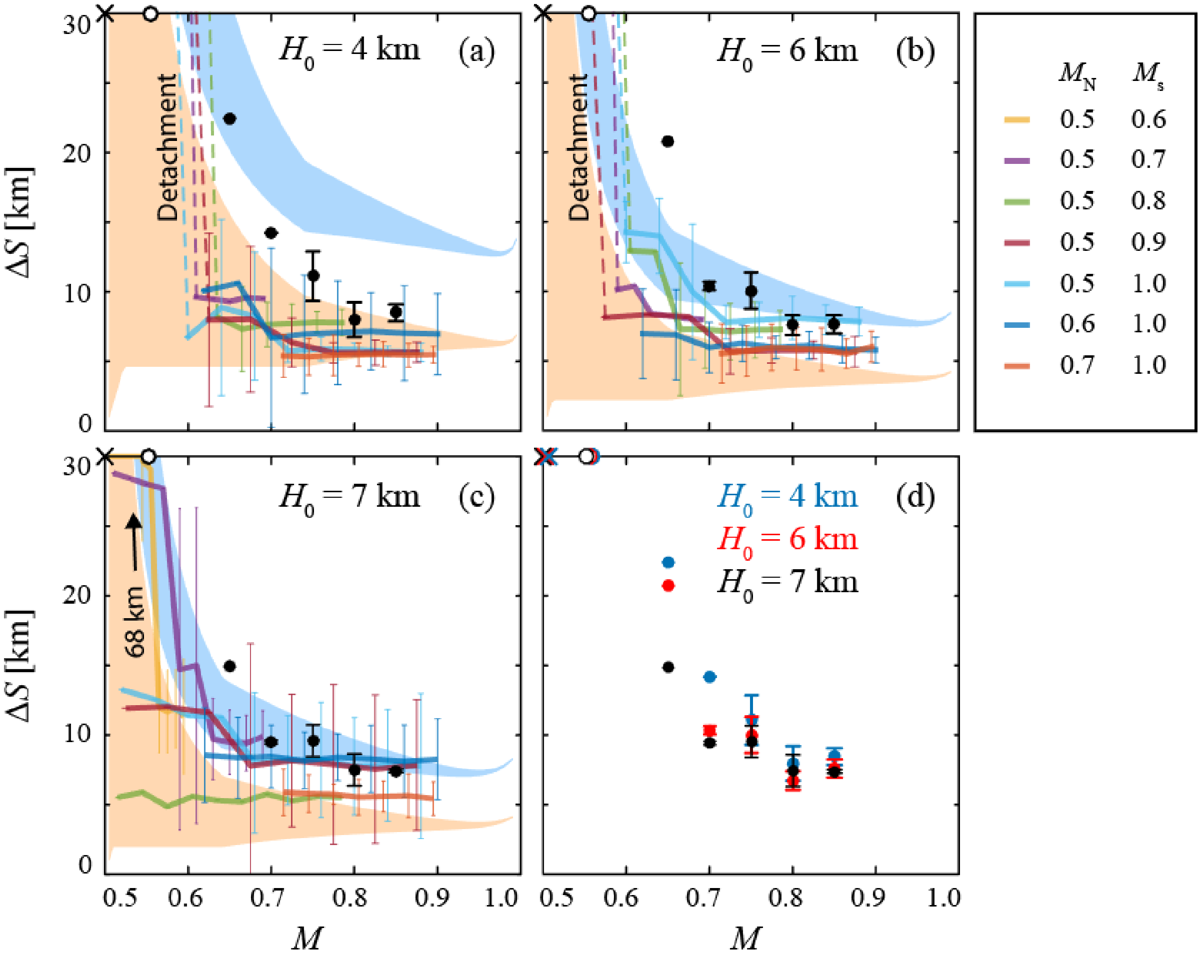

Figure 4.10. Summary of results of fault spacing. In (a-c) colored fields are the same as in Figure 4.4b, but for different on-axis lithospheric thicknesses. (a) $H_0 = 4$ km, (b) 6 km, and (c) 7 km. Solid black circles and error bars correspond to models of uniform *M*, ×s indicate single long-lived faults that persist through the model lifetime, and open circles indicate finite fault spacing > 30 km, though it is difficult to characterize this spacing and distinguish between model results. Colored lines and error bars show results for models with along-axis variations in *M*; lines are dashed when connecting to a long-lived fault (infinite spacing). A comparison of results for the uniform-*M* models across all values of H_0 is shown in (d).

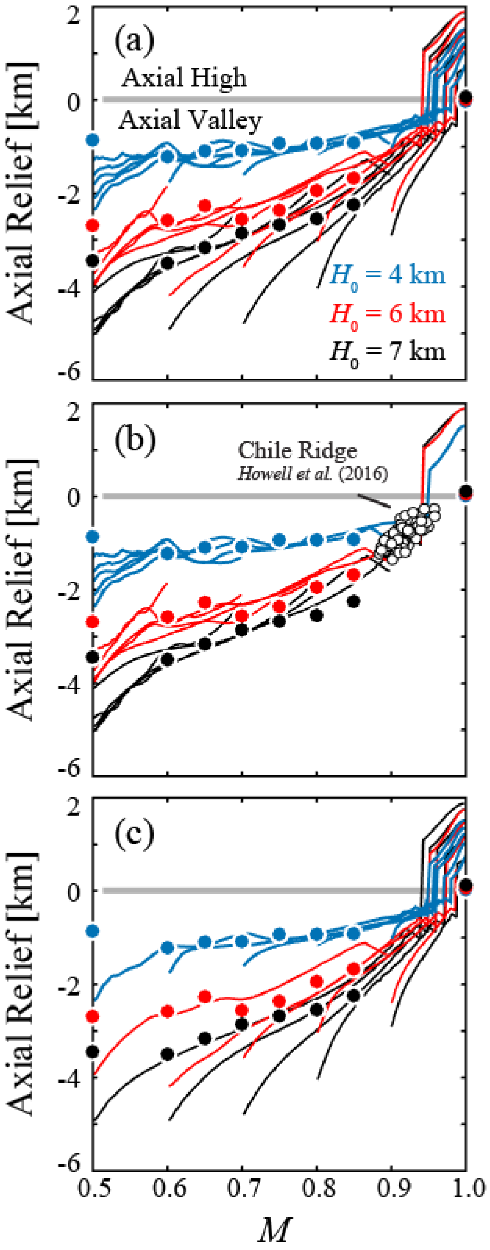

Figure 4.11. Measured long-wavelength axial relief for axial lithospheric thicknesses of H_0 = 4 km (blue), 6 km (red), and 7 km (black). Circles show results for models with uniform values of M; solid lines show relief for variable-M models along the ridge associated with the corresponding values of M . Panels show (a) all models, (b) models where M_S = 0.5, and (c) models where M_N = 1.0. In (b) white circles show measurements of M and axial relief at nine Chile Ridge segments [*Howell et al.*, 2016].

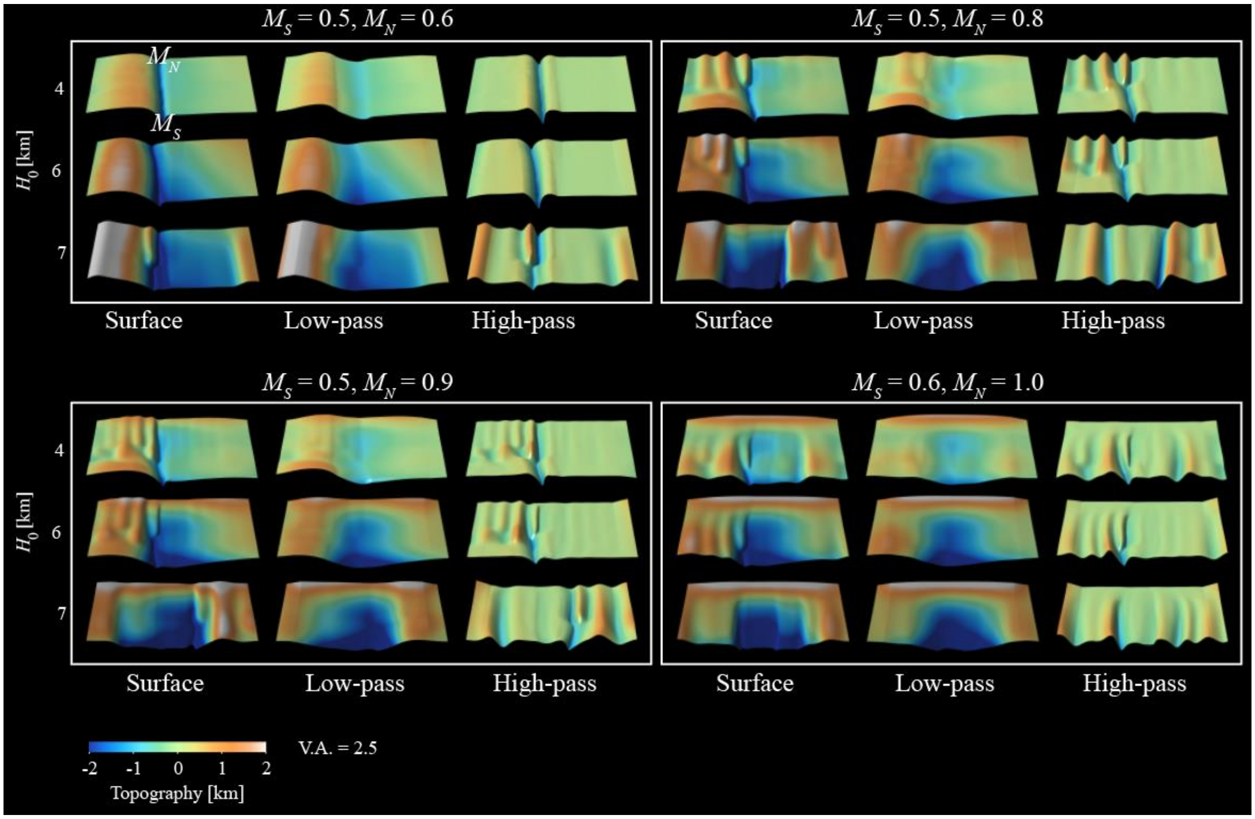

Figure 4.12. Examples of illuminated model seafloor for variable injection-rate models with the labeled values of on-axis lithosphere thickness and M, increasing from M_S in the south ($y = 0$) to M_N in the north ($y = 50$ km). Each panel shows the output topography, the long-wavelength (low-pass filtered) topography, and the short-wavelength (high-pass filtered) topography.

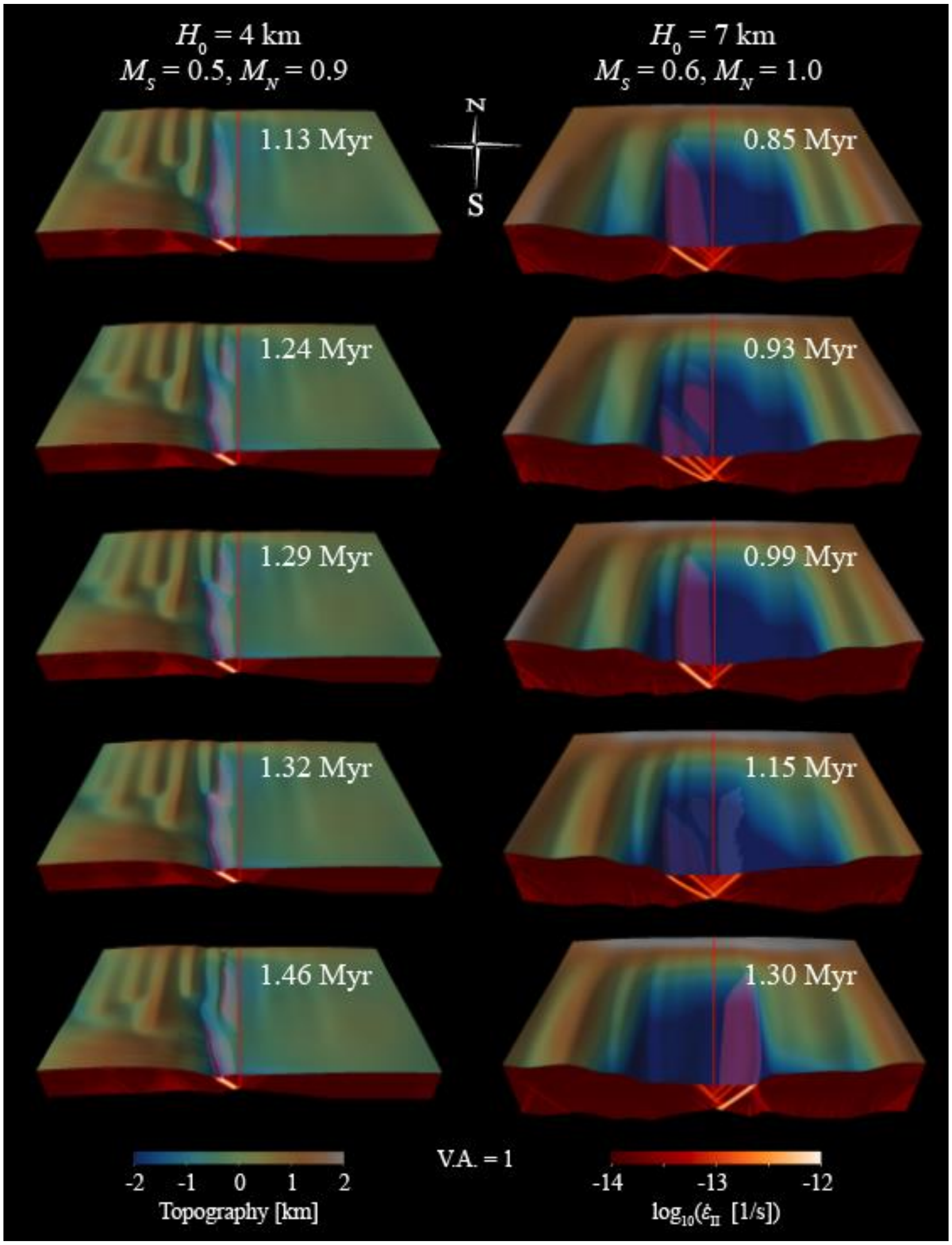

Figure 4.13. Examples of fault evolution for simulations of variable along-axis injection rates with H_0 = 4 and 7 km, and M varying from M_s =0.5 to M_n = 0.9 and M_s = 0.6 to M_n = 1.0, respectively. The asthenosphere is colored per the second invariant of strain rate, $\dot{\varepsilon}_{II}$, and red isosurfaces indicate the active faults. For H_0 = 4 km, faulting initiates in the north, where M is relatively high and migrates southward toward a long-lived fault, eventually linking with the long-lived fault at depth. The result is one-sided faulting with asymmetric magma injection. For H_0 = 7 km, faulting sometimes migrates from north to south and connects to longer-lived faults, but is also observed initiate a new fault along the entire axis simultaneously. The result is mostly two-sided faulting with more symmetric magma injection over time.

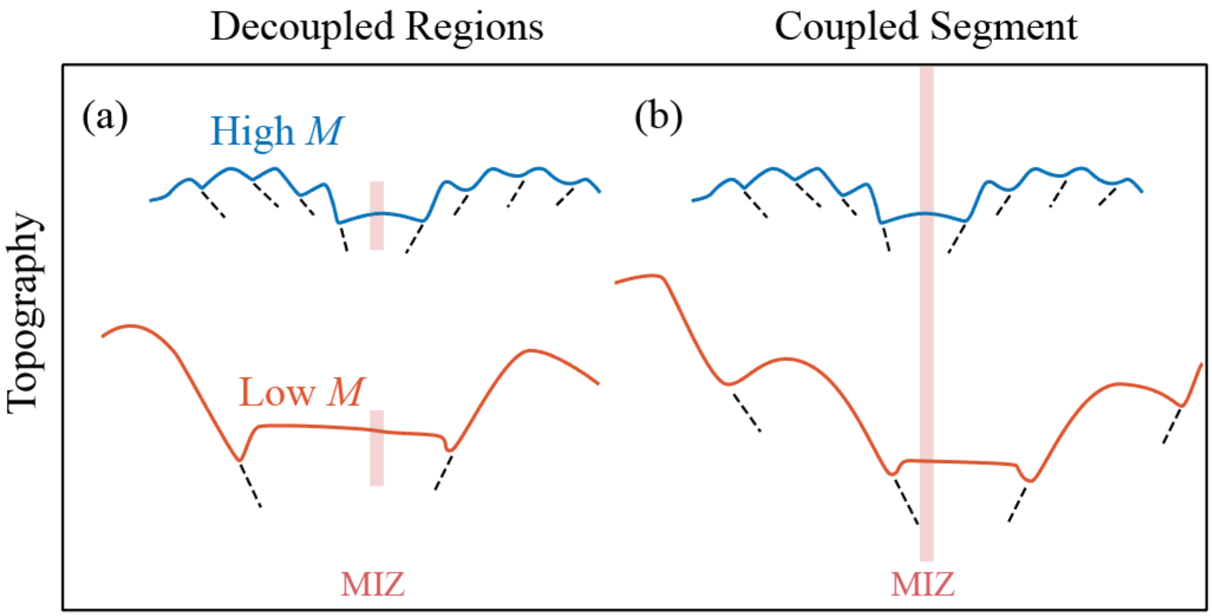

Figure 4.14. Cartoons of seafloor topography showing axial relief for the same high (blue) and low (red) values of *M* in (a) decoupled regions and (b) regions coupled along-axis. Dashed black lines denote faults. In (a), small-offset faults formed at high *M* accumulate little vertical relief in the lithosphere over time, and thus depress the axis and uplift the axis flanks very little. Large offset faults formed at low *M* accumulate a great amount of throw, and deeply depress the axis and uplift the flanks to shallower depths. In (b), the coupling of the low-*M* region to high-*M* regions reduces the spacing of large-throw faults, enhancing axial relief.

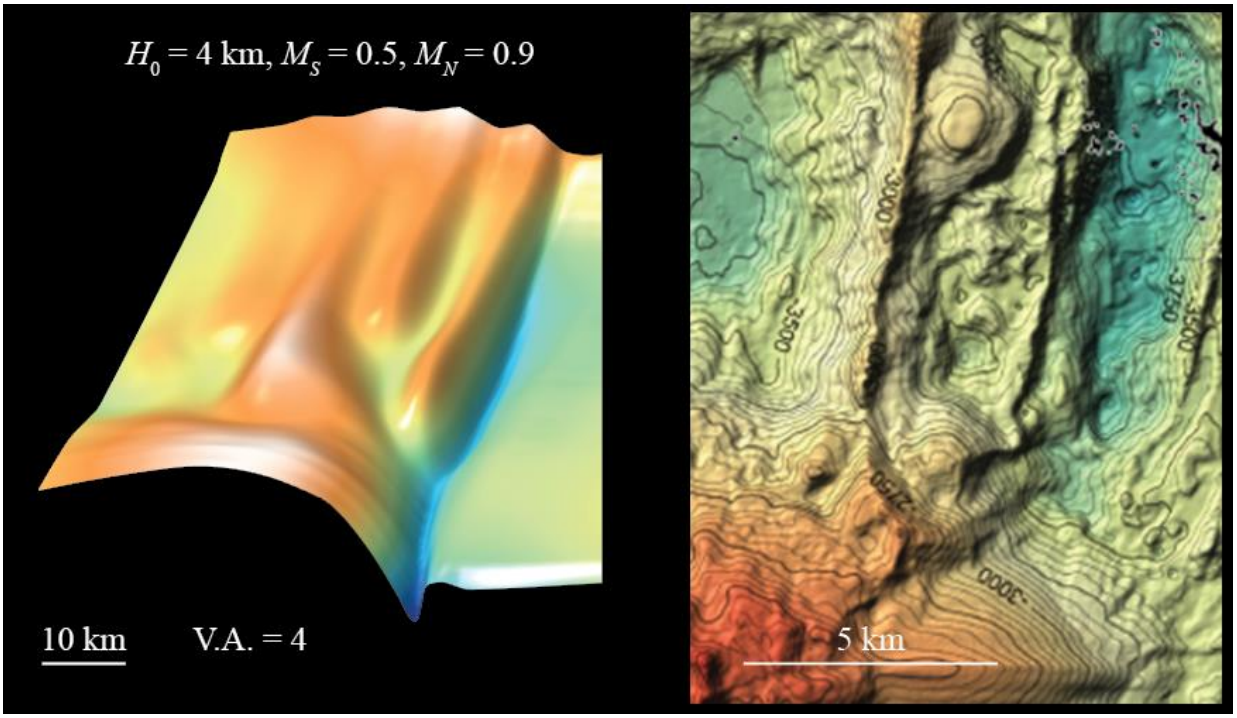

Figure 4.15. Topography for (left) $H_0 = 4$ km variable injection rate model showing long-lived, corrugated fault surface near $M_S = 0.5$ and periodic fault formation in the north and (b) Mid-Atlantic Ridge segment 13 N [*Escartín et al.*, 2016, in prep] showing core complex with corrugated detachment fault surface in the south and smaller periodic faults further north along the axis.

CONCLUSIONS

In our statistical analysis and modeling of vertical GPS motions of the San Andreas fault system (Chapter 2), we exposed the form and magnitude of tectonic uplift in the region. Recent studies of vertical GPS velocities in California have been critical to advancing our understanding of groundwater use and replenishment. These studies largely attribute long-wavelength uplift and subsidence signals to the isostatic response of the crust to changes in the storage and discharge of groundwater. However, the contribution of vertical motions from the historical earthquake cycle demonstrated that the dominant sources of vertical deformation in California are likely a combination of long-wavelength groundwater-induced isostasy and regional earthquake cycle strain. Further, we find that the current GPS array is ideally situated to map the large-scale time-dependent relaxation of the mantle resulting from the next significant rupture of the fault system. These results have implications for seismic moment deficit and seismic hazard mitigation of active faults in southern California.

In our study of Chile Ridge bathymetry (Chapter 3), we characterized relationships between magmatic accretion inferred from tectonic strain, fault characteristics, ridge geometry, and axial morphology. We predict that increases in *M* from segment ends to segment centers result in shorter throw, similarly spaced faults. The finding contrasts with a study of the Mid-Atlantic Ridge that shows a tendency for fault spacing to be widest near segment ends and decreases toward segment centers. Chile Ridge faults show a cyclic pattern of coalescence near the ridge axis and growth into abyssal hills within only a short distance of the center of the median axial valley. Furthermore, rather than responding passively to plate separation, the mantle beneath the Chile Ridge likely exhibits undulations in extension relieved magmatically. These undulations probably indicate deep-sourced variations in melt supply from segmented active mantle upwelling that is partly decoupled from the geometry of the tectonic plate boundary at the surface.

The systematic along-axis variations in strain and axial morphology without corresponding changes in fault spacing demonstrate the inherently 3-D nature of mid-ocean ridge processes, motivating 3-D numerical models of magmatic accretion and faulting. Thus, in our following study (Chapter 4), we performed high resolution, 3-D simulations of faulting for ridge segments subjected to along-axis gradients in magma injection rates and compared the output topography to semi-analytical force balance predictions of fault spacing.

Our force balance solutions predict that the ratio of imposed healing distance to weakening distance can influence the spacing of faults, motivating future studies of the true natural processes that control rock weakening and healing. Further, the new force-balance solutions describe two end-member fault regimes: two-sided faulting exists where successive faults form on opposite sides of the axis, and one-sided faulting exists where faults form on the same side of the axis.

Our 3-D numerical models suggest that thicker axial lithosphere leads to strong across-axis coupling and promotes two-sided faulting, whereas thinner axial lithosphere leads to weak across-axis coupling promotes one-sided faulting. Additionally, we observe that axial relief increases with lithospheric thickness as has been well recognized, but in addition, we find that axial valleys that deepen with increasing decreasing *M*, or the corresponding increasing fraction of tectonic strain. We attribute this directly to the vertical relief of successive faults that are frozen into the lithosphere as inactive faults migrate off-axis, providing a tectonic source of long-wavelength axial valley relief.

Finally, the models predict long-lived detachment faults with convex, corrugated surfaces along portions of a ridge segment where *M* is close to 0.5, but as *M* increases along axis away from the detachment fault, the faulting style transitions to multiple smaller faults. We propose that such a variation in *M* may be responsible for oceanic core complexes adjacent to smaller fault blocks found on the Mid-Atlantic Ridge segments. This explanation is alternative to the hypothesis that the smaller faults are blocks riding on top of a detachment fault that extends much further along the ridge segment, and distinguishing between these competing hypotheses could be done with future studies to seismically estimate the magma budget along-axis in these regions.

REFERENCES

Akaike, H. (1974), A new look at the statistical model identification, *Automatic Control, IEEE Transactions on*, *19*(6), 716-723.

Amos, C. B., P. Audet, W. C. Hammond, R. Burgmann, I. A. Johanson, and G. Blewitt (2014), Uplift and seismicity driven by groundwater depletion in central California, *Nature*(509), 483-486.

Argus, D. F., Y. Fu, and F. W. Landerer (2014), Seasonal variation in total water storage in California inferred from GPS observations of vertical land motion, *Geophys. Res. Lett.*, *41*, 1971–1980.

Balay, S., et al. (2015), PETSc users manual, *Technical Report ANL-95/11–Revision 3.6*, *Argonne National Laboratory*.

Behn, M. D., and G. Ito (2008), Magmatic and tectonic extension at mid-ocean ridges: 1. Controls on fault characteristics, *Geochem. Geophys. Geosys.*, *9*(8), Q08O10, doi:10.1029/2008GC001965.

Behn, M. D., J. Lin, and M. T. Zuber (2002), Evidence for weak oceanic transform faults, *Geophysical Research Letters*, *29*(24), 60-61-60-64.

Blume, F., H. T. Berglund, K. Feaux, S. T. Dittmann, C. P. Walls, K. E. Austin, and G. S. Mattioli (2013), Stability of GNSS Monumentation: Analysis of Co-Located Monuments in the Plate Boundary Observatory, paper presented at American Geophysical Union, Fall Meeting 2013, San Francisco, CA.

Bohnenstiehl, D. R., and M. C. Kleinrock (1999), Faulting and fault scaling on the median valley floor of the trans-Atlantic geotraverse (TAG) segment, ∼26°N on the Mid-Atlantic Ridge, *Journal of Geophysical Research: Solid Earth*, *104*(B12), 29351-29364.

Bohnsenstiehl, D. R., and S. M. Carbotte (2001), Faulting patterns near 19°30'S on the East Pacific Rise: Faults formation and growth at a superfast spreading center, *Geochemistry Geophysics Geosystems*, *2*, 2001GC000156.

Borsa, A. A., D. C. Agnew, and D. R. Cayan (2014), Ongoing drought-induced uplift in the western United States, *Science*, *345*(6304), 1587-1590.

Boussinesq, J. (1885), *Application des potentiels à l'étude de l'équilibre et du mouvement des solides élastiques, principalement au calcul des deformations et des pressions que produisent, dans ces solides, des efforts quelconques exercés sur und petite partie de leur surface ou de leur intérieur;memoire suivi de notes étendues sur divers points de physique mathématique et d'analyse*, Gauthier-Villars, Paris.

Buck, W. R. (1993), Effect of lithospheric thickness on the formation of high- and low-angle normal faults, *Geology*, *21*, 933-936.

Buck, W. R., L. L. Lavier, and A. N. B. Poliakov (2005a), Modes of faulting at mid-ocean ridges, *Nature*, *434*(7034), 719-723.

Buck, W. R., L. L. Lavier, and A. N. B. Poliakov (2005b), Modes of faulting at mid-ocean ridges, *Nature*, *434*, 719-723.

Burmister, D., L. Palmer, E. Barber, and T. Middlebrooks (1944), The theory of stress and displacements in layered systems and applications to the designs of airport runways*Rep.*, Washington D.C.

Burnham, K. P., and D. R. Anderson (2002), *Model Selection and Multimodel Inference: A Practical Information-Theoretic Approach (2nd ed.)*, Springer-Verlag.

Burnham, K. P., and D. R. Anderson (2004), Multimodel inference: understanding AIC and BIC in Model Selection, *Sociol. Method. Res.*, *33*, 261–304.

Carbotte, S. M., and K. C. Macdonald (1994a), Comparison of seafloor tectonic fabric at intermediate, fast, and super fast spreading ridges: Influence of spreading rate, plate motions, and ridge segmentation on fault patterns, *J. Geophys. Res.*, *99*(13), 609-613.

Carbotte, S. M., and K. C. Macdonald (1994b), Comparison of seafloor tectonic fabric at intermediate, fast, and superfast spreading ridges: Influence of spreading rate, plate motions, and ridge segmentation on fault pattern, *Journal of Geophysical Research*, *99*, 13,609-613,631.

Chen, Y. J., and W. J. Morgan (1990a), A nonlinear rheology model for mid-ocean ridge axis topography, *Journal of Geophysical Research*, *95*, 17,583-517,604.

Chen, Y. J., and W. J. Morgan (1990b), Rift valley/no rift valley transition at mid-ocean ridges, *Journal of Geophysical Research*, *95*, 17,571-517,581.

Conrad, C. P. (2013), The solid Earth's influence on sea level, *Geological Society of America Bulletin*, *125*(7-8), 1027-1052.

Cowie, P. A., C. H. Scholz, M. Edwards, and A. Malinverno (1993), Fault strain and seismic coupling on mid-ocean ridges, *J. Geophys. Res.*, *98*(17), 911-917.

Deng, J., M. Gurnis, H. Kanamori, and E. Hauksson (1998), Viscoelastic flow in the lower crust after the 1992 Landers, California, earthquake, *Science*, *282*, 1689–1692.

Dunn, R. A., V. Lekic, D. R. S., and D. R. Toomey (2005), Three-dimensional seismic structure of the Mid-Atlantic Ridge (35°N): Evidence for focused melt supply and lower crustal dike injection, *J. Geophys. Res*, *110*(B09101), doi:10.1029/2004JB003473.

EarthScope-PBO (2015), GPS Network Velocities, edited, UNAVCO, http://pbo.unavco.org/data/gps/.

Edwards, M. H., D. J. Fornari, A. Malinverno, W. B. F. Ryan, and J. Madsen (1991), The regional tectonic fabric of the East Pacific Rise from 12°50′N to 15°10′N, *Journal of Geophysical Research: Solid Earth*, *96*(B5), 7995-8017.

Escartín, J., P. A. Cowie, R. C. Searle, S. Allerton, N. C. Mitchell, C. J. MacLeod, and A. P. Slootweg (1999), Quantifying tectonic strain and magmatic accretion at a slow spreading ridge segment, Mid-Atlantic Ridge, 29°N, *Journal of Geophysical Research: Solid Earth*, *104*(B5), 10421-10437.

Escartín, J., et al. (2016, in prep), Tectonic structure, evolution, and the nature of oceanic core complexes and their detachment fault zones (13°20'N and 13°30'N, Mid Atlantic Ridge), *Geochem. Geophys. Geosys.*

Fay, N. P., and E. D. Humphreys (2005), Fault slip rates, effects of elastic heterogeneity on geodetic data, and the strength of the lower crust in the Salton Trough region, southern California, *J. Geophys. Res.*, *110*.

Fialko, Y., M. Simons, and D. Agnew (2001), The complete (3-D) surface displacement field in the epicentral area of the 1999 MW7.1 Hector Mine Earthquake, California, from space geodetic observations, *Geophys. Res. Lett.*, *28*.

Fornberg, B. (1995), *A Practical Guide to Pseudospectral Methods*, Cambridge University Press, Cambridge.

Forsyth, D. W. (1992), Finite extension and low-angle normal faulting, *Geology*, *20*, 27-30.

Freed, A. M., and R. Burgmann (2004), Evidence of power-law flow in the Mojave desert mantle, *Nature*, *430*(6999), 548-551.

Gelman, A., J. B. Carlin, H. S. Stern, D. B. Dunson, A. Vehtari, and D. B. Rubin (2014), *Bayesian Data Analysis, Third Edition*, Chapman and Hall/CRC Boca Raton, FL.

Gerya, T. (2010a), Dynamical Instability Produces Transform Faults at Mid-Ocean Ridges, *Science*, *329*(5995), 1047-1050.

Gerya, T. (2010b), *Introduction to Numerical Geodynamic Modelling*, Cambridge Univ. Press, Cambridge, U. K.

Gerya, T. (2013a), Initiation of transform faults at rifted continental margins: 3D petrological-thermomechanical modeling and comparison to the Woodlark Basin, *Petrology*, *21*(6), 550-560.

Gerya, T. V. (2013b), Three-dimensional thermomechanical modeling of oceanic spreading initiation and evolution, *Physics of the Earth and Planetary Interiors*, *214,* 35-52.

Goff, J. A., Y. Ma, A. Shah, J. R. Cochran, and J.-C. Sempéré (1997), Stochastic analysis of seafloor morphology on the flank of the Southeast Indian Ridge: The influence of ridge morphology on the formation of abyssal hills, *Journal of Geophysical Research*, *102,* 15,521-515,534, 510.1029/1097JB00781.

Hearn, E. H., S. McClusky, S. Ergintav, and R. E. Reilinger (2009), Izmit earthquake postseismic deformation and dynamics of the North Anatolian Fault Zone, *Journal of Geophysical Research: Solid Earth*, *114*(B8), n/a-n/a.

Hetland, E. A., and B. H. Hager (2005), Postseismic and interseismic displacements near a strike-slip fault: A two-dimensional theory for general linear viscoelastic rheologies, *J. Geophys. Res.-Sol. Ea.*, *110*(B10).

Hirth, G., and D. L. Kohlstaedt (2003), Rheology of the upper mantle and the mantle wedge: A view from the experimentalists, in *Inside the Subduction Factory, Geophys. Monogr. Ser.*, edited by J. Eiler, pp. 83-105, AGU, Washington D.C.

Hooft, E. E. E., R. S. Detrick, D. R. Toomey, J. A. Collins, and J. Lin (2000), Crustal thickness and structure along three contrasting spreading segments of the Mid-Atlantic Ridge, 33.5°–35°N, *Journal of Geophysical Research: Solid Earth*, *105*(B4), 8205-8226.

Howell, S. M., G. Ito, M. D. Behn, F. Martinez, J.-A. Olive, and J. Escartín (2016), Magmatic and tectonic extension at the Chile Ridge: Evidence for mantle controls on ridge segmentation, *Geochemistry, Geophysics, Geosystems*, *17*(6), 2354-2373.

Ito, G., and M. D. Behn (2008), Magmatic and tectonic extension at mid-ocean ridges: 2. Origin of axial morphology, *Geochem. Geophys. Geosys.*, *9*(9), Q09O12, doi:10.1029/2008GC001970.

Johnson, K. M., and P. Segall (2004), Viscoelastic earthquake cycle models with deep stress-driven creep along the San Andreas fault system, *J. Geophys. Res.*, *109*.

Karsten, J., et al. (1999), The northern Chile Ridge revealed: Preliminary cruise report of PANORAMA Expedition Leg 04, in *InterRidge News*, edited, pp. 15-21.

Kaus, B. J. P., A. A. Popov, T. S. Baumann, A. E. Pusok, A. Bauville, N. Fernandez, and M. Collignon (2016), Forward and Inverse Modelling of Lithospheric Deformation on Geological Timescales, paper presented at NIC Symposium 2016 - Proceedings, NIC Series, Jülich, DE, Feb. 11-12, 2016.

Knoll, D. A., and D. E. Keyes (2004), Jacobian-free Newton–Krylov methods: a survey of approaches and applications, *Journal of Computational Physics*, *193*(2), 357-397.

Koptev, A., E. Calais, E. Burov, S. Leroy, and T. Gerya (2015), Dual continental rift systems generated by plume-lithosphere interaction, *Nature Geosci*, *8*(5), 388-392.

Kuo, B.-Y., and D. W. Forsyth (1988), Gravity anomalies of the ridge-transform system in the South Atlantic between 31° and 34.5°S: Upwelling centers and variations in crustal thickness, *Marine Geophysical Researches*, *10*, 205-232.

Lavier, L. L., W. R. Buck, and A. N. B. Poliakov (2000), Factors controlling normal fault offset an ideal brittle layer, *J. Geophys. Res.*, *105*(B10), 23431-23442.

Lin, J., and E. M. Parmentier (1989), Mechanisms of lithospheric extension at mid-ocean ridges, *Geophysical Journal*, *96*, 1-22.

Lin, J., and J. Phipps Morgan (1992), The spreading rate dependence of three-dimensional mid-ocean ridge gravity structure, *Geophysical Research Letters*, *19*, 13-16.

Lin, J., G. M. Purdy, H. Schouten, J.-C. Sempéré, and C. Zervas (1990), Evidence from gravity data for focused magmatic accretion along the Mid-Atlantic Ridge, *Nature*, *344*, 627-632.

Lyons, S. N., Y. Bock, and D. T. Sandwell (2002), Creep along the Imperial Fault, southern California, from GPS measurements, *Journal of Geophysical Research: Solid Earth*, *107*(B10), 2249.

Macdonald, K. C. (1982), Mid-ocean ridges: fine scale tectonic volcanic and hydrothermal processes within the plate boundary zone, *Annu. Rev. Earth Planet. Sci.*, *10*, 155-190.

Macdonald, K. C. (1986), The crest of the Mid-Atlantic Ridge: models for crustal generation processes and tectonics, in *The Geology of North America*, edited by P. R. Vogt and B. E. Tucholke, pp. 51-68, Geological Society of America.

Macdonald, K. C., D. S. Scheirer, and S. M. Carbotte (1991a), Mid-Ocean ridges: Discontinuities, segments and giant cracks, *Science*, *253*, 986-994.

Massonnet, D., M. Rossi, C. Carmona, F. Adragna, G. Peltzer, K. Feigl, and T. Rabaute (1993), The displacement field of the Landers earthquake mapped by radar interferometry, *Nature*, *364*(6433), 138-142.

MATLAB (2014), Statistics Toolbox Release 2014b, *The MathWorks, Inc., Natick, Massachusetts, United States*.

Meade, B. J., and B. H. Hager (2004), Viscoelastic deformation for a clustered earthquake cycle, *Geophysical Research Letters*, *31*(10), L10610.

Melini, D., A. Piersanti, G. Spada, G. Soldati, E. Casarotti, and E. Boschi (2004), Earthquakes and relative sea level changes, *Geophys. Res. Lett.*, *31*, L09601.

Milman, M. S. (2002), Petrogenesis of lavas from the axis of the northern Chile Ridge, 143 pp, University of Hawaii at Manoa, Honolulu, HI.

Moore, D. E., and M. J. Rymer (2007), Talc-bearing serpentinite and the creeping section of the San Andreas fault, *Nature*, *448*(7155), 795-797.

Moresi, L., F. Dufour, and H. B. Mühlhaus (2003), A Lagrangian integration point finite element method for large deformation modeling of viscoelastic geomaterials, *Journal of Computational Physics*, *184*(2), 476-497.

Olive, J.-A., and M. D. Behn (2014), Rapid rotation of normal faults due to flexural stresses: An explanation for the global distribution of normal fault dips, *J. Geophys. Res.*, *119*(4), 3722-3739.

Olive, J.-A., M. D. Behn, and L. C. Malatesta (2014), Modes of extensional faulting controlled by surface processes, *Geophysical Research Letters*, *41*(19), 2014GL061507.

Olive, J.-A., J. Escartin, M. Behn, W. R. Buck, G. Ito, and S. M. Howell (2015), Sensitivity of seafloor bathymetry to climate-driven fluctuations in mid-ocean ridge magma supply *Science*, *350*(6258), 310-313.

Patterson, M. S., and T.-F. Wong (2005), Brittle-Ductile Transition, in *Experimental Rock Deformation — The Brittle Field*, edited, pp. 211-237, Springer Berlin Heidelberg, Berlin, Heidelberg.

Paulatto, M., J. P. Canales, R. A. Dunn, and R. A. Sohn (2015), Heterogeneous and asymmetric crustal accretion: New constraints from multibeam bathymetry and potential field data from the Rainbow area of the Mid-Atlantic Ridge (36°15'N), *Geochemistry, Geophysics, Geosystems*, *16*(9), 2994-3014.

Peltier, W. R. (1998), Postglacial variations in the level of the sea: Implications for climate dynamics and solid-Earth geophysics, *Reviews of Geophysics*, *36*(4), 603-689.

Phipps Morgan, J., and Y. J. Chen (1993a), Dependence of ridge-axis morphology on magma supply and spreading rate, *Nature*, *364*, 706-708.

Phipps Morgan, J., and Y. J. Chen (1993b), The genesis of oceanic crust: magma injection, hydrothermal circulation, and crustal flow, *Journal of Geophysical Research*, *98*, 6283-6297.

Poliakov, A. N. B., and W. R. Buck (1998), Mechanics of stretching elastic-plastic-viscous layers: Applications to slow-spreading mid-ocean ridges, in *Faulting and Magmatism at Mid-Ocean Ridges*, edited by W. R. Buck, P. T. Delaney, J. A. Karson and Y. Lagabrielle, pp. 305-323, AGU, Washington D. C.

Pollitz, F. F. (2003), Transient rheology of the uppermost mantle beneath the Mojave Desert, California, *Earth and Planetary Science Letters*, *215*(1–2), 89-104.

Pollitz, F. F. (2005), Transient rheology of the upper mantle beneath central Alaska inferred from the crustal velocity field following the 2002 Denali earthquake, *Journal of Geophysical Research: Solid Earth*, *110*(B8), n/a-n/a.

Pollitz, F. F., C. Wicks, and W. Thatcher (2001), Mantle Flow Beneath a Continental Strike-Slip Fault: Postseismic Deformation After the 1999 Hector Mine Earthquake, *Science*, *293*.

Probabilities, W. G. o. C. E. (2008), The Uniform California Earthquake Rupture Forecast*Rep.*, United States Geological Survey.

Püthe, C., and T. Gerya (2014), Dependence of mid-ocean ridge morphology on spreading rate in numerical 3-D models, *Gondwana Research*, *25*(1), 270-283.

Reston, T. J., and C. R. Ranero (2011), The 3-D geometry of detachment faulting at mid-ocean ridges, *Geochemistry, Geophysics, Geosystems*, *12*(7).

Richards-Dinger, K. B., and P. M. Shearer (2000), Earthquake locations in southern California obtained using source-specific station terms, *Journal of Geophysical Research: Solid Earth*, *105*(B5), 10939-10960.

Rundle, J. B., and D. D. Jackson (1977), A three-dimensional viscoelastic model of a strike slip fault, *Geophysical Journal International*, *49*(3), 575-591.

Sandwell, D. T., S. D. Barbot, C. A. Williams, A. Freed, S. Ellis, M. Huang, and B. Smith-Konter (2012), Investigations into effects of different modeling codes and rheology on predicted coseismic and postseismic surface deformation, paper presented at SCEC Annual Meeting, Palm Springs, CA.

Savage, J. C. (1990), Equivalent strike-slip earthquake cycles in half-space and lithosphere-asthenosphere earth models, *Journal of Geophysical Research: Solid Earth*, *95*(B4), 4873-4879.

Savage, J. C. (2006), Dislocation pileup as a representation of strain accumulation on a strike-slip fault, *Journal of Geophysical Research*, *111*(B4).

Schouten, H., D. K. Smith, J. R. Cann, and J. Escartín (2010), Tectonic versus magmatic extension in the presence of core complexes at slow-spreading ridges from a visualization of faulted seafloor topography, *Geology*, *38*(7), 615-618.

Searle, R. C., and A. S. Laughton (1981), Fine-scale study of tectonics and volcanism on the Reykjanes Ridge, *Oceanol. Acta.*, *4*, 5-18.

Shaw, P. R. (1992), Ridge segmentation, faulting and crustal thickness in the Atlantic Ocean, *Nature*, *358*, 491-493.

Shaw, P. R., and J. Lin (1993), Causes and consequences of variations in faulting style at the Mid-Atlantic Ridge, *Journal of Geophysical Research*, *98*, 21,839-821,851.

Shaw, W. T., and J. Lin (1996), Models of oceanic ridge lithospheric deformation: Dependence on crustal thickness, spreading rate, and segmentation, *Journal of Geophysical Research*, *101*, 17,977-917,993.

Sieh, K., D. H. Natawidjaja, A. J. Meltzner, C.-C. Shen, H. Cheng, K.-S. Li, B. W. Suwargadi, J. Galetzka, B. Philibosian, and R. L. Edwards (2008), Earthquake Supercycles Inferred from Sea-Level Changes Recorded in the Corals of West Sumatra, *Science*, *322*(5908), 1674-1678.

Small, C. (1998), Global systamatics of mid-ocean ridge morphology, in *Faulting and Magmatism at Mid-Ocean Ridges*, edited by R. W. Buck, P. T. Delaney, J. A. Karson and Y. Lagabrielle, pp. 1-25, AGU, Washington D. C.

Smith-Konter, B., and D. T. Sandwell (2006), A model of the earthquake cycle along the San Andreas Fault System for the past 1000 years, *J. Geophys. Res.*, *111*, B01405.

Smith-Konter, B., D. T. Sandwell, and P. Shearer (2011), Locking depths estimated from geodesy and seismology along the San Andreas Fault System: Implications for seismic moment release, *J. Geophys. Res.*, *116*(B06401).

Smith-Konter, B. R., G. M. Thornton, and D. T. Sandwell (2014), Vertical crustal displacement due to interseismic deformation along the San Andreas fault: Constraints from tide gauges, *Geophys. Res. Lett.*, *41*, 3793–3801.

Smith, B., and D. T. Sandwell (2003), Accuracy and resolution of shuttle radar topography mission data, *Geophys. Res. Lett.*, *30*(9).

Smith, B., and D. T. Sandwell (2004), A 3-D semi-analytic viscoelastic model for time-dependent analyses of the earthquake cycle, *J. Geophys. Res.*, *109*.

Smith, D. K., J. R. Cann, and J. Escartin (2006), Widespread active detachment faulting and core complex formation near 13° N on the Mid-Atlantic Ridge, *Nature*, *442*(7101), 440-443.

Spencer, J. E. (1999), Geologic continuous casting below continental and deep-sea detachment faults and at the striated extrusion of Sacsayhuamán, Peru, *Geology*, *27*(4), 327-330.

Steketee, J. A. (1958), On Volterra's dislocations in a semi-infinite elastic medium, *Canadian Journal of Physics*, *36*(2), 192-205.

Tapponnier, P., and J. Francheteau (1978), Necking of the lithosphere and the mechanics of slowly accreting plate boundaries, *Journal of Geophysical Research*, *83*, 3955-3970.

Tebbens, S. F., S. C. Cande, L. Kovaks, J. C. Parra, J. L. LaBrecque, and H. Vergara (1997), The Chile ridge: A tectonic framework, *J. Geophys. Res.*, *102*(B6), 12,035-012,059.

Tian, X., and E.-s. Choi (2016), Effects of axially variable diking rates on faulting at slow spreading mid-ocean ridges, *Earth and Planetary Science Letters, doi:10.1016/j.epsl.2016.10.033*.

Tolstoy, M., A. J. Harding, and J. A. Orcutt (1993), Crustal thickness on the Mid-Atlantic ridge: bull's eye gravity anomalies and focused accretion, *Science*, *262*, 726-729.

Tong, X., D. Sandwell, and B. Smith-Konter (2015), An integral method to estimating the moment accumulation rate on the Creeping Section of the San Andreas fault, in revision, *Geophys. J. Int., GJI-S-14-0783*.

Tong, X., D. T. Sandwell, and B. Konter-Smith (2013), High-resolution interseismic velocity data along the San Andreas Fault from GPS and InSAR, *118*, 1–21.

Tong, X., B. Smith-Konter, and D. T. Sandwell (2014), Is there a discrepancy between geological and geodetic slip rates along the San Andreas Fault System?, *J. Geophys. Res. Solid Earth*, *119*.

Tucholke, B. E., M. D. Behn, W. R. Buck, and J. Lin (2008), Role of melt supply in oceanic detachment faulting and formation of megamullions, *Geology*, *36*(6), 455-458.

Wdowinski, S., B. Smith-Konter, Y. Bock, and D. T. Sandwell (2007), Spatial characterization of the interseismic velocity field in southern California, *Geology*.

Weertman, J. (1964), Continuum distribution of dislocations on faults with finite friction, *Bulletin of the Seismological Society of America*, *54*(4), 1035-1058.

Wessel, P. (2009), A general-purpose Green's function-based interpolator, *Computers & Geosciences*, *35*(6), 1247-1254.

Williams, C. A., and R. M. Richardson (1991), A rheologically layered three-dimensional model of the San Andreas Fault in central and southern California, *Journal of Geophysical Research: Solid Earth*, *96*(B10), 16597-16623.